Study of Low Energy Electron-Impact Induced Ionization and Fragmentation of Uracil

Steven Diskin

A thesis submitted for the degree of Masters of Science

Department of Experimental Physics
National University of Ireland Maynooth
Maynooth
Co. Kildare

February 2016

Head of Department

Professor J. Anthony Murphy

Research Supervisor

Dr. Peter J. M van der Burgt

Contents

Abstract

The aim of this experiment is to study low energy electron impact induced ionization and fragmentation of uracil. The apparatus consists of a pumped vacuum system with an expansion chamber, a collision chamber and a flight tube. A beam of uracil is generated in the expansion chamber, passes through a skimmer and crossed with a pulsed beam of low energy electrons in the collision chamber. The electron gun has a pulse width of 1 μs providing the necessary time of flight resolution and incorporates a deflection system for the steering of the beam. Positive ion fragments are mass resolved and detected using a reflectron time of flight mass spectrometer with a microchannel plate detecter. A multichannel scaler card is used for data acquisition. Code written in LabVIEW is used to control the electron impact energy and the acquisition of mass spectra as a function of electron impact energy. Ion yield curves for positive fragments are obtained from the mass spectra.

Ion yield curves and appearance energies have been obtained from our data set and are in good agreement with results from previous research and other research groups. Partial ionization cross sections have been obtained by normalization of the sum of the ion yield curves to the average of calculated total ionization cross sections at 70 eV. These results provide new information about the fragmentation pathways initiated by electron impact and the cross sections for production of these ions. This research is relevant in the study of low energy secondary electron interactions within biological organisms. The aim of this research is to better understand the fundamental reaction mechanisms leading to DNA strand breaks. The experiment also includes the development and testing of a supersonic source using a 50 micron straight nozzle with argon gas acting as the buffer gas. The supersonic source will improve beam collimation and will enable formation of small nucleobase-water clusters when water vapour is introduced into the source.

Chapter 1: Introduction

1.1 Radiation damage to DNA

The primary energy deposits of radiation are now well understood and the data needed to calculate energy absorption in biological tissue from different types of ionizing radiation is also available [1]. Such data are of importance in calculating doses received by patients during radiotherapy procedures. However there is no precise understanding of the subsequent sequence of events that occur on a femto second time scale after the the primary energy deposits. The absorption of the primary energy deposits can produce a range of chemical and structural modifications in biological tissue. These modifications can occur because of the production of intermediate species such as excited atoms and molecules, radicals, ions, and secondary electrons. These slower chemical events responsible for the products of ionizing radiation are not as well understood [2]. As a consequence, there is no well defined relationship between adsorbed dose and the induced biological effects. It is important to understand and determine the yields of processes induced by secondary species to get a better understanding of the slower chemical events. Of the secondary species generated when high-energy ionizing radiation interacts with human tissue, low energy secondary electrons (with energies less than 20 eV) are the most abundant [3].

In 2000 Sanche et al [4] showed that low energy electrons are very effective in causing DNA strand breaks through electron attachment to the nucleobases. This has led to a new field of experimental and theoretical studies of the processes of inelastic interactions between biomolecules and low energy electrons. Experimental techniques such as mass spectrometry are being used in many laboratories to study the building blocks of biomolecules in the gas phase [5]. Data on processes induced

in the condensed phase by low energy electron impact have been generated since the eighties [6].

In this chapter I will provide a brief introduction into the structure of DNA, RNA and uracil and proceed by describing the sources for its damage and their effects. I will then provide a brief introduction into direct and indirect radiation damage with tissue and a summary on some significant findings to date on electron and photon impact studies on uracil.

1.2 DNA structure and Nucleic acids

It was confirmed in the first half of the 20th century that deoxyribonucleic acid (DNA) was the genetic material in cells. All multicellular organisms are formed by eukaryotic cells [7] and are characterized by their nucleus containing the cellular deoxyribonucleic acid (DNA) within a permeable nuclear envelope. (See figure 1.1)
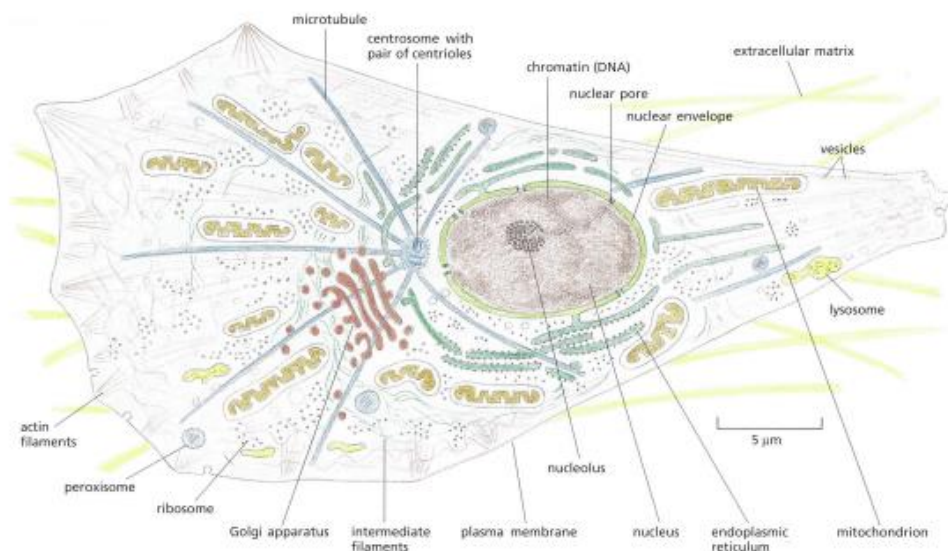
Figure 1.1. Schematic of eukaryotic cell architecture [7].

In eukaryotic cells the DNA is compacted into 23 pairs of chromosomes. This mechanism is thought to provide it with a high degree of stability capable of protecting it from radiation damage. The presence of two copies of each chromosome allows replication to continue in the event that one of the chromosomes suffers irreparable damage. The DNA is the part of the cell nuclei where genetic information is stored.
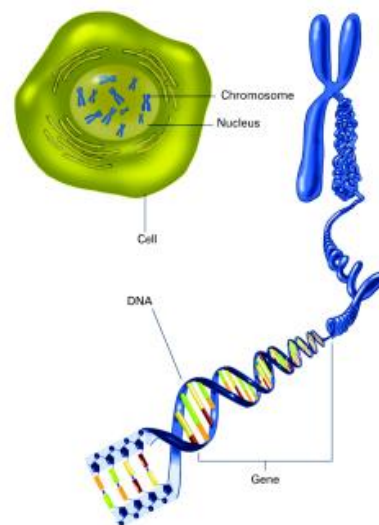
Figure 1.2. Structure and nuclear location of eukaryotic chromosomal DNA and chromosomes [7].

DNA is a biopolymer that consists of a backbone of which each section contains a sugar with five carbon atoms that are connected to a phosphate group [8]. Attached to the sugar is an aromatic nitrogen containing base. There are four bases in DNA: adenine, cytosine, guanine and thymine, see figure 1.3. Each DNA molecule consists of two twisted strands that make up a double helix structure. The two strands are held together by hydrogen bonds between pairs of bases. Adenine forms two hydrogen bonds with thymine and cytosine forms three hydrogen bonds with guanine. The spacing only fits those two combinations. If the identity of one nucleobase is known the other nucleobase can be known. These are referred as complementary strands.
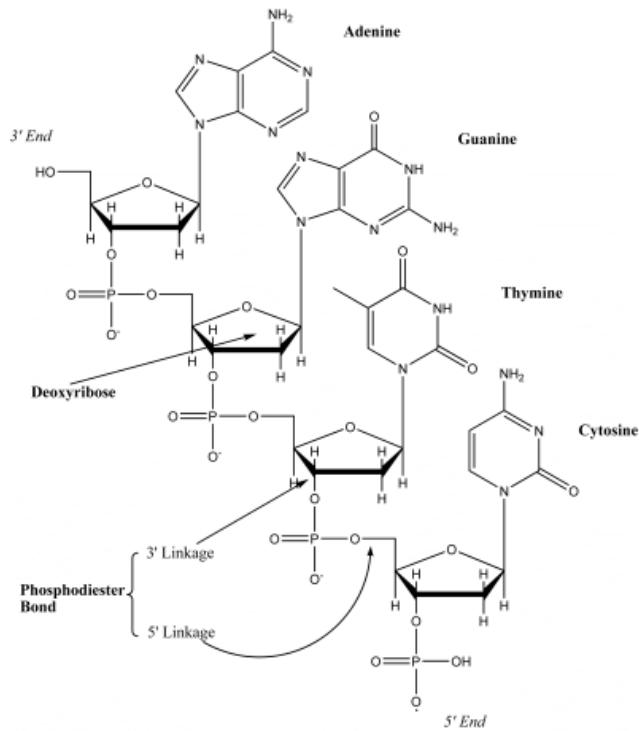
Figure 1.3. Schematic of the structure of DNA showing the four bases (A, Adenine; G, Guanine; T, Thymine; C, Cytosine) bonded to their sugar backbone [7].

For protein synthesis to take place the cell must make a complimentary copy of the required portion of the DNA using Ribonucleic Acid (RNA), a process is known as transcription [8]. In RNA uracil replaces thymine. Uracil is a natural pyrimidine derivative. It is an aromatic heterocyclic organic compound. Ribose in RNA has a hydroxyl group (-OH) where deoxyribose in DNA only has a hydrogen atom at the same position. A chain of RNA can be cleaved many times faster than a chain of DNA under the same conditions due to the presence of the hydroxyl group. The greater stability of DNA contributes to it being a better repository for genetic information.
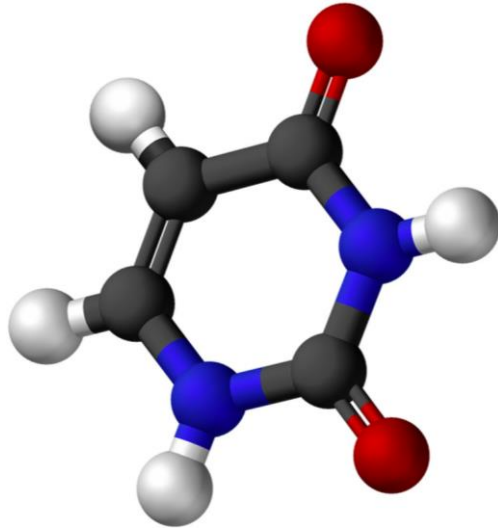
Figure 1.4. Uracil Molecule ($C_4H_4N_2O_2$) [9]. Carbon represented in black, hydrogen in white, nitrogen in blue and oxygen in red.

1.3 Direct and indirect radiation damage

Direct action of radiation occurs when the atoms of the target itself directly absorbs the primary radiation which can cause the atoms or molecules to be ionized or excited, thus initiating the chain of events that leads to a biological change. Direct damage causes effects such as DNA strand breaks that can lead to alterations in cell replication and transcription. The radiation impacts with the DNA itself, causing bond breakages between the bases and the sugar backbone of each strand of the DNA, or breakage of the hydrogen bonds between complementary bases.

The primary radiation deposits may also interact with other atoms or molecules in the environment such as the water rich nucleus of the cell to produce secondary electrons or free radicals that are able to diffuse far enough in the medium to reach and damage the critical targets [10]. The chemical environment of the DNA is a major factor in the yield of the radiation damage to the cell. This type of interaction is called indirect action of radiation.

A free radical is an atom or molecule carrying an unpaired orbital electron in the outer shell. In an atom or molecule with an odd number of electrons, there is one electron in the outer orbit for which there is no other electron with an opposing spin. This is an unpaired electron. Radicals have a high degree of chemical reactivity. The OH radical and higher order free radicals such as super oxides and nitrous oxides are capable of damaging DNA [7]. They must be produced within distances of 2 to 4 nm in order to interact with DNA based on the diffusion distance of water radicals. The OH radical is thought to be the most harmful radical as it is highly electrophilic and interacts with unsaturated sites of high electron density [11]. In reactions with the DNA backbone, the OH radical interacts by H-atom abstraction that can form a peroxyl radical in an oxygen environment which can lead to a single strand break [11].

The H_2O molecule in the environment of the DNA can become ionised.

$$H_2O \rightarrow H_2O^+ + e^-$$
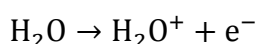
The ionised H_2O molecule is now a highly unstable free radical ion which can dissociate in the following reaction.

$$H_2O^+ \rightarrow H^+ + OH$$
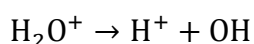
Hydrogen peroxide may also be produced as a result from the reaction

$$OH + OH \rightarrow H_2O_2$$
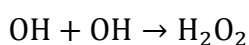
Secondary electrons are also produced as a result of indirect action of radiation. These low energy electrons (< 20 eV) are produced in large quantities (4×10^4 by a 1MeV particle) along ionization tracks [4]. These electrons being the most abundant charged particles play the dominant role in converting the kinetic energy into chemical energy causing DNA damage. Incoming secondary electrons can excite

other atoms by moving an orbital electron to a higher state or cause DNA strand breaks through electron attachment to the nucleobases within nanoscopic volumes. It has been demonstrated that electrons at energies well below ionization thresholds can induce substantial yields of single and double strand breaks in DNA by dissociative electron attachment processes [3]. Direct radiation damage to the genome in a living cell by ionizing radiation is thought to be one third of the overall damage, and damage as a result from indirect events make up the remaining two thirds of the total damage [7].
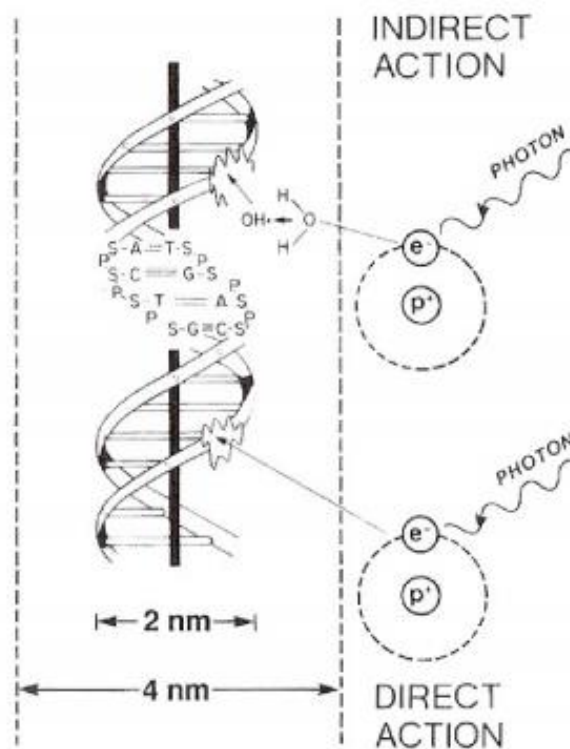
Figure 1.5. Mechanisms of interaction of ionising radiation with cellular DNA. Direct damage concerns damage directly in the DNA from energy deposition and indirect damage concerns energy disposition in biomolecules and water molecules near the DNA [7].

The effects of the radiation damage that take place occur at times that range from femtoseconds to years after the received dose. The physical stage refers to the initial stage of the received dose that occurs in the femtosecond period after the primary radiation interaction. Excitation, ionization, thermalisation and the production of free radicals from subsequent bond ruptures occur in this stage that trigger a complex cascade of reactions. The following stage is referred to as the chemical stage and involves molecular relaxation of molecules which leads to the formation of new molecules as part of the reaction. DNA repair events also take place during this stage. The main factors on deciding what DNA damage repair mechanism takes place depends on the type of damage (base and sugar damage, DNA single and double strand breaks (SSB's and DSB's), DNA-protein crosslinks, clustered damage), severity of the damage and location in the cell cycle during mitosis in which the damage occurs [7]. The final stage known as the biological stage refers to the overall biological response of the system over a large time range. Cell functions can be affected within minutes. This stage focuses on the minority of DNA strand breaks that were not repaired. Cell death and mutations to the daughter cells during replication result from this stage.

1.4 Particles produced by electron impact in the target region

The effects of low energy electron impact on DNA and nucleic acids in the gas phase can be studied using techniques like mass spectrometry. Mass spectrometry allows for detailed information on the properties of the biomolecules and the dynamics of reactions to be explored. Using a suitable detection method we can obtain information about the by-products formed as a result of electron impact collisions with the molecular beam. When electrons interact with a molecular beam in the mass spectrometer several processes can occur, including dissociative electron attachment (DEA), excitation, ionization and fragmentation (dissociation). As the energy of the primary electrons increases, the abundance and variety of the ionized species will also increase, i.e., fragmentation may occur *via* different channels, each

of which gives rise to characteristic ionized and neutral products. This includes the production of the following type of ions: molecular ions, fragment ions, multiply charged ions, metastable ions, rearrangement ions and ion pairs. It is from these products that we can extract information on the interaction. They are formed by the redistribution of atoms from the unstable parent ion. The parent ion peak will show in all mass spectra. The intensity of the parent peak will depend upon the stability of the ionised molecule which depends strongly on the structure of the molecule. As explained by the Franck-Condon principle, it is unlikely that molecular ions will be generated in their vibrational ground state. Instead, the majority of the ions created by electron impact are vibrationally excited and many of them are well above the dissociation energy level.

The ionization of the neutral sample can only occur when the energy deposited by the electron-neutral collision is equal to, or greater than the ionization energy (IE) of the corresponding neutral. The ionization efficiency is close to zero however if the electrons are carrying just the IE of the sample.

$$M + e \rightarrow M^+ + 2e$$
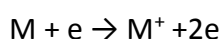
where M is the molecule (uracil in this experiment) and M^+ is the ionized molecule which is identical in molecular weight. The minimum energy needed to be transferred to the neutral M to all allow for the detection of the fragment ion M^{n+} in most organic molecules is between 9 and 15 eV [12].

The fragmentation of biomolecules provides valuable insights into their formation. Neutral species in the ground state and metastable (long lived excited state) products are very difficult to detect and are not analysed in this experiment. The positive ions are detected and resolved into mass spectra, in our case using a

reflectron time of flight mass spectrometer described in chapter 3. The amount of energy needed to be transferred to the neutral M to allow for the detection of the fragment ion M^+ is called the appearance energy of that fragment ion. A common rearrangement in nucleobase dissociation is the transfer of a hydrogen atom or migration of an alkyl group. The results published by Pan et al [13] indicate that H arises principally from the bases and the sugar ring of the backbone and O is produced from fragmentation in the backbone of the helix. The more atoms that are contained within a molecule the easier it finds a way for stabilization of the charge. Once the molecular ion is formed, the electron charge is never really localized in a single orbital, although assuming so is often a good working hypothesis for mass spectral interpretation [14].

1.5 Low energy electron impact studies

1.5.1 Low energy electrons in DNA damage

Many groups have performed studies on the effects low energy secondary electrons have on DNA; see the review by Sanche [3]. Secondary electrons are generated in great abundances along ionization tracks with energies in the range of 1- 30 eV. These secondary electrons were believed not to initiate any damage to the DNA structure until in 2000 when Sanche et al presented findings that showed the induced damage to nucleic acids, in the form of single and double strand breaks. The group used an electron beam over the energy range of 3–30 eV to irradiate plasmid DNA. The initial findings on plasmid DNA showed strong bond breaking peaks at 10 eV, both single and double bond breaks occur with a ratio 4 to 1. Single and double strand breaks can be generated through electron attachment to the DNA strand followed by bond breaking due to energy transfer to an anion.
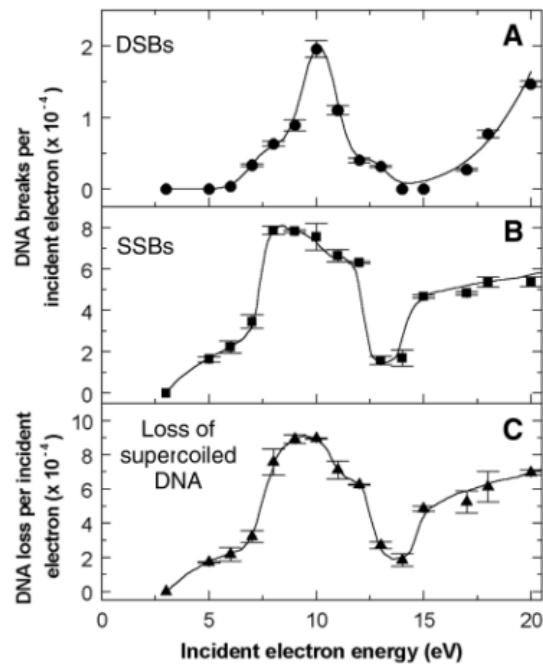
Figure 1.6. Measured quantum yields, per incident electron, for the induction of DSBs (A), SSBs (B), and loss of the supercoiled DNA form (C), in DNA solids by low-energy electron irradiation as a function of incident electron energy by Ptasińska et al [15].

In 2005 L. Sanche et al [16] concluded that below 15 eV bond ruptures in DNA and its bases occur *via* the formation of transient anions decaying into dissociative electronically excited states or into a dissociative electron attachment (DEA) channel. Above 15 eV direct scattering causes bond rupturing but transient anions still cause damage up to 40 eV. One of the main factors involved in DNA induced damage is the lifetime of the transient anions. Experimental work has led to a proposed model for the resonance interaction of low energy electrons with DNA. The incoming low energy electron is captured forming a core excited resonance on a DNA base at energy E_0 or close to or above the first electronic excitation energy threshold forming a transient anion. This anion can decay by one of the following channels:

1. Elastic channel - The electron is re-emitted with the same incident energy. It can be emitted back into vacuum or transferred within the strand.

2. Inelastic channel – The base becomes electronically excited along with the release of a low energy electron into vacuum or transferred within the strand.

3. DEA channel – Fragmentation of the base itself occurs.

The molecule AB combines with an electron, e^-, to form a super excited anion AB^{-*} which dissociates into the fragments, A^- and B or A + B^-.

$$AB + e^- \rightarrow AB^{*-} \rightarrow A + B^- \text{ or } A^- + B$$
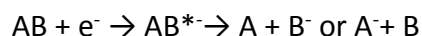
where A and B can be single atoms or a different combination of atoms.

Generally DEA processes have very large cross sections of hundreds to thousands of $Å^2$, which are much larger than cross sections for direct electron or photon induced dissociation.

Sanche showed the uracil transient anion decays as follows as a result from resonant electron capture. Figure 1.7 shows four absolute partial cross sections for dissociative electron attachment to uracil leading to, respectively, $C_4H_3N_2O^-$, $C_3H_2NO^-$, OCN^- and CN^- ions as a function of electron energy

$$e^- + U \rightarrow U^{-*} \rightarrow (U - H)^- + H^*$$
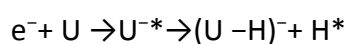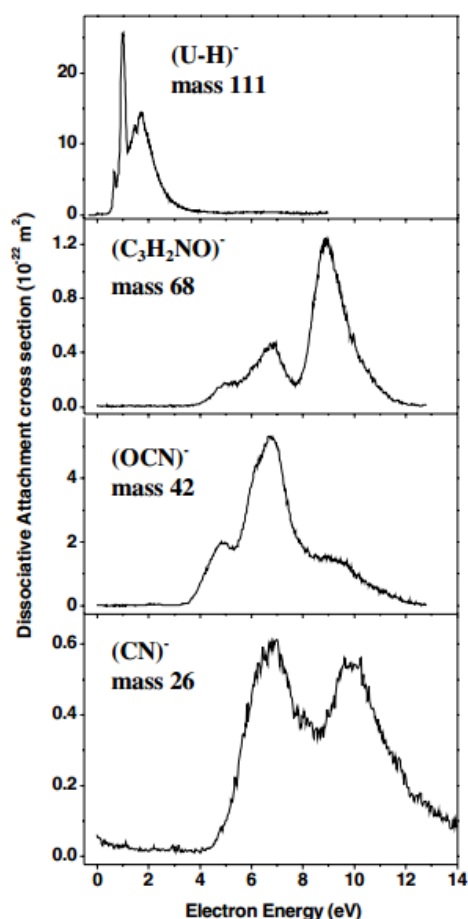
Figure 1.7. Absolute partial cross sections for dissociative electron attachment to uracil as a function of electron energy measured by Denifl et al [17]. (U-H)⁻ refers to the $C_4H_3N_2O_2^-$ ion.

Results on Calculated cross sections for low energy resonant electron attachment to different bases also show that the influence of functional groups on bond and site selective dissociation plays an important role. The cross section for bromouracil is two orders of magnitude larger than thymine [18]. With the knowledge that some bases are more sensitive to ionizing radiation than others, it is possible to control chemical reactions by using specific electron impact energies based on their cross sections.

1.5.2 Dissociative electron attachment studies

Dissociative electron attachment investigations were conducted by Pan et al [13]. Synthetic base pair linear DNA and natural plasmid DNA which was purified from bacteria were bombarded with low energy electrons. The linear DNA was formed from complementary oligonucleotides, 40 nucleotides in length, purified by polyarcylamide gel electrophoresis. The samples were transferred after preparation to a rotary target holder housed in an UHV chamber via a gate valve. The samples were then irradiated by an electron beam of 1.5 nA incident on a 4 mm spot with an energy spread of 0.5 eV full width at half maximum.

The experiment showed that DEA is the process involved in low energy electron induced DNA damage. The maximum intensity at which DEA occurs was found to be 9 -9.5 eV which is close to the maximum in the yields of single strand and double strand breaks by low energy electrons. A break in one strand of the molecule can cause an anion or radical to be produced that can induce another strand breakage when scattered. The results indicate that H arises principally from the bases and the sugar ring of the backbone and O is produced from fragmentation in the backbone. The incident electron energy dependence of H, O and OH yields from 40 base pair DNA is represented by curve A in figure 1.8. These yields exhibit a single broad peak near 9 eV with a continuous rise at higher energies. The result of low energy electron bombardment of natural DNA is represented by curve B and it exhibits the same characteristics as shown in A. Curves C, D and E exhibit the H yield functions from films of thymine, amorphous ice and α-tetrahydrofuryl alchohol. DEA is shown to be the main process involved in the main H desorption pathway. The H peak from amorphous ice in curve D is too low to be associated with DEA.
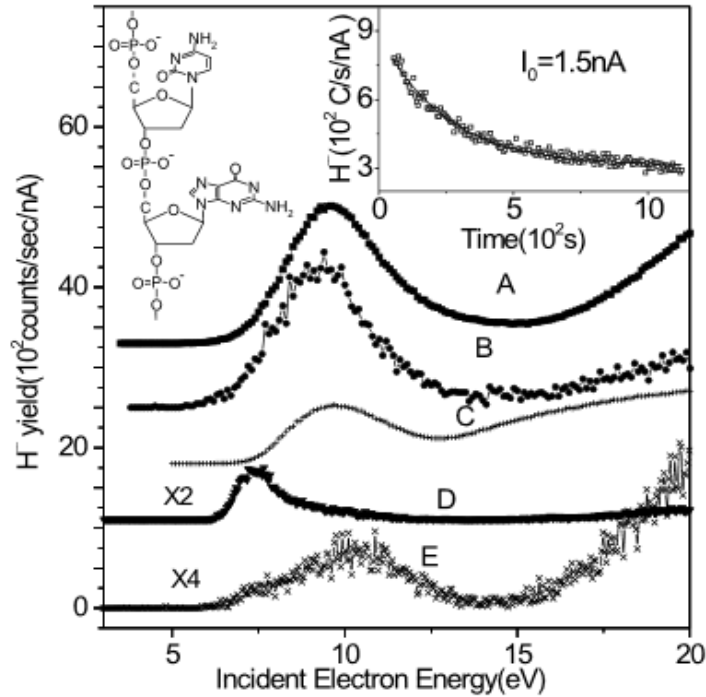
Figure 1.8. Incident electron energy dependence of H yields (i.e., the H yield function) from thin films of: (A) double stranded linear DNA, 40 base-pairs, (B) supercoiled plasmid DNA, (C) thymine, (D) water, and (E) a ribose analog. [13]

Part of a single DNA strand is shown in the upper left. The dependence of the magnitude of the H signal on time of exposure to the electron beam is shown by the open squares in the upper right inset. The solid line is an exponential fit to the data.

1.5.3 Vibrational Feshbach Resonances

Electron impact studies of the dissociative electron attachment (DEA) process in the RNA base uracil have revealed sharp structures at energies below 3 eV that have been identified as vibrational Feshbach resonances. Burrow et al [19] have attributed the sharp peaks observed in the DEA cross sections of uracil as shown in figure 1.7 at energies below 3 eV to vibrational Feshback resonances, in which the electron is weakly bound to a vibrationally excited level of the molecule.

Uracil possesses a well studied dipole bound anionic state (DBS) below the neutral molecular ground state. A resonance is formed when the incoming electron with energy close to the resonance energy is captured into a low lying unoccupied molecular orbital. Resonances (typical lifetime range 10^{-15} to 10^{-11} s) are often found to dominate the dynamics of electron molecule collisions over the energy range 0–10 eV. During the lifetime of the resonance the nuclei start to move to larger distances under the influence of the destabilizing force brought into the system by the captured electron. When the electron leaves the negative ion complex by autodetachment, the nuclei are at a distance substantially larger than the equilibrium distance of the neutral molecule, i.e. in a vibrationally excited state. If the lifetime is sufficiently long to allow propagation of the nuclei to large distances, dissociative attachment occurs. DEA can induce bond selective molecular fragmentation. This can occur at well defined reaction sites, leading to almost 100% bond selectivity and thus initiating controlled chemical processing in the local environment [20]. The resonant state can either decay by the emission of the extra electron leaving the molecule in the ground state or in a vibrationally exited state or can dissociate into several fragments.

1.6 Mass spectrometry studies of uracil

Experiments using techniques such as electron impact *via* DEA or ionization, ion impact and photon impact on the nucleobases guanine, cytosine, thymine, uracil, and adenine have all been performed. This section outlines the fragmentation pathways that occur in uracil, and details the major experiments that have been conducted using uracil and the results obtained. The experimental results will be compared with results from Maynooth in chapter 6.

1.6.1 Electron impact ionization of neutral gas phase uracil.

Rice et al [21] studied the fragmentation patterns of uracil by recording mass spectra at 20 and 70 eV electron impact energies. Approximately 50 - 100 µg of uracil was introduced directly into the ion source of a double-focusing mass spectrometer. The source was heated to 200° C in order to generate a sufficiently high vapour pressure. They identified the molecular ion peak at 112 u and intense fragment ion peaks at 69 and 42 u corresponding to the succesive loss of HNCO and HCN in the 70 eV mass spectrum. The 69 u fragment is also prominent in the 20 eV mass spectrum. They were one of the first groups to study the primary decomposition of uracil following electron impact on uracil.

Ulrich et al [22] have performed mass spectrometry following 70 eV electron impact on uracil, thymine, and related molecules by using an AEI MS-9 mass spectrometer. They could confirm several of the fragmentation pathways proposed by Rice et al [21] on the electron impact mass spectra of uracil. These pathways were established in part by making use of metastable peaks and isotope labeling.

S. Denifl et al [5] measured ionization yield curves for the uracil parent ion and eight other intense fragment ions at an electron impact energy of 70 eV in order to determine the corresponding appearance energies. The experiment was performed

with a crossed molecular beam in combination with a quadrupole mass filter. The ionization yield curves were normalized with the electron current in order to eliminate the influence of a changing electron current when scanning the electron energy. The cations formed by the electron impact of the neutral uracil beam were extracted from the interaction region by a weak electrostatic potential towards the entrance of a quadrupole mass spectrometer. The mass selected ions were then resolved and detected by a channeltron. The measured ionization yield curves were fitted with a non linear fit function for the determination of the appearance energies.
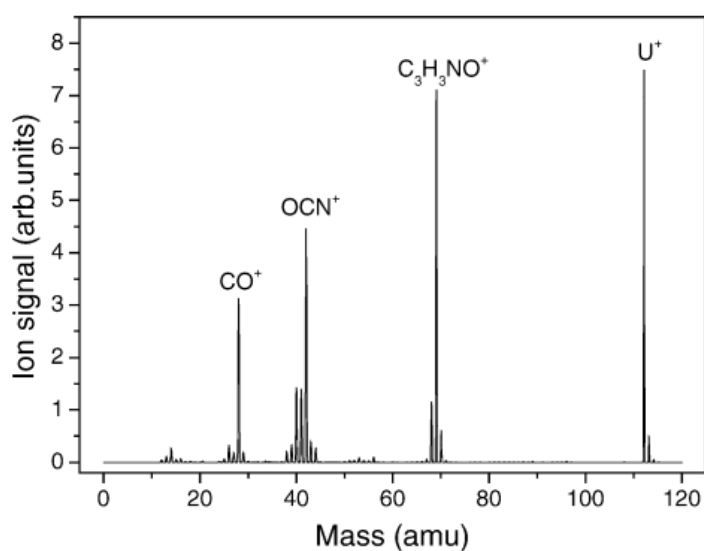
Figure 1.9. Mass spectrum of uracil measured at the electron energy of 70 eV by Denifl et al [5]. The parent ion appears at mass 112 amu with the most abundance of all product cations.
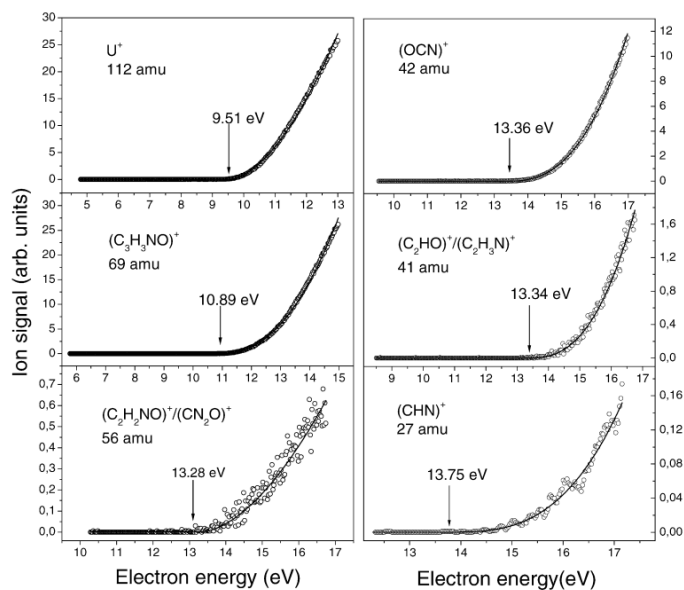
Figure 1.10. Ionization yield curves near the threshold region for the formation of uracil cations from neutral uracil by electron impact presented by Denifl et al [5]. The measured data are shown as open circles whereas the fit curves are shown as solid lines. The appearance energies are indicated by arrows.

They found the most abundant fragment cations of uracil to be $(C_3H_3NO)^+$, 69 u, $(OCN)^+$, 42 u and $(CO)^+$, 28 u. They found the parent ion has an appearance energy value of 9.59 ± 0.08 eV which was the lowest appearance energy value of all the measured cations. The values they found for the adiabatic ionization energy are significantly lower than the value for the vertical ionization energy. They claim uracil exhibits behaviours similar to other molecules, such as C_6H_6 and C_3H_8 indicating a direct ionization mechanism in the electron impact event. Such results may be explained by an indirect ionization mechanism via the excitation of a Rydberg state with subsequent associative ionization within the molecule [23].

Imhoff et al [24] studied the chemical composition and formation channels of charged fragments of uracil and 5-bromouracil produced by 70 eV electron impact in the gas phase. Films of uracil and 5-BrU were prepared *via* vacuum evaporation

and condensation on a polycrystalline Pt foil substrate held at room temperature. The oven was heated to 90 – 100°C to yield an appropriate molecular deposition rate, which was then placed in front of the entrance of a quadrupole mass spectrometer. Fragmentation patterns of the molecules induced by 70 eV electron impact were collected using a built-in ionizer in the quadrupole mass spectrometer after careful baking of the vacuum system to reduce background signal. (They also subtracted a background spectrum taken immediately prior to the sample evaporation)

Feil et al [25] reported total ionization cross sections up to 1000 eV for uracil by normalizing their values at 100 eV with theoretical data and absolute partial cross sections for the formation of selected positive and negative ions resulting from electron interactions with uracil. The experiment was carried out using a double focusing two sector field mass spectrometer. They recorded relative partial ionization cross sections for the three most intense mass selected ions in their mass spectrum (the parent $C_4H_4N_2O^+$ ion and the $C_3H_3NO^+$ and OCN^+ fragment ions) for electron energies from threshold to 1000 eV. The parent ionization cross section was found to have the largest peak value of about 4.4×10^{-20} m^2 (at about 100 eV) whereas the two fragment ions have cross sections that peak around 2.2×10^{-20} m^2 at a slightly higher impact energy.

Shafranyosh et al [26] used a crossed molecular and electron beam to study the electron impact on uracil. The electrons in the beam that passed the collision region were captured by a Faraday cylinder that had a positive potential. The cross-sections of the formation of positive and negative ions of uracil were obtained experimentally. The magnitudes and the energy dependence were determined for the cross-section of formation of positive uracil ions in the electron energy interval from the formation threshold to 200 eV. The ionization cross section peak of $1.0 \pm 0.1 \times 10^{-15}$ cm^2 was found at an energy of 95 eV.

M.A. Rahman and E. Krishnakumar have recently measured absolute partial and total electron ion cross sections for uracil up to 500 eV using the well-known relative flow technique [27]. They also present thresholds for the formation of various fragment ions for uracil and the comparison of total ionization cross section with existing results. They measured ion yield curves for the energy range of 0–500 eV for all prominent ions. The appearance energies (AE) were obtained using a linear fit method near threshold. They measured the relative intensities of four principal fragments $HNCH^+/CO$ (28 u), OCN^+ (42 u), $C_3H_3NO^+$ (69 u) and uracil parent ion (112 u). They found that there is considerable differences in the relative intensities in various measurements.

Theoretical studies involving electron impact include R-matrix calculations by Dora et al [28]. Mozejko and Sanche [29] also reported total ionization cross sections for all nucleobases using BEB formalism. Vinodkumar et al [30] have reported total ionization calculations for DNA and RNA bases using Spherical Complex Optical Potential (SCOP) model and scattering theory.

1.6.2 Photo ion mass spectrometry of uracil

A number of groups have looked at photo fragmentation of uracil. We only list one recent references as the focus of this paper is on electron impact. Jochims et al [31] conducted a study on photo ionization mass spectrometry of uracil. In their experimental setup synchrotron radiation in the 6–22 eV photon energy range was focused into a differentially pumped gas cell and heated to excite the source. The uracil sample was introduced into the ionization chamber by direct evaporation below the position of the incident VUV radiation within the ion extraction zone. The whole chamber was heated to between 120°C–140°C. Fragment ions formed by photo ionization of the uracil parent molecule were measured and analysed using a quadrupole mass spectrometer.

The photo ionization mass spectrometry study of uracil revealed VUV-induced degradation pathways of uracil. They found the principal fragmentation pathway of the uracil parent cation involves the loss of the HNCO molecule to give rise to the 69 u ion, $C_3H_3NO^+$. The principle fragmentation decay routes shown in figure 1.11 are similar to the assigned decay routes by Rice et al shown in chapter 6. Shown below in figure 1.12 are the selected ion yield curves for the main fragments.
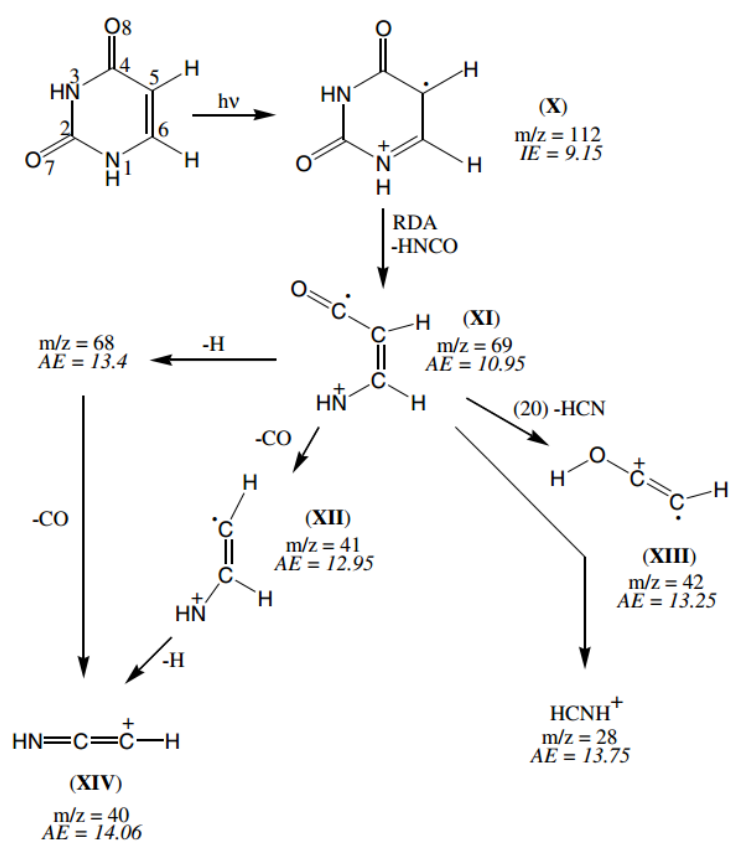
Figure 1.11. Principal fragmentation decay routes of the uracil radical cation proposed by Jochims et al [31].
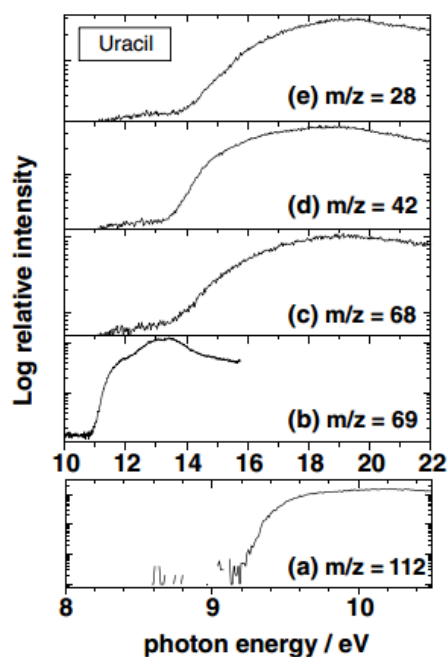
Figure 1.12. Selected ion yield curves of uracil measured by Jochims et al [31].

1.6.3 Proton impact induced ionization of uracil

Tabet et al [32] conducted an experiment on proton impact induced ionization of uracil. Protons were produced in a standard RF gas discharge source (80 MHz) and accelerated to 80 keV with an energy resolution ($\Delta E/E$) of 0.01. The primary magnetic sector field separated the protons from the other ions in the source. The background pressure was maintained below 10^{-6} mbar. The proton beam was crossed with the molecular target beam. The charge state of the projectile after the collision was determined using a second magnetic sector field mass analyzer with three channeltron detectors to detect H^+, H neutral, and H^-. A linear time-of-flight (TOF) mass spectrometer analyzed the uracil product ions formed by proton collisions. By simultaneously determining the mass per charge ratio of the product ions and the post interaction charge of the projectile, the experiment enabled direct ionization detection (detection of H^+ from secondary magnetic analyzer) to be

distinguished from electron capture (coincident product ion and H neutral detection) for each ionization event.
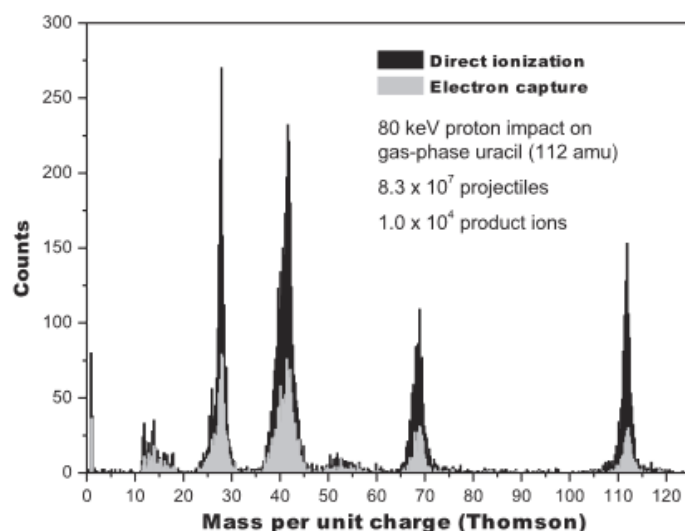
Figure 1.13. Mass spectrum for proton impact ionization of uracil by electron capture and direct ionisation measured by Tabet et al [32].

They found fragmentation patterns for the ionization of a nucleobase as a function of proton impact velocity in the range coinciding with maximum energy deposition (the Bragg peak) with the distinction between electron capture events from direct ionization events. No fragment ions were identified above 90 u. They suggest that the weakness of any production of ions with six or seven heavier atoms is that the dissociative ionization of gas phase uracil following proton impact occurs almost exclusively *via* cleavage of the central aromatic ring. Bond rearrangements were shown to occur prior to the fragmentation of quite similar metastable polyatomic cations to uracil[+]. They conclude that the major peak at 42 u was attributed to CNO^+, $C_2H_4N^+$, and $C_2H_2O^+$. They found that ionization pathways involving high energy deposition were found to increase the likelihood of multiple bond cleavage and fragmentation prior to nuclear rearrangement.

1.7 Overview of experiment

This chapter provides a brief introduction into radiation damage and the biological effects caused by radiation damage to the genome. We pay particular attention to low energy secondary electrons and we give a summary of some significant findings of the effects low energy electrons have on DNA and nucleic acids in the gas phase. We also describe the structure of DNA, RNA and uracil.

The purpose of this research is to study low energy electron impact induced dissociation and fragmentation of uracil. The work has several objectives including obtaining partial ionization cross sections for positive fragments produced by electron impact on uracil, determining appearance energies for positive fragments, and identifying and comparing fragmentation pathways of uracil. Chapter 2 of this thesis provides a brief overview of the principles of mass spectrometry and the reflectron time-of-flight mass spectrometer used for this research. Chapter 3 gives a description of the apparatus used for the research discussed in this thesis. Chapter 4 gives a description of the interfacing and timing scheme of the equipment and describes the LabVIEW software programmes used for data analysis, data acquisition and peak fitting. Chapter 5 gives a description on the calibration of the electron gun, mass spectra and the electron impact energy. Chapter 6 presents the results from electron impact on uracil. Chapter 7 presents the results from electron impact on uracil using the supersonic source.

Chapter 2: Principles and Instrumentation of Mass Spectrometry

2.1 What is mass spectrometry?

Mass spectrometry evolved from the effects magnetic and electrostatic fields had on ions. The purpose of mass spectrometry is to generate ions from organic or inorganic compounds and to separate and resolve the ions with respect to their mass to charge ratios *(m/q)*. Analysis can be done to determine their respective *m/q* and abundance. The mass spectrometer consists of an ion source which converts the molecules in a gas phase sample into ions, a mass analyser to separate the ions by their masses and a detector to detect the incoming ions. It is one of the most important analytical techniques used to get information about the molecular structures of organic or synthetic compounds, making it applicable in many fields of science. Scientific breakthroughs made possible by mass spectrometry have included the discovery of isotopes, the exact determination of atomic weights, characterization of new elements, quantitative gas analysis and the characterization of molecular structure [33]. Discussed in this chapter are the principles and techniques used in a time of flight mass spectrometer, mass filters and mass spectrometers using ion traps.

Figure 2.1 shows the general components for the majority of mass spectrometers. The inlet system introduces a small quantity of the sample into the ion source as a gas at low pressure. Various ion sources can be used in mass spectroscopy such as an electron impact source, a chemical ionization source, or a gas discharge ion source. A mass analyzer is the component of the mass spectrometer that takes ionized molecules and atoms and separates them based on their charge to mass ratios and outputs them to a detector. The residual gas pressure in the active volumes of these components must be kept to a minimum, therefore vacuum

systems are an important part of mass spectroscopy. Important characteristics that mass analyzers should posses are [12]

1. High detection efficiency
2. High resolving power
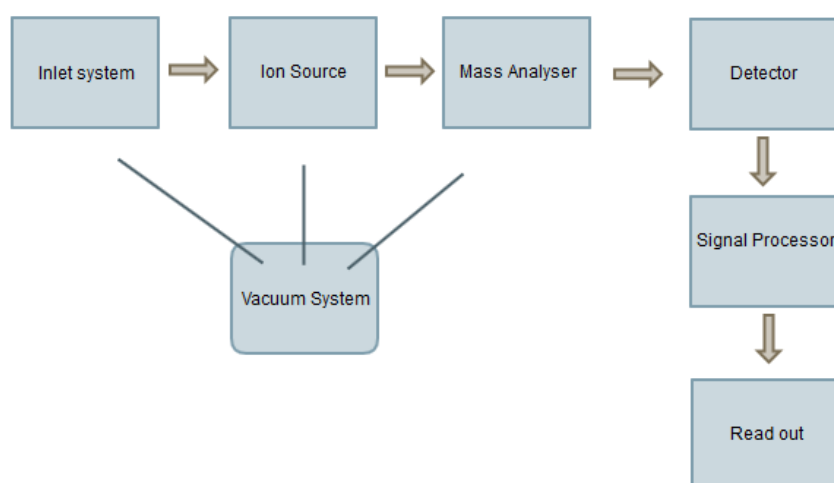
Figure 2.1. Components of a mass spectrometer

2.2 Types of mass spectrometers

2.2.1 Single focusing mass spectrometer

Single focusing mass spectrometers are based on how ions with different m/q ratios at equal kinetic energies behave in a magnetic field. Positive ions formed in the ion source are accelerated between two plates by a potential difference of a few thousand volts. The ions pass through an aperture and are deflected by a magnetic field. The trajectories the ions take in a uniform DC magnetic field are dependent on the m/q ratio of the ions. The ions that pass through a collector aperture reach a detector and a signal is produced. The intensity of the resulting peak is proportional to the abundance.

2.2.2 Double focusing analyser

Single focusing analysers fail to resolve for small mass differences in a sample because of the small variation in the kinetic energy of the particles emerging from the source. In order to achieve better resolution the energy spread of the ion packets must be reduced before they enter the magnetic field. Double focusing mass spectrometers were first designed by Mattauch and Herzog [34]. The ion beam is first passed through a radial electrostatic field which focuses only particles of the same kinetic energy onto a second slit and the particles from this point are separated by a magnetic field until they reach a detector at a third point. This arrangement can distinguish between particles that differ slightly in mass giving it high resolving power. However this method produces low ion currents.

2.2.3 Quadrupole mass spectrometer

A quadrupole mass filter consists of four cylindrical metal rods arranged symmetrically around the ion beam. Two opposite rods have an applied positive potential ($U + V \cos\omega t$) consisting of a DC (U) and a varying radio frequency AC component ($V \cos\omega t$) and the other two opposing rods are connected to a negative potential of -($U + V \cos\omega t$). The positive DC potential is applied to the rods in the X-Z plane and the negative DC potential is applied to the rods in the Y-Z plane. The ions are separated in a quadrupole based on the stability of their trajectories in the oscillating field. By suitable adjustment of the DC potential and the time dependent AC potential, only ions of certain m/q values pass through the quadrupole filter. It is important to note the fields do not accelerate the ions. A mass spectrum can be obtained by varying the voltages such that ions of successively higher masses are detected. Quadruple mass filters are in common use today due to their relatively small size, light weight, low cost and rapid scan times (less than 100 ms).
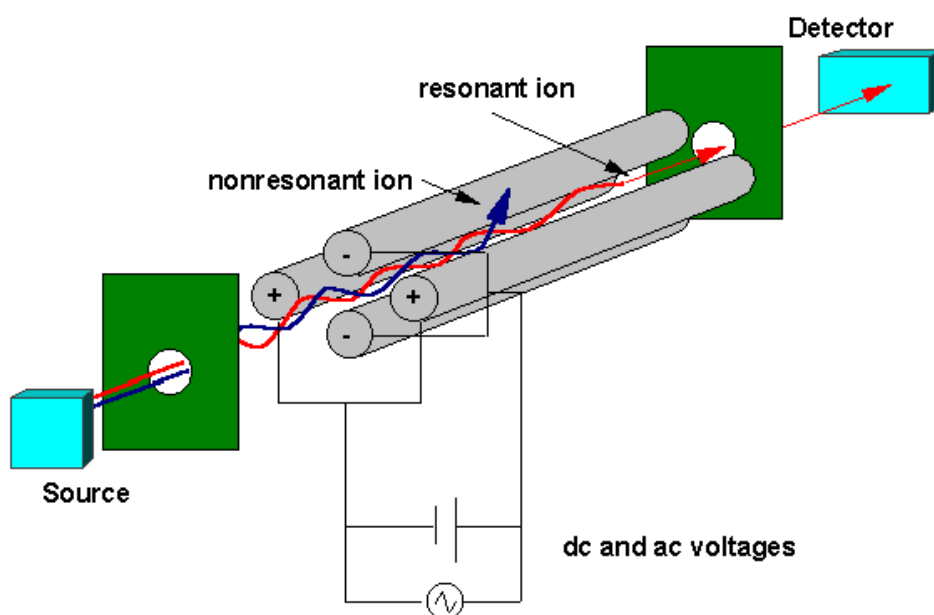
Figure 2.2. Example schematic of a quadrupole mass filter [35]

2.2.4 Mass spectrometry using traps

A quadrupole ion trap is a type of ion trap that uses dynamic electric fields to trap charged particles. The quadrupole ion trap functions both as an ion store in which gaseous ions can be confined for a period of time and as a mass spectrometer of considerable mass range and variable mass resolution. The quadrupole ion trap consists of two hyperbolic metal electrodes with their foci facing each other and one hyperbolic ring electrode halfway between the the two hyperbolic electrodes. The ions are trapped in the space between these three electrodes by AC (oscillating) and DC (static) electric fields. The AC radio frequency voltage oscillates between the two hyperbolic metal end cap electrodes if ion excitation is desired; the driving AC voltage is applied to the ring electrode [33]. All the ions that enter the entry electrode independent of their mass are trapped in a three-dimensional trajectories in the space between the electrodes by AC and DC electric fields. Ions are expelled according to their masses to create a mass spectrum. The ions repel each other in

the trap which causes an expansion of their trajectories as a function of time. The ion trap is typically filled with helium to avoid ion loss. Collisions with helium dampen the kinetic energy of the ions and serve to quickly contract trajectories toward the center of the ion trap [12].

As each ion species leaves the ion trap in turn, the ions impinge upon an external detector, creating thereby a series of ion signals dispersed in time which constitutes a mass spectrum. Ejection of ions from the potential well is accomplished by ramping in a linear fashion the amplitude of a radiofrequency (r.f.) potential applied to one of the ion trap electrodes; each ion species is ejected from the potential well at a specific r.f. amplitude and, because the initial amplitude and ramping rate are known, the m/q ratio can be determined for each ion species upon ejection.
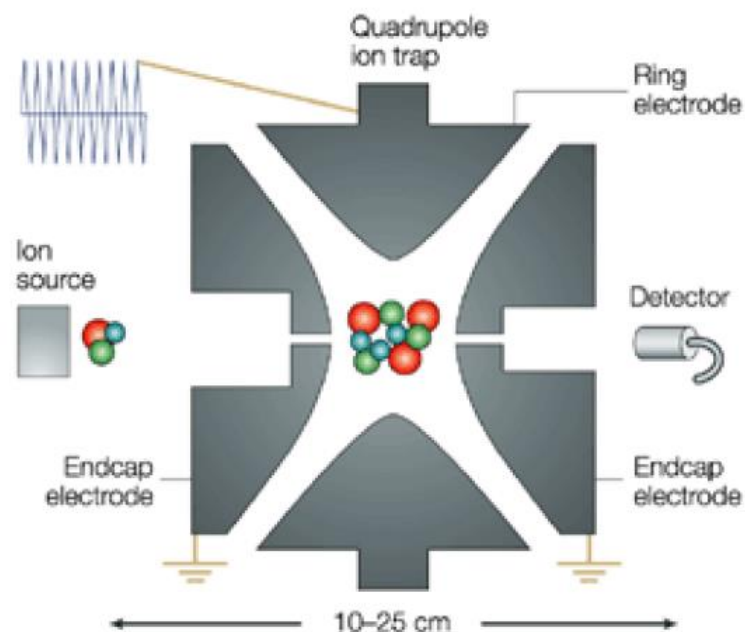

Figure 2.3. Example schematic of a quadrupole ion trap [36]

2.3 Time of flight mass spectrometry

Time of flight mass spectrometrs (TOFMS) are a type of mass spectrometer in which an ion's mass to charge ratio m/q is determined *via* a time measurement. TOFMS differ fundamentally from scanning instruments in that they involve temporally discrete ion formation and mass dispersion principally in the time domain rather than along a spatial axis.

Ions are extracted from a pulsed ion source. Pulsed ionization is achieved using a pulsed laser or a pulsed electron beam. The time taken for the ions to travel the flight tube is dependent on their mass to charge ratio assuming all the ions receive the same kinetic energy. The separation of the ions is not dictated by the use of electric or magnetic fields like the other mass analysers but on the time taken for the ions to be detected. If the length of the path taken by the ions, the potential applied to accelerate the ions between the electrodes and the extraction grids are held constant, the ions will have a corresponding distribution of flight times in which time of flight is inversely proportional to the square root of m/q. A mass spectrum is accumulated by collecting the ions from a large number of laser or electron pulses.

Time of flight analysers have the advantage over single focusing analysers because they depend on electronic circuits rather than extremely accurate mechanical alignment and highly uniform stable magnetic fields [37] and an advantage over mass filters that they can measure a larger mass range making time of flight analysers suitable for measuring clusters. The concept of time-of-flight (TOF) analysers was first described by Stephens in 1946 [38]. Wiley and McLaren published in 1955 the design of a linear TOF mass spectrometer which later became the first commercial instrument [39]. The reflectron time of flight mass spectrometer (RTOFMS) increases the flight path without increasing the dimensions of the mass spectrometer and provides second order focussing in flight time. The RTOFMS used for this project will be discussed in section 2.5.

The TOF mass spectrometer requires a calibration equation to relate and convert the flight time of the ions to a mass value. The relationship between t and $\sqrt{\frac{m}{q}}$ is linear and can be written as (refer to paragraph 2.4)

$$t = A\sqrt{\frac{m}{q}} + B \qquad\qquad (2.1)$$

Inversion of this equation gives

$$\frac{m}{q} = (Ct + D)^2 \qquad\qquad (2.2)$$

where $C = 1/A$ and $D = -B/A$.

2.3.1 Time of flight resolution

The mass resolution of time of flight mass spectrometers is affected by factors that create a distribution in flight times among ions with the same *m/q* ratio. These are

1. The length of the ion formation pulse (time distribution), for example the width of the electron pulse or laser pulse,
2. The size of the volume where the ions are formed (space distribution),
3. The variation of the initial kinetic energy of the ions produced by molecular fragmentation (kinetic energy distribution)

An ion packet with a given ratio m/q focused near the source contains ions with a set of energies due to the difference in the paths traversed by the ions in the field of the extracting pulse. In moving through the field-free space the ion packet expands as the result of the difference in ion velocities. To reduce the kinetic energy spread among ions with the same *m/q* ratio leaving the source, a delay between ion formation and extraction can be introduced. The ions are first allowed to expand into a field-free region in the source and after a certain delay a voltage pulse is applied to extract the ions outside the source. Delayed extraction compensates for the initial momentum of the ions, it provides the same arrival times at the detector for ions with the same *m/q* ratios but with different initial velocities. The energy focusing can be accomplished by adjusting the amplitude of the pulse and the time delay between ion formation and extraction.

2.4 Reflectron time of flight mass spectrometer

A reflectron is a type of time of flight mass spectrometer that comprises a pulsed ion source, field-free region, ion mirror (reflector), and an ion detector. The reflector uses a static or time dependent electric field to provide second order focussing of the ion beam towards the detector. The reflectron time of flight mass spectrometer was proposed for the first time by Mamyrin [40]. The reflectron accomplishes space-time focusing of ion packets with high resolution. An einzel lens arrangement is used to focus the ion beam at the entrance of the mass spectrometer. In moving through the field-free space the ion packets expand as the result of the difference in ion velocities. As the ion packets reach the end of the first portion of the flight path a reflecting system (reflector) is in place in the form of a uniform electrostatic field. The field created in the reflector is at the end of the flight tube. The polarity of the field is the same as the ions so they experience a retarding potential that acts as an ion mirror by deflecting the ions and sending them back through the flight tube. With an appropriate choice of parameters of the reflecting system, the time of movement of ions from the source to the detector

can be measured. Depending on the voltages applied to the instrument the reflectron can either resolve positive or negative ions. The reflector is situated behind the field-free region opposite to the ion source. The detector is positioned on the source side of the reflecter to capture the arrival of ions after they are reflected [37]. The reflector diminishes the spread of flight times among ions with the same *m/q* ration caused by a spread in kinetic energy of these ions at the exit from the ion source. Ions with more kinetic energy will penetrate the reflector more deeply than ions with lower kinetic energy. Consequently, the faster ions will spend more time in the reflector and will reach the detector at the same time as slower ions with the same *m/q*. For this project a reflectron time of flight mass spectrometer (RTOFMS) by R.M. Jordan Company was used to detect the ions. A schematic of the reflectron time of flight mass spectrometer used in this project is shown in figure 3.11.

The relationship between *m/q* and time is discussed here. The time taken for an ion in a RTOFMS can be written as [41]

$$t = A_0 \left[\frac{A_1}{\sqrt{k}} + A_2\left(\sqrt{k} - \sqrt{k-p}\right) \right] = A_0 F \qquad (2.3)$$

Assuming the extraction potential of the source to be $U = kU_0$ where qU_0 is the mean ion energy and *qU* the ion energy corresponding to the ion velocity components, *k* is a factor close to unity (k_0=1), $p = \frac{U_b}{U_o}$

 we define the following quantities independent of *m, q*

$$A_1 = \frac{L_1 + L_2}{4d_r U_0}$$

34

$$A_2 = \frac{d_b U_r}{d_r U_b}$$

where U_b is the potential in the decelerating gap d_b, U_r and d_r are the distance and potential difference between the reflector electrodes respectively $L1$ and $L2$ are the lengths of the flight paths that cover the length of the field free drift space and reflecting field,

$$A_0 = \frac{4d_r}{\sqrt{\frac{2qU}{m}}} \frac{U_0}{U_r}$$

$$A_0 = \frac{4d_r}{\sqrt{2U}} \frac{U_0}{U_r} \sqrt{\frac{m}{q}}$$

Inserting quantities $A1$, $A2$ and $A0$ into equation (2.3) the ion flight time becomes

$$t = A \sqrt{\frac{m}{q}}$$

$$A = \frac{4d_r}{\sqrt{2U}} \frac{U_0}{U_r} \left[\frac{A_1}{\sqrt{k}} + A_2 \left(\sqrt{k} - \sqrt{k-p} \right) \right]$$

The resolution $\left(\frac{m}{\Delta m}\right)$ observed with the TOF mass can be measured in terms of $\left(\frac{t}{\Delta t}\right)$ as follows:

$$\frac{m}{q} = (Ct + D)^2 \tag{2.2}$$

$$\frac{1}{q}dm = C2tdt$$

$$\frac{m}{dm} = \frac{t}{2dt}$$

$$R = \frac{m}{\Delta m} = \frac{t}{2\Delta t}$$

Therefore, the resolution R in TOF mass spectrometry is equal to [33]

$$R = \frac{m}{\Delta m} = \frac{t}{2\Delta t} \approx \frac{d}{2\Delta x} \tag{2.4}$$

where m and t are the mass and flight time of the ion, and Δm and Δt are the peak widths measured at the 50 % level on the mass and time scales, respectively, d is the flight distance taken by the ions and Δx is the thickness of an ion packet based on the factors listed in section 2.3.2. A solution to increase the resolution of a time of flight mass spectrometer is to increase the flight path. However, too long a flight tube decreases the performance of TOF analysers because of the loss of ions by scattering after collisions with gas molecules or by angular dispersion of the ion beam. It is also possible to increase the flight time by lowering the acceleration voltage. But lowering this voltage reduces the sensitivity. To obtain both high resolution and high sensitivity a long flight tube with a length of 1 to 2 m is commonly used [33].
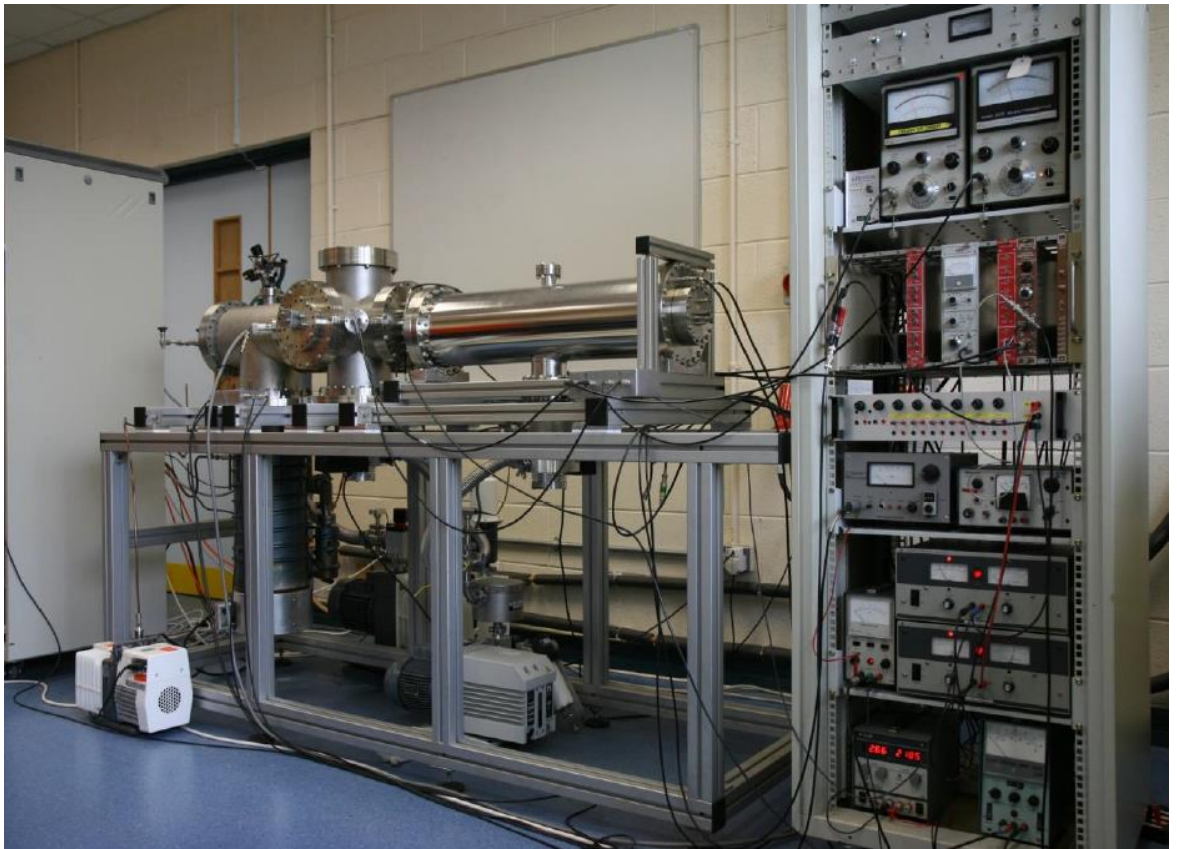
Chapter 3: Experimental Set up

Figure 3.1. Experimental setup used for this project.

3.1 Introduction

In this chapter the apparatus used for the research in this thesis is described. The main components of the apparatus are discussed individually in detail. A description of the interfacing set up of the equipment is provided in chapter 4. Calibration tests will be presented in chapter 5.
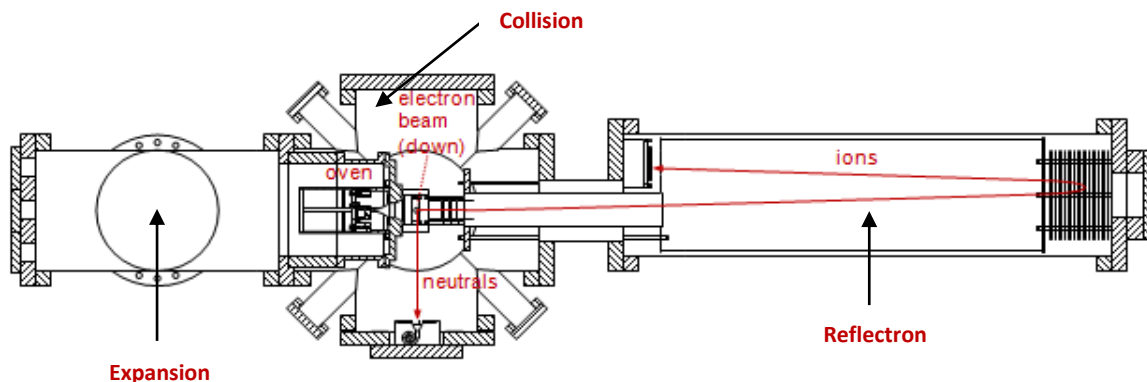
Figure 3.2. Diagram of the experimental apparatus

The apparatus consists of three chambers shown in figure 3.2: the expansion chamber where a beam of uracil is produced, the collision chamber where the uracil molecules are ionised and fragmented, and the flight tube which contains the reflectron time of flight mass spectrometer and the micro channel plate detector where the reaction products are detected. Five pumps are in use to keep a suitable vacuum throughout the system. It is necessary to evacuate the chamber to prevent air molecules from interfering through chemical reactions and contaminating clean surfaces inside the chamber. Copper gaskets and viton O-Rings are used to join the chambers together. The chambers are supported by an aluminium frame, which has sliding rails allowing the chambers to be disconnected and moved apart to access the components in the interior. To enable time of flight mass spectrometry, a pulsed electron beam and a pulsed extraction grid system (explained in chapter 4) are used.

3.2 Vacuum system

3.2.1 Expansion chamber

In the expansion chamber, an Edwards E09K diffusion pump (2800 l/s) coupled with an Alcatel OME 40S rotary vane pump keeps the pressure to 7.5×10^{-7} mbar when the resistively heated oven is in operation. An electroplated skimmer with a diameter of 1.2 mm mounted on a top hat arrangement is used to separate the expansion chamber from the collision chamber. The conical shape of the skimmer deflects stray molecules and creates a forward collimated beam of biomolecules entering the collision chamber.

A beam of biomolecules is generated using a resistively heated oven mounted inside a bracket in the top hat. The bracket is designed to provide alignment between the capillary of the oven, the aperture in the skimmer and the electron beam. A Thurlby Thander PL330 power supply provides a 0.9 A current to the heating line in the oven. The temperature of the oven is set using an Omron E5CK controller that maintains a preset temperature by switching the current through the heating wire on and off. The temperature is measured using a thermocouple that is placed in a small hole in the copper cavity. The uracil contained in the oven evaporates and exits through a capillary in the front the oven. A constant stream of uracil is generated at 180 ^{o}C.
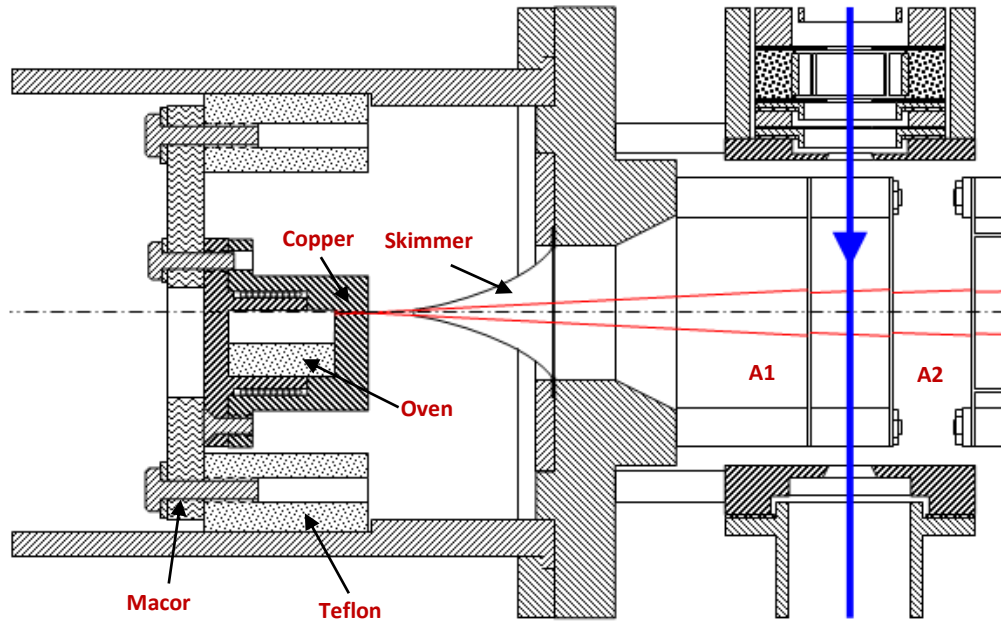
Figure 3.3. Schematic of the oven and skimmer for the effusive source. Mounting of the oven, skimmer and electron gun on the top hat extending into the collision chamber. Collision chamber and expansion chamber are separated by the skimmer.

Two sources were tested during this research. The supersonic source design was introduced to highlight certain advances from the effusive source configuration that are discussed in section 3.3.2. Shown in figure 3.3 and figure 3.4 are the schematics of the oven, the skimmer and their mounting for the effusive and supersonic source set up.

3.2.2 Collision Chamber

A Leybold Turbovac 361 turbo molecular pump coupled with a Trivac D25B rotary vane pump keeps the pressure in the collision chamber to 1.7×10^{-8} mbar. The chamber houses the electron gun (described in section 3.4) used to ionize the

molecular beam, the extraction grids A1 and A2 (shown in figure 3.3 and described in section 3.5), and the Faraday cup (described in section 3.4.2) to monitor the electron currents. These elements are mounted on a top hat arrangement shown in figure 3.2. The chamber also contains a neutral metastable detector which is mounted on a chamber flange at 90 degrees to the direction of the electron beam, but the detector was not used in the research presented here. The molecular beam travels from the expansion chamber into the collision chamber through the skimmer. Ionization and fragmentation of the molecular beam occurs when it interacts with the electron beam in the interaction region. This region is situated between two metal plates A1 and A2 (shown in figure 3.3).

3.3 Molecular beam source

3.3.1 Effusive source

A beam of biomolecules is generated using a resistively heated oven. The oven is positioned in the center of the expansion chamber shown in figure 3.2. The oven is safely mounted on a macor plate which is attached to a hollow teflon cylinder designed to fit into the metal bracket. The uracil evaporates and exits the copper cavity through a capillary located in the front of the oven. The capillary of the oven is aligned to the entrance of the skimmer. The skimmer creates a forward collimated beam of uracil that enters collision chamber. The skimmer has an orifice diameter of 1.2 mm and a base width of diameter 22.9 mm and is mounted on a top hat arrangement shown in figure 3.2. The skimmer allows differential pumping of for the expansion and collision chamber, and allows for a steady flow of the uracil to enter the collision chamber. By varying the distance of the oven capilary and the skimmer, molecular beam flux and collimation can be varied. All measurements in chapter 6 were taken with the effusive source.
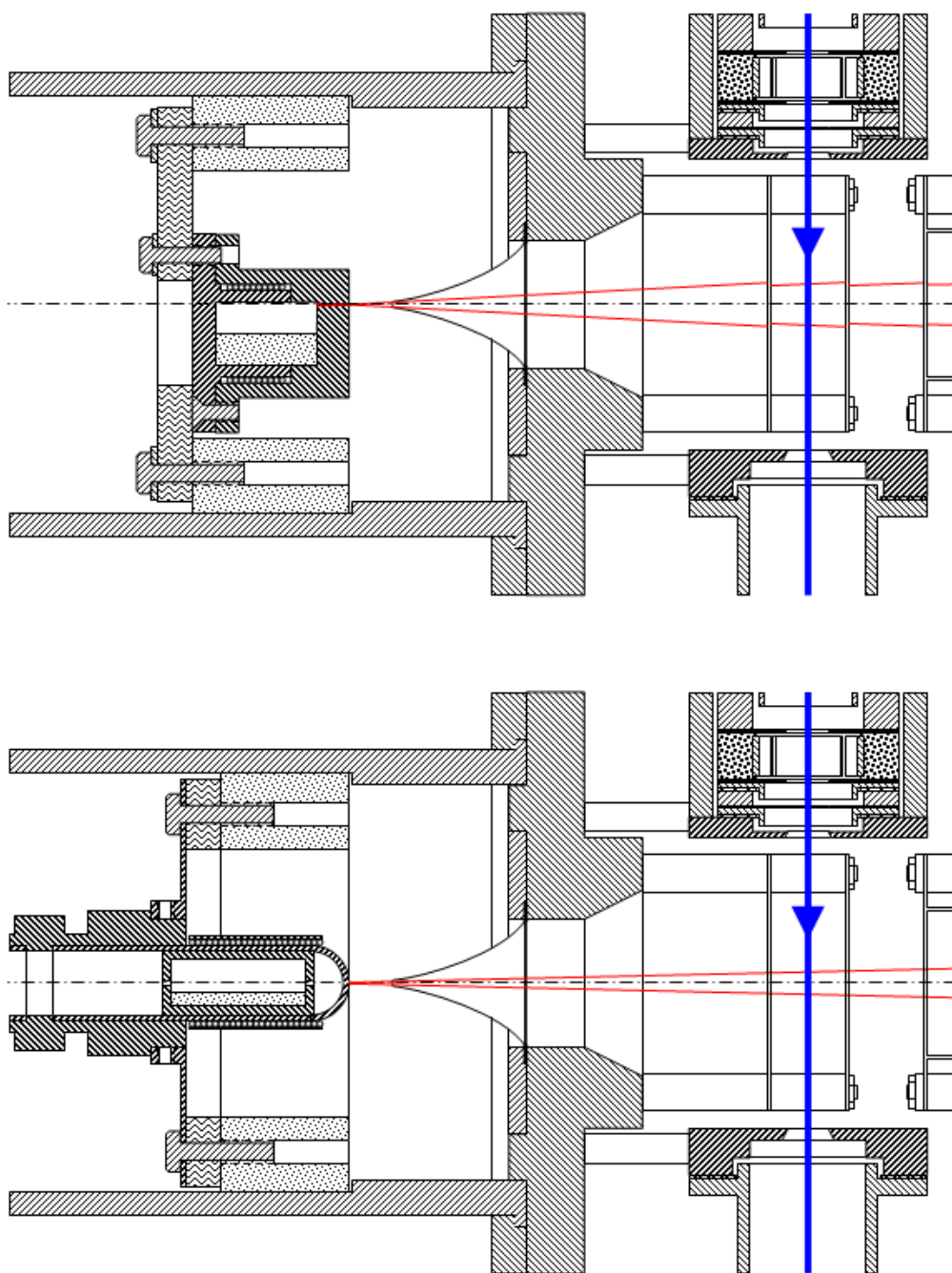
Figure 3.4. The effusive source (top) and the supersonic source (bottom) used to generate beams of uracil. In both figures, the red line indicates the uracil beam, and the blue line indicates the electron beam. The intersection of both beams is midway between the extraction plates A1 and A2. In both figures the electron gun, the Faraday cup and the first element of the Einzel lens are partly shown. The supersonic source connected to the tube and the regulated buffer gas system by a Swagelock connector shown in the bottom figure is also shown in figure 3.5.

3.3.2 Supersonic source

A supersonic source with a 50 micron straight nozzle with argon gas acting as the buffer gas has been implemented and this report presents a few test measurements done with this source (see chapter 7). Figure 3.5 shows the new source mounted on the tube which supplies the argon buffer gas. The supersonic source will improve beam collimation and will enable formation of small nucleobase-water clusters when water vapour is introduced into the source.

A beam of biomolecules is generated using a resistively heated oven mounted at the end of the supersonic source. The supersonic source allows the biomolecules to be easily refilled without the need to let the collision chamber and flight tube up to atmospheric pressure. It is important to note that the pressure in the expansion chamber goes into the 10^{-4} mbar range so the pressure gauges need to be overridden on the interlock box in order to prevent a shut down.

The supersonic source provides alignment between the nozzle of the oven, the aperture in the skimmer and the electron beam. The uracil contained in the oven evaporates and exits through the nozzle when the buffer gas passes through the oven.

The new oven uses a nozzle from Lenox Laser which is a 2" x 0.5" stainless steel tube with a rounded end with a 50 micron nozzle at the centre. This is connected to a 1.5 m x 1/2" stainless steel tube using a SS-810-6 Swagelock fitting (partly shown in figure 3.4). The 1/2" tube passes through the 10" end flange of the expansion chamber and connects to the buffer gas manifold shown in figure 3.5. Regulated argon gas from the foreline interacts with the evaporated uracil in the oven to produce a molecular beam and is fed from the inlet valve to the nozzle. The valve is mounted in a Teflon holder that slides into the bracket in the top hat.
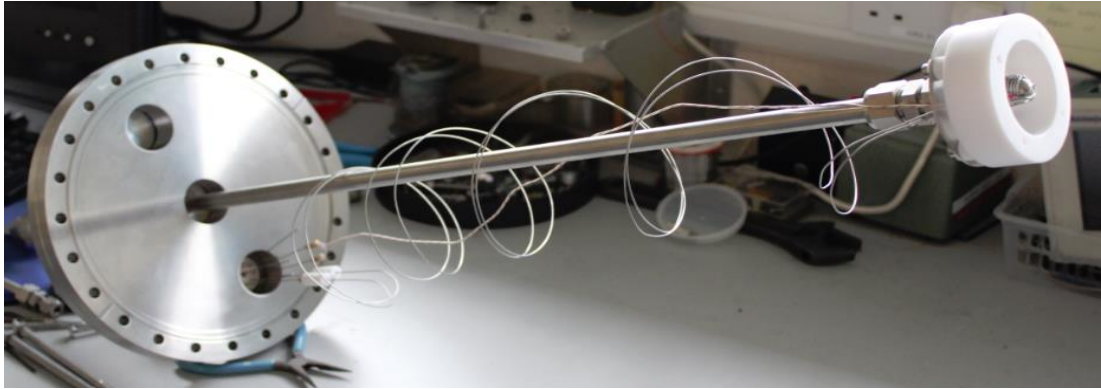
Figure 3.5. The supersonic source
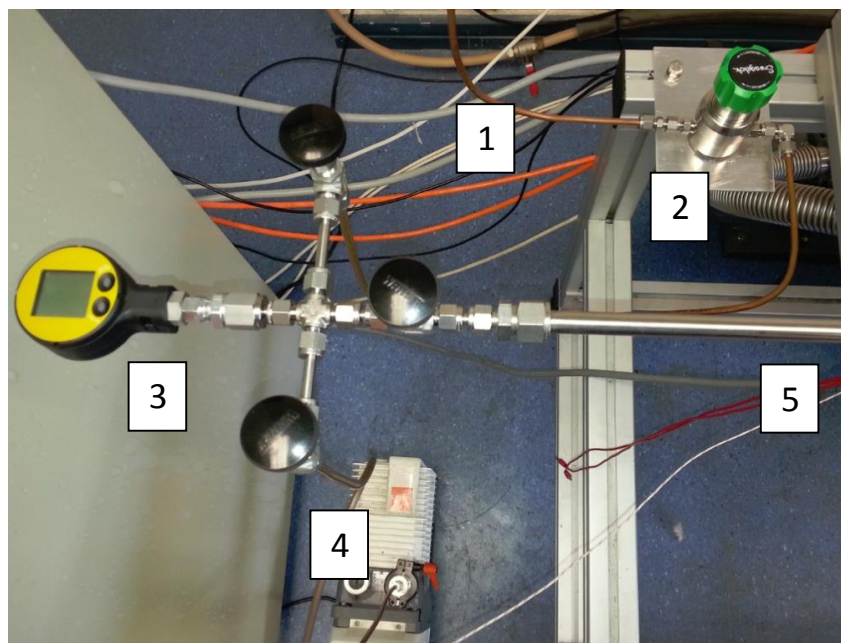
3.3.3 Buffer gas system

Figure 3.6. The regulated buffer gas system. 1 – Boc gas regulator (1-2 bar), 2 - Swagelok KPR regulator (0.1 – 0.5 bar), 3 - Keller LEO 2 digital manometer, 4 - Alcatel 2010 SD rotary vane pump, 5 - Regulated buffer gas to source.

An argon gas research grade bottle housed in a safety compartment delivered a stable flow of 1 bar of argon gas into the foreline using a BOC gas regulator on the bottle. By regulating the flow of argon gas by the Swagelok S series metering valve it was possible to achieve a stable flow of gas from the foreline into the source. The Swagelok valve regulated the flow of argon gas in the source to about 0.1 bar. A Keller LEO 2 digital manometer measured the pressure in the source. This manometer is a highly accurate pressure measuring device that uses a piezoresistive pressure transducer to read out the real time source pressure. An Alcatel 2010 SD rotary vane pump was used to decrease the pressure in the foreline. During the measurements the pressure in the source was poorly regulated and fluctuated between 0.02 and 0.18 bar related to small variations in the ambient temperature in the labaratory. A new regulator will be used in the future to try to stabalise the source pressure.
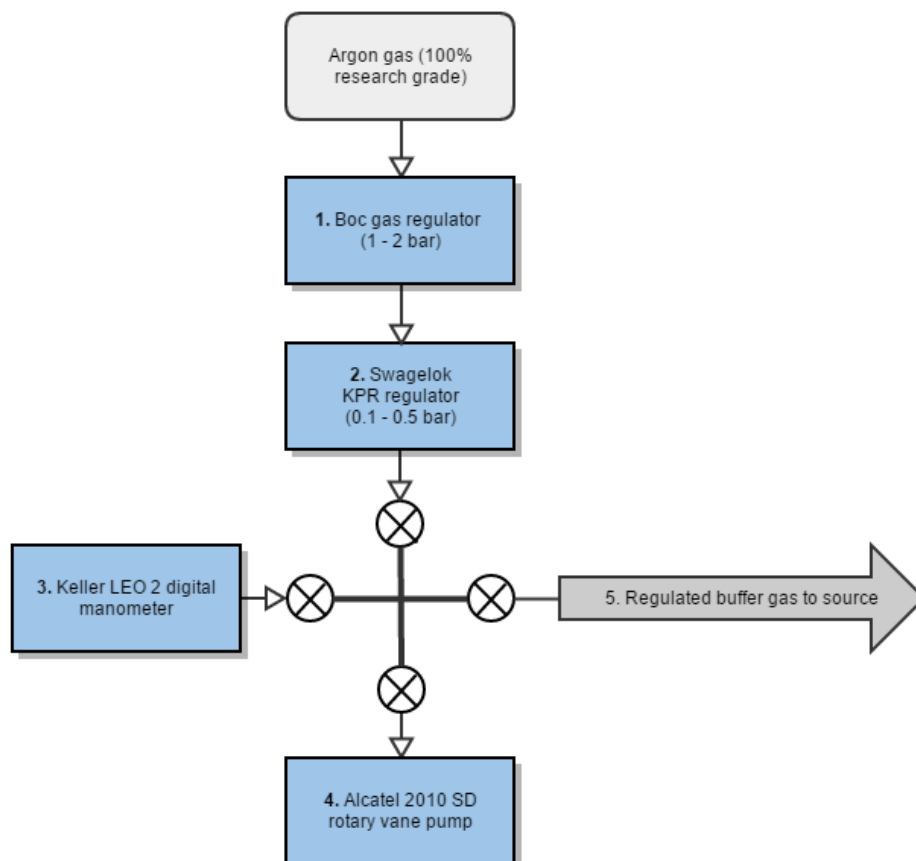

Figure 3.7. Flow chart diagram of regulated buffer gas system.

3.4 The electron gun

The electron gun used in this experiment produces a pulsed beam of low energy electrons. It consists of a filament holder ("grid") with a 1.5 mm aperature, a deflection system for steering the beam and four lens elements to focus the beam (for more details see [40]). The grid potential is set slightly negative with respect to the filament tip and V1 is set to 46 V in order to achieve this. The filament tip of the electron gun is centered in the hole of the grid element. The electron gun is positioned on a top hat arrangement in the collision chamber 90 degrees to the molecular beam as shown in figure 3.4 and figure 3.8. A current of 2 A is supplied to a tungsten filament that releases electrons by thermionic emission. The beam passes through the interaction region (area where electron beam and molecular beam interact) which is located between the two grids A1 and A2. To focus the electron beam the voltages on four lens elements (V1, V2, V3 and V6 shown in figure 3.9) were individually varied. To allow steering of the electron beam, four deflection plates X1, X2, Y1 and Y2 were mounted in lens element V3. The electron impact energy is controlled externally by a Kepco APH 500M DC programmable power supply controlled using a LabVIEW program discussed in chapter 4. It is shown as V $_{incident}$ in figure 3.10.
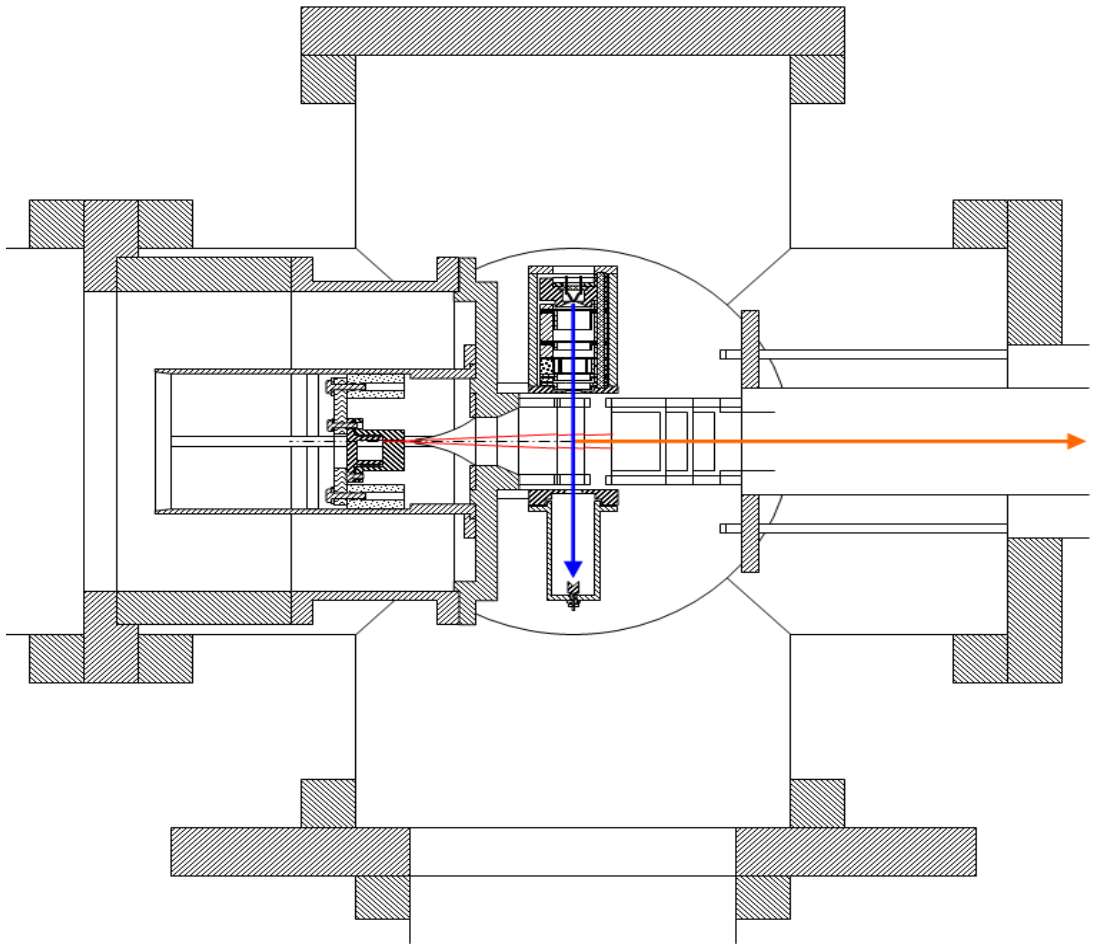
Figure 3.8. Diagram of the collision chamber, containing the top hat assembly with the oven, bracket, skimmer and electron gun. The Einzel lens and part of the field free region of the reflectron TOF mass spectrometer are also shown. The blue line represents the beam of low energy electrons, the orange line represents the molecular beam.
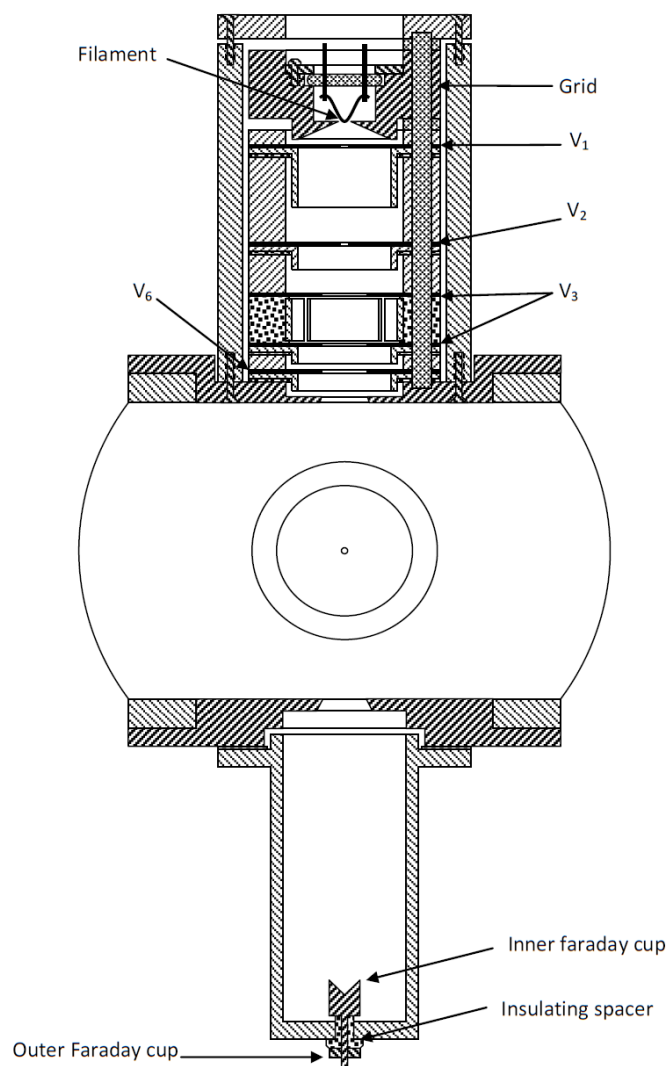
Figure 3.9. Schematic of the electron gun and Faraday cup. The molecular beam is directed out of the paper

3.4.1 Electron gun voltage supply

An array of potential dividers inside the electron gun voltage box is used to apply the desired voltages to the electron gun elements that are controlled by a set of potentiometers mounted on the front panel of the electron gun voltage box. Test points exist on the front of the voltage box so the potential of each electrode can be measured while in operation. The voltage box is powered by a Kepco APH 500M DC power supply. This power supply delivers 300 V with a current of 40 mA to the circuit. For the deflection system in the electron gun, the power required is +/ -24 V

DC. This is provided by two EPSD 15/200C AC-DC converters from VxI Power Limited. The two convertors provide + 24 and -24 V and require 230 V AC input voltage. This provides the variance for the deflection voltages across each pair of deflection plates.
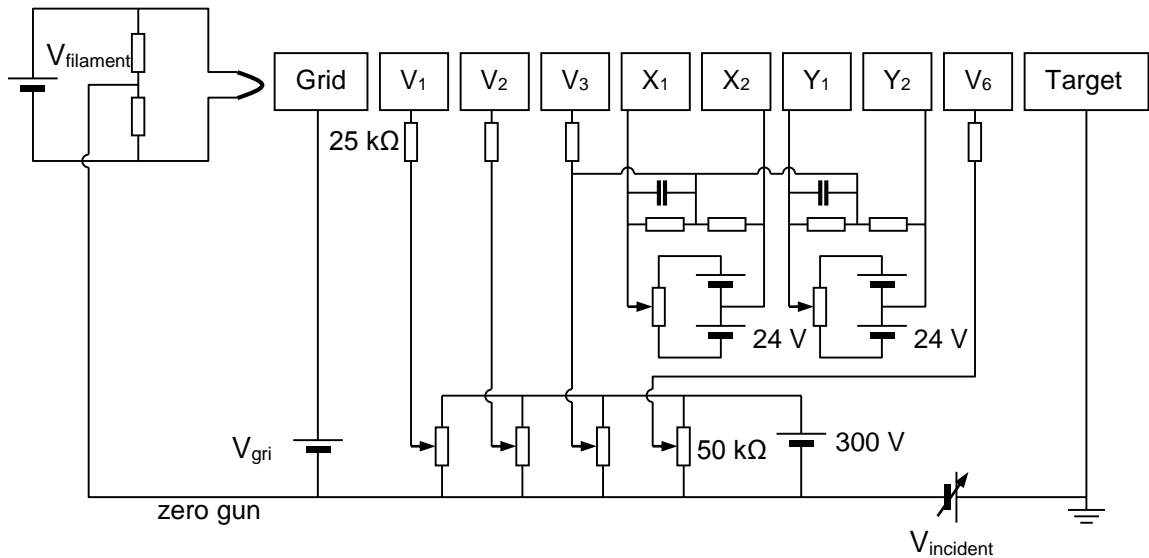

Figure 3.10. Circuit diagram for the voltages of the electron gun.

3.4.2 The Faraday cup

The electron beam is collected in a Faraday cup which consists of an inner cup which is held at +40 V and an outer cup which is held at +10 V. Both cups are separated by an insulating space. The Faraday cup is used to measure the beam current as a function of incident energy. The current from each cup is measured using a Keithley 610 C ammeter. A LabVIEW program is used to record the current of the outer Faraday cup and inner Faraday cup from the ammeters. The outer Faraday cup current was minimised and the inner Faraday cup was maximised in order to optimise the beam and to achieve greatest collimation.

3.5 Flight tube and reflectron time of flight mass spectrometer

Two Leybold Turbovac 361 turbo molecular pumps coupled with a Trivac D25B rotary vane pump keep the pressure in the collision chamber and flight tube at 1.7×10^{-8} mbar. The reflectron used was manufactured by R.M. Jordan Company in California. Ions produced at the interaction region are repelled into the flight tube by the grid potential of A1 (pulsed to +100 V). Its purpose is to accelerate the ions into the einzel lens arrangement for focussing of the ion beam. The einzel lens arrangement consists of three electrodes. The first and third electrodes are held at a potential of -1200 V, which is also the potential of the flight tube and the second (V_{focus}) is set to a potential of -1400V. The ions must be deflected slightly before traversing the flight tube in order to reach the center of the MCP detector because it is not centrally located. To achieve this, two deflection plates XY1 and XY2 are used to steer the beam. XY1 is set to -1200 V and XY2 is set to -1140 V with respect to ground. These values were previously determined by J. Lynch [42].

The ions pass through the flight tube and enter the reflector. The field created in the reflector is at the end of the flight tube. The polarity of the field is the same as the ions so they experience a retarding potential that acts as an ion mirror by deflecting the ions and sending them back through the flight tube until the ions reach a microchannel plate detector (MCP). The voltages used in the reflector are VR1 = -390 V and VR2 = +87 V. A resistor divider network spreads the strength of the electric field in the reflector uniformly across 18 plates and grid apertures.

The micro channel plate detector is positioned opposite to the reflector to capture the arrival of ions after they are reflected. The voltage of the detector is set to -3800 V, which is divided across two plates by a voltage divider network resulting in VD1= -1672 V, VD2 = -912 V and VD3= -180 V, where VD1 is applied to the front of the first plate, VD2 is applied to the back of the first plate and also to the front of the second plate, and VD3 to the back of the second plate (this design stops the voltage exceeding 1000 V across any one plate). These values were previously

determined in a test by Gerard Barret [43]. The electronics used for accumulation of the pulses from the microchannel plate detector is described in the next chapter.
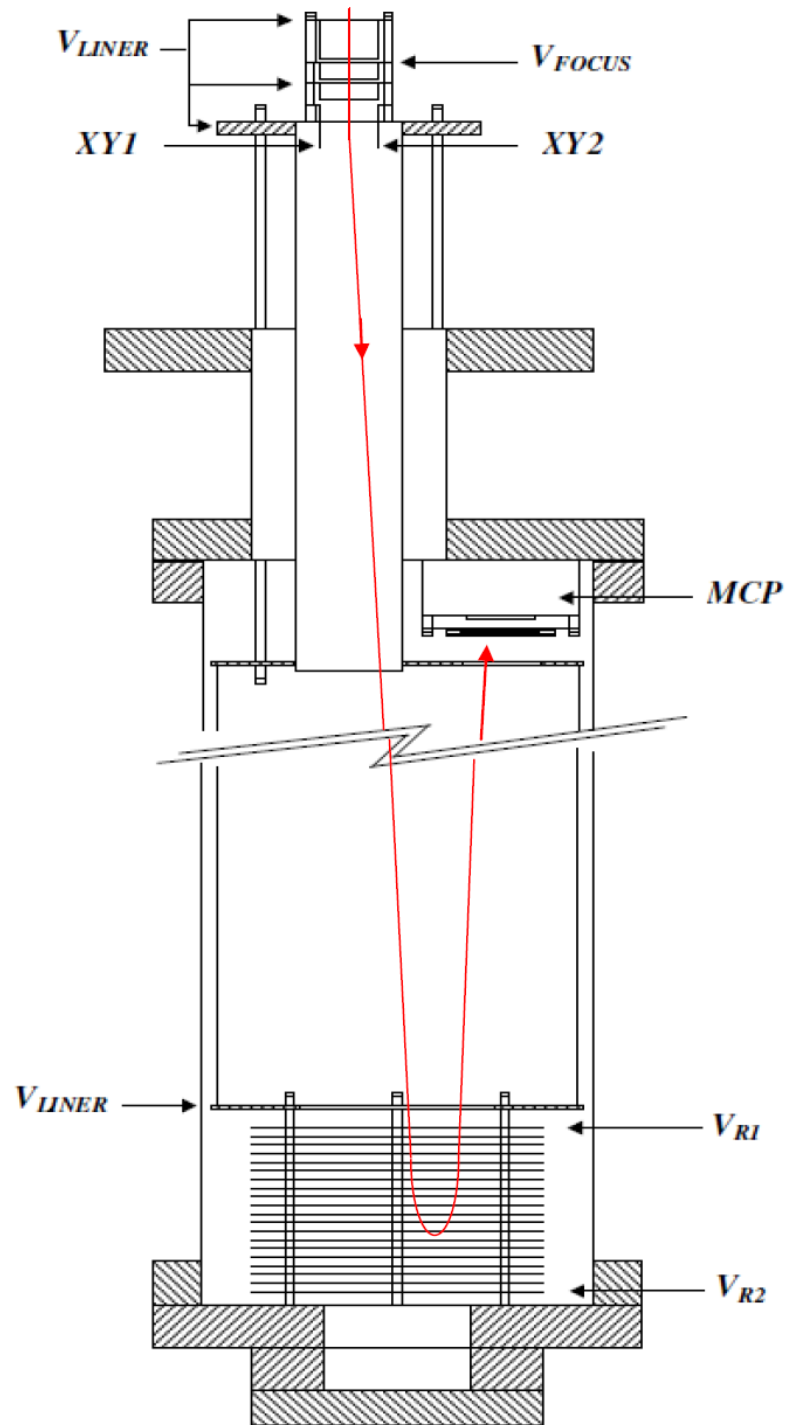

Figure 3.11. Schematic of the reflectron and MCP detector used in this project.

Chapter 4: Data acquisition and analysis

4.1 Introduction

The steps to acquire mass spectra as a function of electron impact energy are described in this chapter. To acquire a mass spectrum a combination of hardware, software and analysis of data is required. The hardware includes a digital delay generator (described in section 4.2.1), an amplifier and timing discriminator (described in section 4.2.2) and a multichannel scaler (described in section 4.2.3). The hardware and software work together to set a sequence of events. The pulsing and timing sequence of the various elements of the system are set *via* a digital delay generator. The experiment is LabVIEW controlled and programs run in LabVIEW for hardware control and data acquisition are described in section 4.5. The initial event involves the pulsing of the electron gun, the following step triggers the pulsing of the extraction grid voltage immediately after the pulsing of the electron gun to extract ions out of the interaction region and into the flight tube. The final step involves the triggering of the multichannel scaler (MCS) after the ions are extracted.

4.2 Data acquisition hardware

4.2.1 Pulsing

The electron gun pulse, ion extraction pulse and the multichannel scaler trigger pulse all require the correct width and delay with respect to each other in order to record accurate data. The delays are produced by a DG535 digital delay generator designed by Stanford Research Systems Inc. The digital delay generator features a T0 pulse to mark the beginning of the timing cycle, four delay outputs A, B, C and D, and two independent outputs AB and CD. The delay outputs can be set over a range

of 1000 s with a 5 ps resolution. Each timing cycle is started either by the internal clock or by an external trigger. In this experiment the internal clock was used. The first delay of the independent output specifies the leading edge of the pulse, while the second delay defines the trailing edge. The pulse shapes can be TTL or NIM and normal or inverted (respectively). The four delay outputs A, B, C and D are triggered relative to T0 after their programmed delays. The A, B, C and D outputs return low about 800 ns after the longest delay. The pulse outputs AB and CD go high for the time interval between their corresponding delay channels [42].
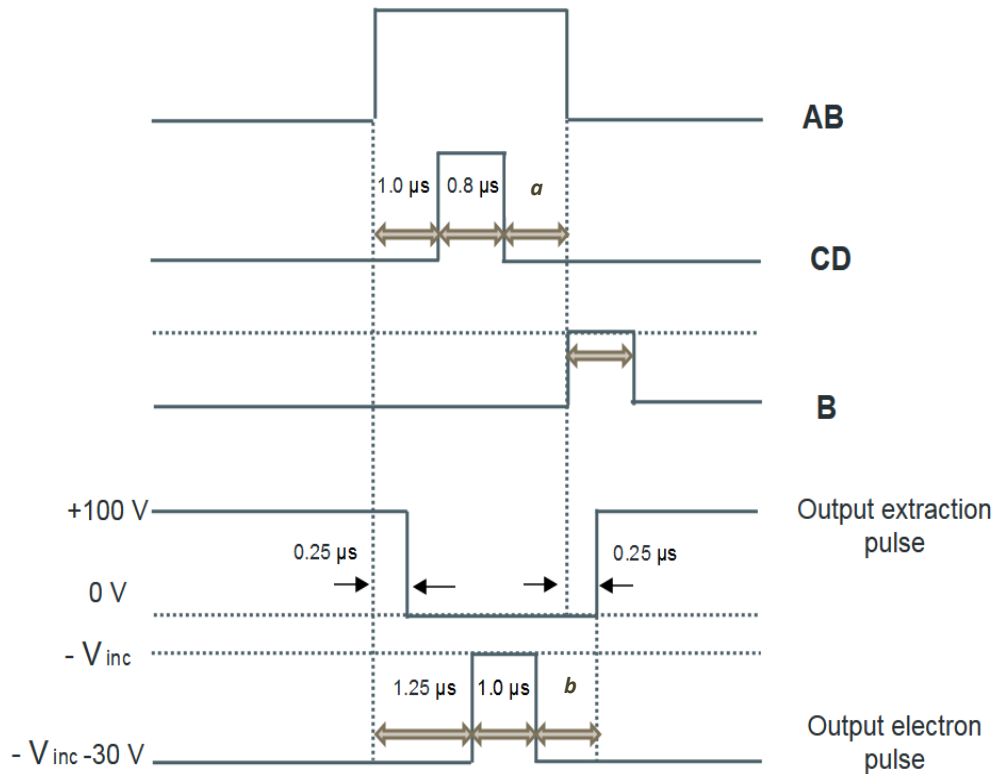

Figure 4.1. Pulse settings used for the electron gun and the ion extraction. For the effusive source the settings were: a=1.0 μs, b= 0.80 μs**.** For the supersonic source the settings were: a=0.27 μs, b=0.05 μs

When the pulse of the electron gun passes through the interaction region, the extraction voltage on A1 grid (+100V) must be dropped to ground. The potential of the A1 grid is on for the majority of the cycle in order to remove all ions in the interaction region before the electron gun is triggered. This reduces any background in our mass spectra. This is initiated by a signal sent from the AB output (TTL) to an ion extraction remote pulser box connected to A1. The ion extraction remote pulser box requires 12 V to power its circuit, two dc voltages to specify the low and high voltages (see figure 4.1) of the output pulse and a TTL trigger pulse to determine the timing of the output pulse. The remote pulser connects to the A1 grid by a vacuum feed through.

Immediately after the extraction plate has dropped to ground the electron gun is pulsed. The CD pulse (shown in figure 4.1) is used to trigger the remote pulser for the electron gun which pulses from $-V_{inc} -30$ V to $-V_{inc}$. The electron gun remote pulser box consists of a bias voltage set by a Farnell L30B (stabilised) power supply, a pulse voltage from a Farnell E30/2 power supply, a 12 V input to power the circuit from the pulser power supply and an input for the CD pulse. To reduce the kinetic energy spread among ions with the same m/q ratio leaving the source a delay exists between the ion formation and extraction pulse as shown in figure 4.1.

The ions are repelled into the TOF region when A1 is restored. Output B of the digital delay generator is delayed by 1 μs (using an ORTEC 416A gate and delay generator) and connected to the START IN input of the MCS card and this triggers a sweep of the MCS card. When the ions hit the MCP detector pulses are produced and are amplified. The signal is then sent to the STOP IN of the MSC card to trigger the stop of the cycle. The pulse settings used for the remote pulsers are shown in figure 4.1. For the uracil measurements in this report the repetition rate used was 8 kHz (125 μs between successive pulses) and the time-of-flight range was 62 μs.
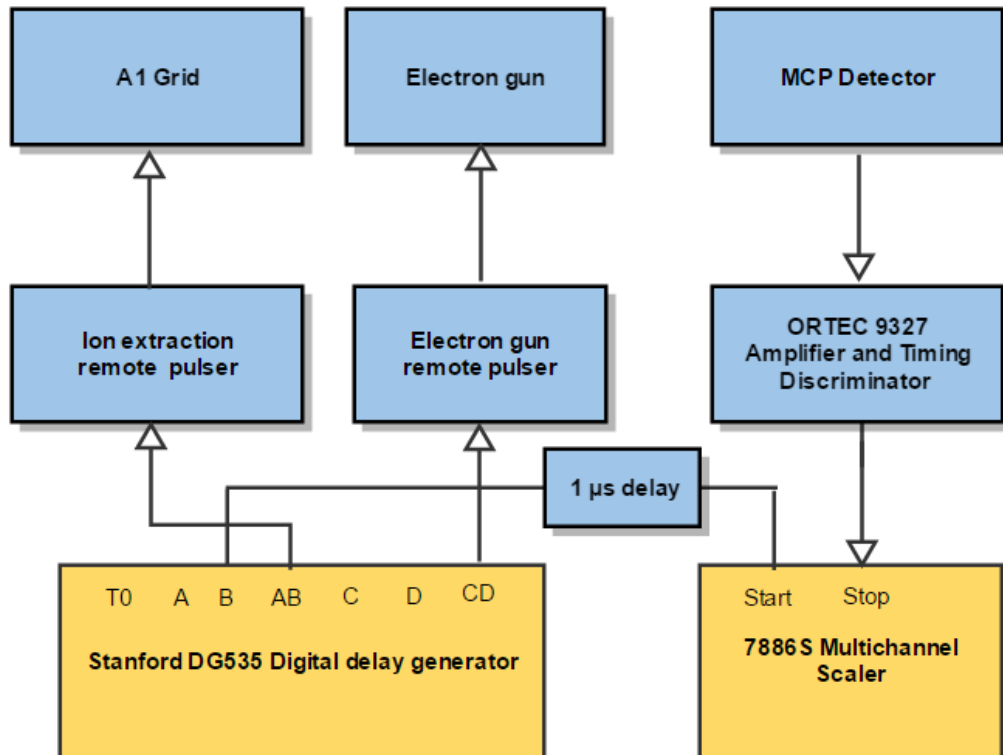
Figure 4.2. Pulsing setup for DG535 digital delay generator.

4.2.2 Amplifier and timing discriminator

The signal produced by the microchannel plate detector (MCP) when an ion is detected must be amplified and discriminated before any data acquisition can take place. The ORTEC 9327 1GHz amplifier and timing discriminator has a 1 GHz bandwidth to minimise the noise and rise time contributions to timing jitter on detector pulses. The amplifier and timing discriminator amplifies pulses in the range with widths of 0.25 – 5 μs and amplitudes up to – 150 mV. The device features an LED to indicate when pulse amplitudes have exceeded the discriminator level of the amplifier. The discriminator level was set at -19 mV by monitoring the background signal between the peaks from single mass spectra.

4.2.3 Multichannel scaler

The Multichannel scaler card used in this experiment was the 7886S by FAST
ComTec. It is used to accumulate time of flight spectra. The 7886S multichannel
scaler card can accept one event in every channel with up to 2 GHz of peak count
rates. It has a dynamic range of up to 2^{37} channels, which enables sweeps for 68.7
seconds with a time resolution of 430 ps per channel [45]. The card is controlled by
a set of instructions written in LabVIEW. The code in the LabVIEW program contains
two different nodes. The first node initialises the MCS card and the second node
deals with the measurements of the data (bin width and time range). The bin width
ranges from powers of 2 up to 16,384 channels each. The dwell time of each
channel is 430 ps. The range is the length of the spectrum in bins. The mass spectra
recorded had a bin width of 128 channels and a range of 1122 bins (61.8μs).

The inputs and outputs contained on the card are. STOP IN, START IN, ABORT IN,
SYNC OUT, DIGITAL IN and a THRESHOLD ADJUST potentiometer. Output B of the
digital delay generator is connected to the START IN input of the MCS card shown in
figure 4.2. The multichannel plate detector output is connected to the input of the
amplifier and timing discriminator and the NIM OUT output of the ORTEC 9327 is
connected to the STOP IN of the MCS card shown in figure 4.2 so that the signal
from the detector can be registered as a count at the designated binning location of
the MCS.

4.2.4 Calibration of the multichannel scaler

The MCS card utilizes a phase-locked loop (PLL) oscillator that is set to at least 1.8
GHz which results in an assured time resolution of less than 500 ps per channel. This
frequency can vary so the time per channel was calibrated using the DG535 digital
delay generator as an external reference. The multichannel scaler card was
calibrated in order to determine the time length of one channel. The digital delay

generator was used to send a start and a stop pulse with a fixed delay to the MSC card. The accuracy of the calibration is limited by the accuracy of the delay generator which is 5 ps. The delay in the pulses was varied over 55 µs in steps of 5 µs and the corresponding channel number was recorded.
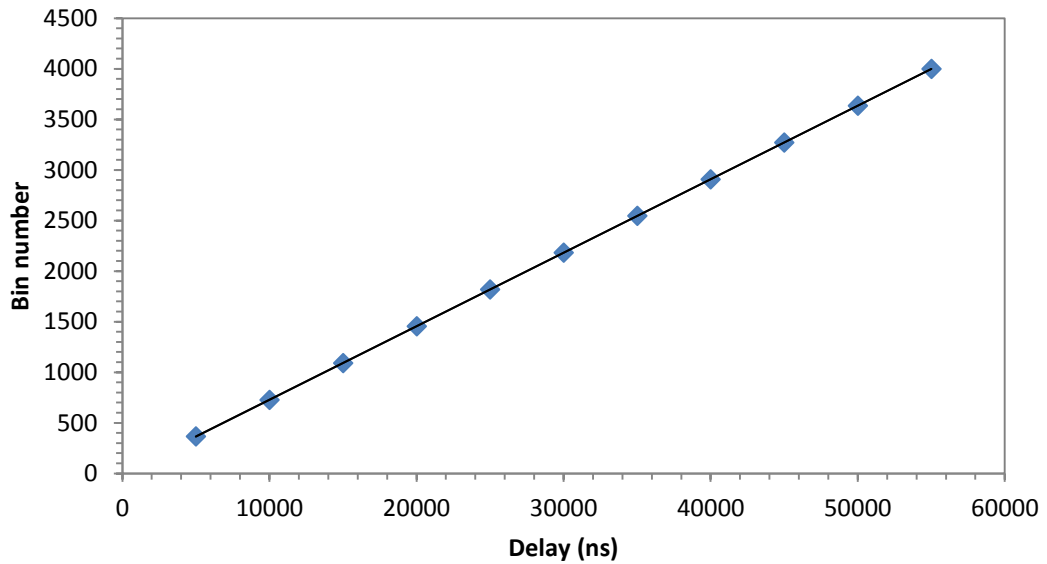

Figure 4.3. Calibration measurement of the multi channel scaler card.

The best fit line was drawn through these points and the slope was found to be 72.666 ± 0.005 bins per µs, yielding a dwell time of 430.05 ± 0.03 ps per channel. A bin width of 32 channels was used. For the measurements on Uracil a bin width of 128 channels was used, corresponding to 55.046 ± 0.004 ns per bin.

4.3 Data acquisition software

4.3.1 LabVIEW Programs

The data acquisition programs are designed in the graphical programming language LabVIEW by National instruments. LabVIEW is capable of controlling external hardware and data analysis. Two different LabVIEW data acquistion programs were used to measure mass spectra for this experiment. A program for the acquisition of single scans of mass spectra is described in section 4.2.2 and a program for the acquisition of mass spectra as a function of electron impact energy is described in section 4.2.3. The LabVIEW programs used for data analysis are explained in detail in section 4.4.

A LabVIEW program called set-gun-V-myDAQ.vi is used to set the electron impact energy of the electron gun. A National Instruments myDAQ data acquisition device is connected to a KEPCO APH 500m programmable power supply *via* terminals located on the back. It is capable of producing voltage levels up to 500 V DC. The myDAQ has two analog input channels that act as a high impedance differential voltage input and has two analog output channels. Both channels have digital to analog converters (DAC) and are capable of updating simultaneously.

4.3.2 Single mass spectra

Two different LabVIEW programs were used to measure mass spectra for this experiment. For the acquisition of a single mass spectrum a program called getspectrum-3-5.vi was used. The program records data from the MCS card and allows real-time observation of data while it is being acquired and displayed on a graph. The card for this project is controlled externally in LabVIEW. The card settings and functions are stored in a dynamic link library (DLL) which contain C

code written for communication with the MCS card. The DLL files are accessed in LabVIEW using a built in Call Library Function node VI. The DLL files were provided by Dr. Marcin Gradziel and are a modified version of the code provided by FAST ComTec. The code in the DLL contains two different nodes. The first node initialises the MCS card and the second node deals with the measurement of the data (bin width and time range). The program was developed by Dr. Peter van der Burgt with help from Dr. Marcin Gradziel. The program was coded using a standard state machine. The program replaced the MCDWIN software provided by FAST ComTec (to allow the implementation of a multi scan program, see next paragraph). The front panel of the program, shown in figure 4.4 displays a mass spectrum of argon.
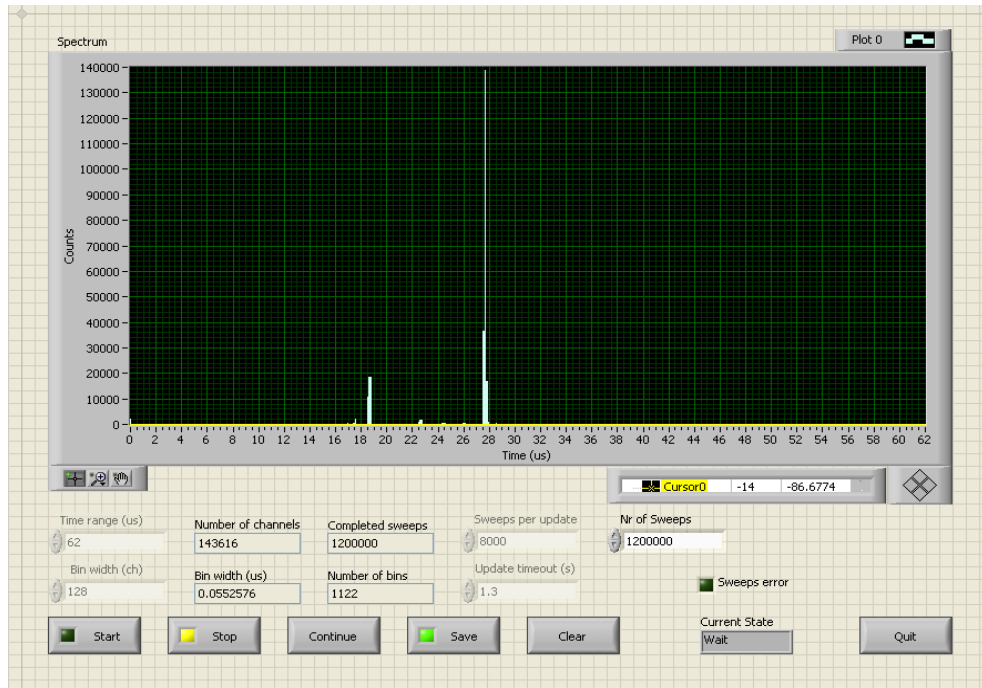

Figure 4.4. Front panel screen shot of getspectrum-3-5.vi, showing a mass spectrum of argon

4.3.3 Mass spectra as a function of electron energy

The second program called Spectra-vs-E-v7.vi measures and records multiple mass spectra. Mass spectra are recorded sequentially, with the electron impact energy incremented by a set step size value, over a range of electron impact energies.The program was developed by Gerard Barrett [43] with help from Dr. Marcin Gradziel and modified by Dr. Peter van der Burgt. The program uses a structure of three nested loops.

The first loop runs for the amount of cycles set. Within one cycle of this loop a complete set of runs across the range of electron impact energies is taken. Multiple cycles are taken so that we have a number of such sets, each of which can independently be used to extract an ionisation yield curve, yet allow us to examine any time dependent effects in the spectra. Twelve cycles were measured for this experiment.

The second loop runs the acquisition carried out by the MCS over a range of impact energies, stepping through those energies sequentially. The initial electron impact energy was set to 0 eV and was incremented by step size value of 0.5 eV over a range of 200 electron impact energies. A time delay was implemented between successive electron impact energies to allow the electron gun to stabilise.

The third loop sets the number of sweeps per scan. Each mass spectrum completes 240,000 sweeps using an electron pulse rate of 8 kHz, acquisition of a single mass spectrum takes about 30 seconds, and a full cycle is completed in slightly less than 2 hours. The front panel gives the user control of the number of cycles (Cycle), the starting and stopping impact energies, time range, the number of sweeps per scan (sweeps completed), the bin width and the step size (E nr). The program records data from the MCS and allows real time observation of data while it is being acquired. A full 2 dimensional array of mass spectra as a function of electron energy

is written after the completion of each cycle. The uracil data set in chapter 6 contained 12 cycles.

4.4 Data analysis software

4.4.1 Gaussian Peak Fitting

For calculating ion yields for each fragment in our mass spectra, a program called multigauss test.vi was used. The peak area for each fragment is needed for the accumulation of ion yield curves. Individual peak areas can be accurately determined for adjacent peaks that overlap each other in the mass spectrum. In this program the Levenberg-Marquardt vi is used to fit a series of adjacent mass peaks with a sequence of Guassian functions. The Levenberg-Marquardt algorithm determines the set of parameters that best fit the input data points (x) as expressed by a nonlinear function $y = f(x)$. A model function is required as an input for the Levenberg-Marquardt algorithm. All the peaks were fitted using a sequence of normalised Gaussian functions given by:

$$f(x) = \sum_{i=1}^{n} \frac{c_i}{a\sqrt{\pi}} \exp\left(-\left(\frac{x-p-\Delta_i}{a}\right)^2\right) + d \qquad (4.1)$$

where c_i is the peak area, p is the position of the largest peak in the group, a is the peak width (assumed equal for the adjacent peaks), Δ_i is the difference between the peak position and that of the largest peak in the group, and d is the background. The input variable x is the bin number.

For each group of peaks the relevant part of the output file of Spectra-vs-E-v7.vi is extracted, and used as the input for the Guassian peak fitting. This data comprises a two dimensional array of ion yields as a function of bin number and of electron energy.

The user selects the number of fits to be performed. We used 200 fits because we used an energy range of 0-100 eV in steps of 0.5 eV. Within one cycle of the loop a complete fit on a group of peaks at a single electron impact energy is performed and an array containing the best fit parameters are saved. A time delay was introduced into the code in order to inspect the fitting process for errors. For near threshold fits, problems with convergence were encountered, and for this reason the fits were separated over a smaller energy range near threshold with a reduced number of peaks (if possible) and with the width a and/or the position p of the largest peak set fixed. The width a would be fixed to the average value obtained at higher electron energies. Sometimes two different widths a and b were used to fit a group of peaks. In all cases the background d was set to a fixed value (1 in most cases) to avoid unrealistic fit results.
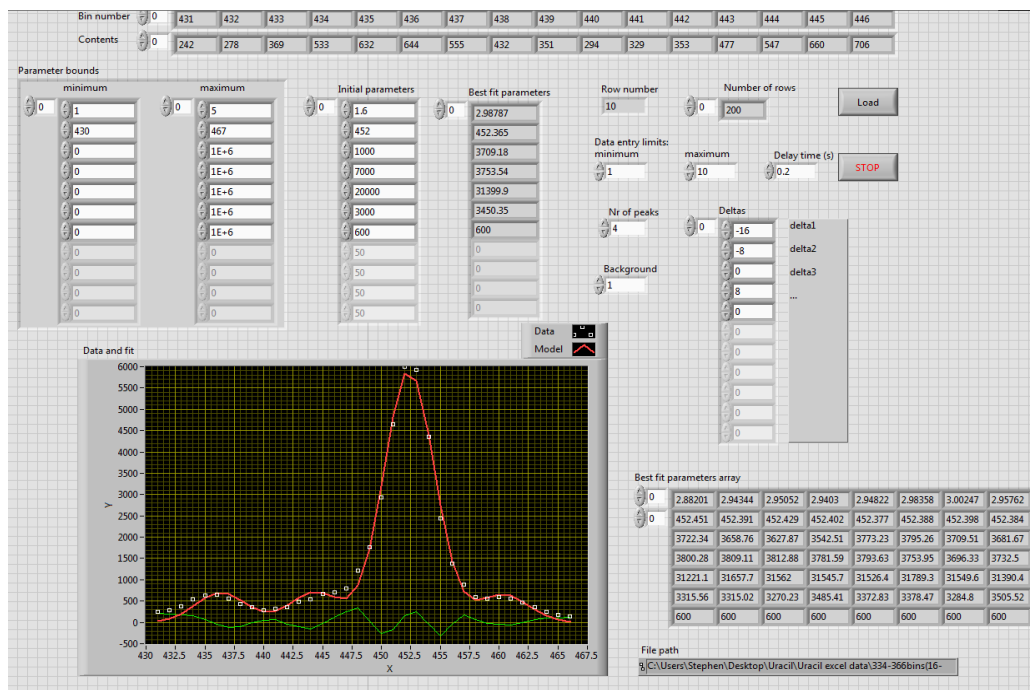
Figure 4.5. Front panel screen shot of multigauss test.vi (26 – 29 u group)

The initial parameters array shown in figure 4.5 is where the user must input the estimates for the area of each peak, the position of the peak with the highest mass and the peak width. The user must also input the number of peaks in the fit and deltas (bin number difference between peaks). The size of the array will change depending on the number of peaks to be fit. The best fit parameters array stores the best fit values obtained at each energy. Ion yield curves are obtained for each group of peaks in succession for all electron impact energies. The ion yield curves display the fragmentation sequence as a function of incident energy for each fragment.

4.4.2 Determining appearance energies

To determine the appearance energy of a fragment a LabVIEW program called single_onset.vi was used. The program was developed by Peter van der Burgt with help from Sinead Finnegan [46]. The ion yields near threshold are extracted from

63

the ion yield curves for each fragment. A non-linear model onset function fit convoluted with a Guassian function was used to determine the appearance energy of an individual fragment. The measured curve was fitted using the function $P(E)$.

For a single onset (appearance energy) the following function was used :

$$P(E) = \int_{-\infty}^{\infty} f(\varepsilon)\, g(E - \varepsilon)d\varepsilon + d \qquad\qquad (4.2)$$

$$f(\varepsilon) = 0 \qquad\qquad\qquad \text{if } \varepsilon \leq E_1$$

$$f(\varepsilon) = c(\varepsilon - E_1)^p \qquad\qquad \text{if } \varepsilon > E_1$$

$$\text{With: } g(\varepsilon) = \frac{1}{\sigma\sqrt{\pi}} \exp(\frac{-\varepsilon}{\sigma})^2$$

The function comprises several parameters: a background d, a scaling factor c and a power value p. E_1 and E_2 are the onsets. σ is the Guassian beam width which is fixed at 0.48, corresponding to an electron beam width of 0.8 eV. The convolution integral was evaluated using a nine point Gauss-Hermite quadrature.

For two onsets the function was modified to;

if $\varepsilon > E_2$ $\qquad\qquad f(\varepsilon) = c_1(\varepsilon - E_1)^{P_1} + b + c_2(\varepsilon - E_2)^{P_2} + d \qquad$ (4.3)

The errors in the appearance energies are provided by the Constrained Nonlinear Curve Fit vi in LabVIEW, which uses the Levenberg-Marquardt algorithm. This vi provides the covariance matrix C_{ij} and the residue R, which is the weighted mean square error between the best nonlinear fit and the data. The estimated errors σ_i

in the fit parameters are obtained from the diagonal elements of the covariance matrix by using the formula

$$\sigma_{i=}\sqrt{\mathcal{X}_r{}^2 C_{ii}}$$

in which the reduced chi-squared is given by

$$\mathcal{X}_r{}^2 = \frac{1}{n-p}\,\mathcal{X}^2 = \frac{n}{n-p}\,R$$

where n is the number of data points and p is the number of fitted parameters.

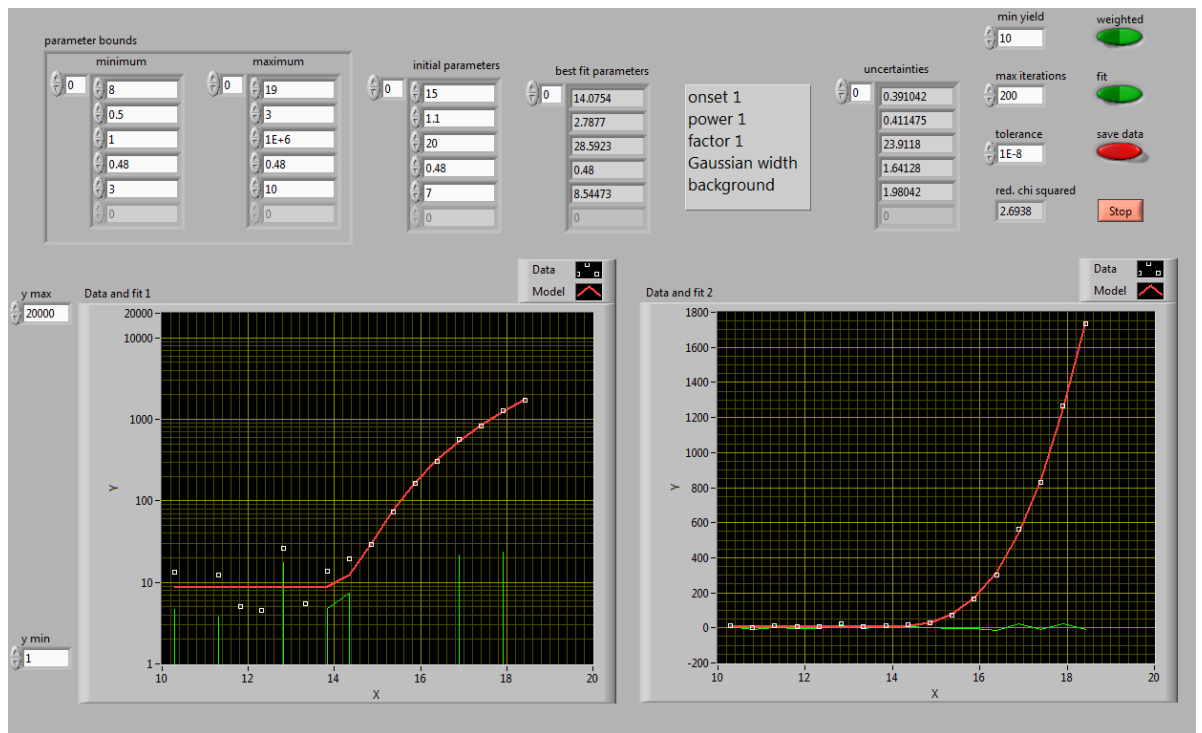The errors do not incorporate the error in the energy calibration. The energy calibration is discussed in chapter 5.

Figure 4.6. Single-onset function fit to determine the appearance energy of the 28 u cation fragment.

The graph on the left in figure 4.6 displays the ion yield count logarithmically plotted as a function of the electron energy and the graph on the right displays the ion yield count linearly plotted as a function of the electron energy.

Chapter 5: Calibration and test measurements

The purpose of this chapter is to present the test measurements conducted to ensure the validity of the experiment. These test measurements included the calibration of the electron gun and the calibration of the mass spectra. 16 u, 17 u and 18 u ions are generated in the interaction region in the collsion chamber as a result of residual water content coming from the walls from the inside of the collision chamber. The water peaks (16 u, 17 u and 18 u) in our mass spectrum are shown in figure 5.2. An analysis of the water peaks taken from our mass spectrum is used for the energy calibration.

5.1 Electron gun calibration

A LabVIEW program called gun-test-my DAQ.vi is used to test the operation of the electron gun. The LabVIEW program is used to control the Kepco power supply that sets the acceleration voltage of the electron gun. The acceleration voltage setting determines the incident electron gun energy. The program also measures the inner Faraday cup current and outer Faraday cup current corresponding to the incident electron gun energy using a myDAQ device connected to two Keithley 610C ammeters. The ammeters measure the currents from the outer Faraday cup and inner Faraday cup as the electron impact energy is incremented in a set step size and the program calculates the total current as a function of electron impact energy.
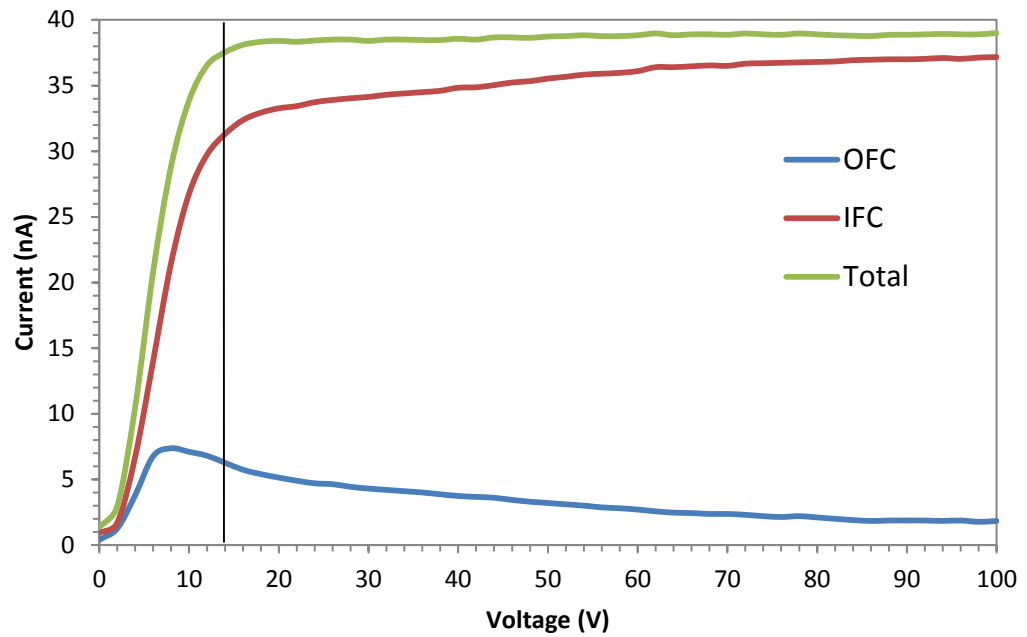
Figure 5.1. Optimum electron gun setting for ongoing pulsed operation (OFC – Outer faraday cup, IFC- Inner Faraday cup)

The electron gun is calibrated to ensure the current remains constant when the electron gun incident energy is changing. The results were achieved by a series of systematic tests by varying the two deflection plate voltages and the voltages of V3 and V6. The optimum electron gun setting is shown in table 5.1. This provided an IFC current of 38 nA and an OFC current of 1.5 nA with an electron pulse width of 1.0 µA and a repetition rate of 8 kHz. The red data series represents the current for the outer faraday cup (OFC). The green data series represents the inner faraday cup (IFC) and the green data series represents the total current. The total current is constant from 100 V down to 17 V, below which the current begins to deteriorate.

Settings	V pulsed
V filament	3.05 V
I filament	2.25 A
V Grid	-0.076 V
V_1	50.1 V
V_2	207.9 V
V_3	58.1 V
V_{x1}/V_{x2}	-5.56/5.56 V
V_{y1}/V_{y2}	-11.6/11.6 V
V_6	10.7 V

Table 5.1. Optimum voltage and current settings for the pulsed electron gun used for uracil measurements in chapter 6.

5.2 Calibration of Mass Spectra

In order to calibrate the mass spectrum the time of flight scale must be converted to mass per charge ratio (*m/q*). To convert the scale we must find the constants of calibration *C* and *D* using the following formula which is derived in section 2.4.

$$\frac{m}{q} = (Ct + D)^2 \qquad\qquad (2.2)$$

Figure 5.2 shows the Uracil mass spectrum at 70 eV. Five prominent peaks in the spectrum were chosen.The square root of their mass was plotted against the corresponding time and a best fit line line was fitted to the data as shown in figure 5.3.
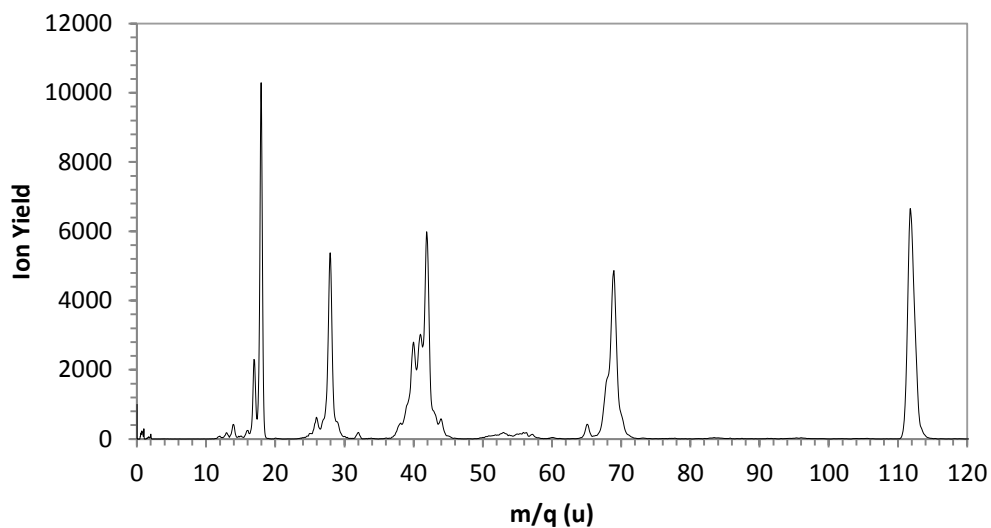
Figure 5.2. Uracil mass spectrum at 70 eV

$$y = 4.832x - 0.6584$$
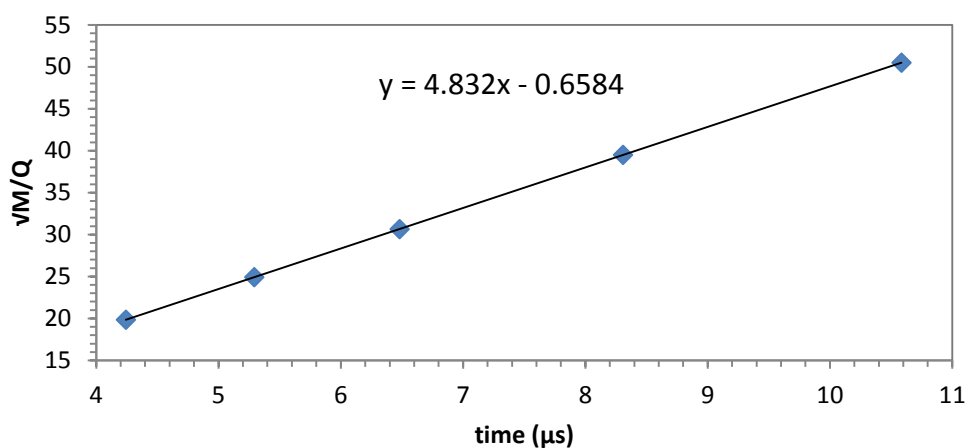
Figure 5.3. Evaluating constants of calibration

Using equation 5.1 the value for *C* was calculated to be 0.20695 ± 0.00005 and *D* was calculated to be 0.1363 ± 0.0018 (all uracil spectra and ion yield curves presented in chapter 6 have been obtained from a single measurement using these results).

5.3 Electron energy calibration

The water peaks in our mass spectrum shown in figure 5.2 have been used for the energy calibration. The 16, 17 and 18 u peaks are due to residual water vapour in the vacuum chamber. The ionization cross sections in the paper by Itikawa and Mason [47] are used for comparison. This paper contains a compilation of all the major cross section data for electron collisions with water molecules. For the energy calibration we are interested in the electron impact ionization cross section of the water molecules. This paper provides the relevant data from Straub et al [48] who used a parallel plate apparatus with a time of flight mass spectrometer and a position sensitive detector. Lindsay and Mangan [49] slightly corrected the original values of Straub et al. The partial ionization cross sections were made without resorting to any normalization procedure from other works. The uncertainty in their electron energy was ± 1 eV.

The ion yield curves for the 17 u and 18 u water peaks were determined using the peak fitting procedure described in section 4.4.4. The ion yield curves for the H_2O^+ and OH^+ were compared to the excitation functions from Itikawa and Mason. The ionisation energies of H_2O and OH^+ are 12.621 ± 0.002 eV and 18.117 ± 0.003 eV, respectively. The calibration constant was manually varied and the best overlap of the 17 u and 18 u ion yield curves in the region near threshold was obtained. These data indicates that in our experiment the incident electron energy is related to the voltage by:

$$E_i = V_I - 3.8$$

where E_i is the incident energy and V_i is the incident voltage.

The incident voltage here refers to the voltage of the Kepco power supply which determines the electron impact energy. The ionization yield curves obtained using a value of 3.8 as our calibration constant is shown in figure 5.4. The graph compares our ionization yield curves for 18 u (H_2O^+) and 17 u (OH^+) to the data from Itikawa and Mason.
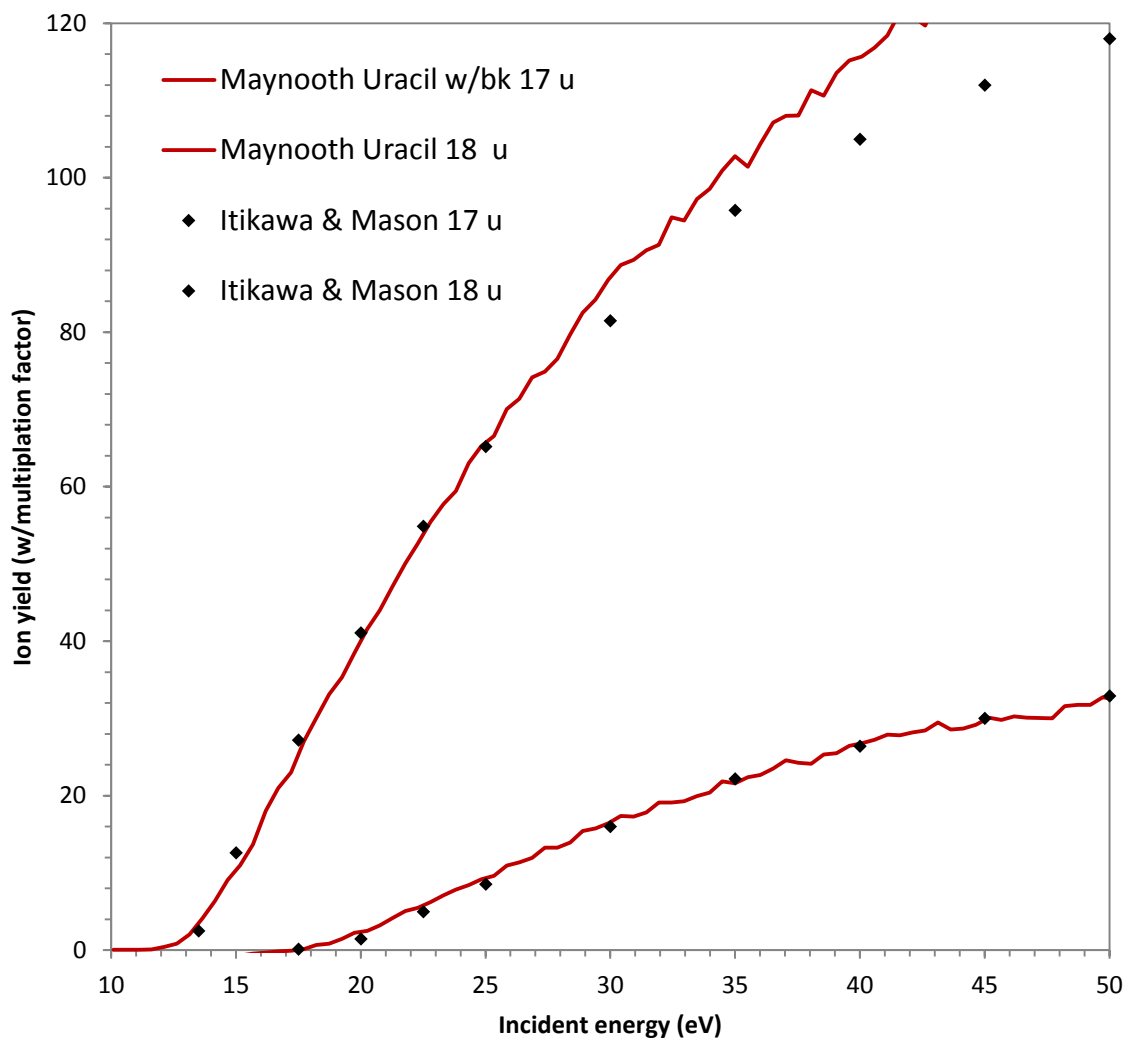

Figure 5.4. Ionization yield curves of 17 u and 18 u compared to Itikawa & Mason

The 16 u ionization yield curve has a much lower yield and has not been used for the energy calibration.

Chapter 6: Electron impact fragmentation of uracil

6.1 Introduction

This chapter will look at the experimental work carried out using the effusive source. The total ionization cross section and normalization of the data is presented in section 6.2. The relative yields of the positive ionised fragments are compared with other research groups in section 6.3. The appearance energy measurements are presented in section 6.4 and the fragmentation processes are discussed in section 6.5.

All uracil mass spectra and ion yield curves presented in this chapter have been obtained using the effusive source experimental set up described in chapter 3. The incident electron energy was varied from 0 to 100 eV in 0.5 eV steps using the programmable power supply described in section 5.4. All ion yield curves have been generated from a single data set. 12 cycles were measured in total to make up the data set using the data acquisition methods described in chapter 4. Assuming that the detection efficiency of the RTOFMS is mass independent, all ion yield curves are on the same relative scale.

Taking the mass range of the peaks, corresponding bin range, location of the largest peak and the number of identified peaks from our calibrated mass spectrum described in section 5.2, we can obtain ionization yield curves using the Guassian fitting procedure described in section 4.4.1. Each ion yield curve measures the peak area of a single fragment as a function of electon incident energy. We obtained the partial ionization cross section for each fragment by normalizing the ion yield curves with the same normalization factor that is used for the total ionization cross section. The appearance energies and fragmentation processes will be anaylsed and discussed in more detail in section 6.4 and 6.5, respectively.
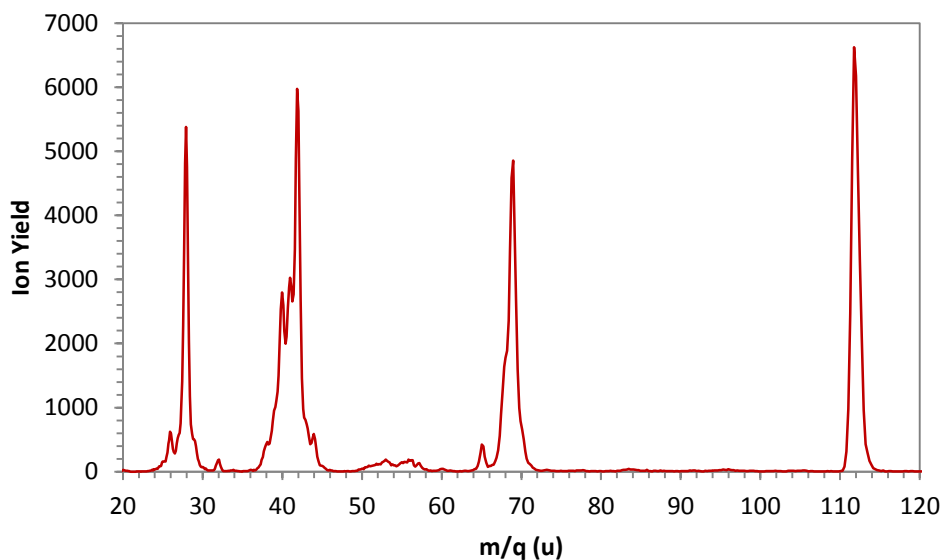
Figure 6.1. Uracil mass spectrum at an electron impact energy of 70 eV.

The uracil mass spectrum shown in figure 6.1 is measured at an electron impact energy of 70 eV. The main uracil parent ion at 112 u is present in our mass spectrum (and there is a presence of a very weak peak at 113 u possibly due to a uracil isotope). The 69 u fragment has been identified as the largest peak in the range of 66 - 71 u. A weak fragment at 65 u was identified that was not identified by other groups. The 50 - 60 u masses were not analysed because they have very low yields and are not well resolved. The 42 u fragment is the most abundant peak in our mass spectrum. Weak fragments in the spectrum (less than 5% of the relative yield of the 42 u peak) have not been analysed. The 26 u, 27 u, 28 u and 29 u fragments are present in our spectrum with the 28 u fragment the most abundant in the group. Our mass spectrum also indicates a weak presence of the 12-15 u fragments. The 17 and 18 u fragments have been analysed in the previous section as part of the energy calibration. These fragments are due to water vapour in our vacuum system. They have not been included in this mass spectrum as they are not fragments of the parent molecule. The 16 – 18 u fragments are much weaker than the 12-14 u fragments in the 70 eV mass spectrum of Imhoff et al [24]. Assignments of molecular configuration for each of these fragments will be discussed in section 6.6.

6.2 Total ionization cross section and normalization of the data
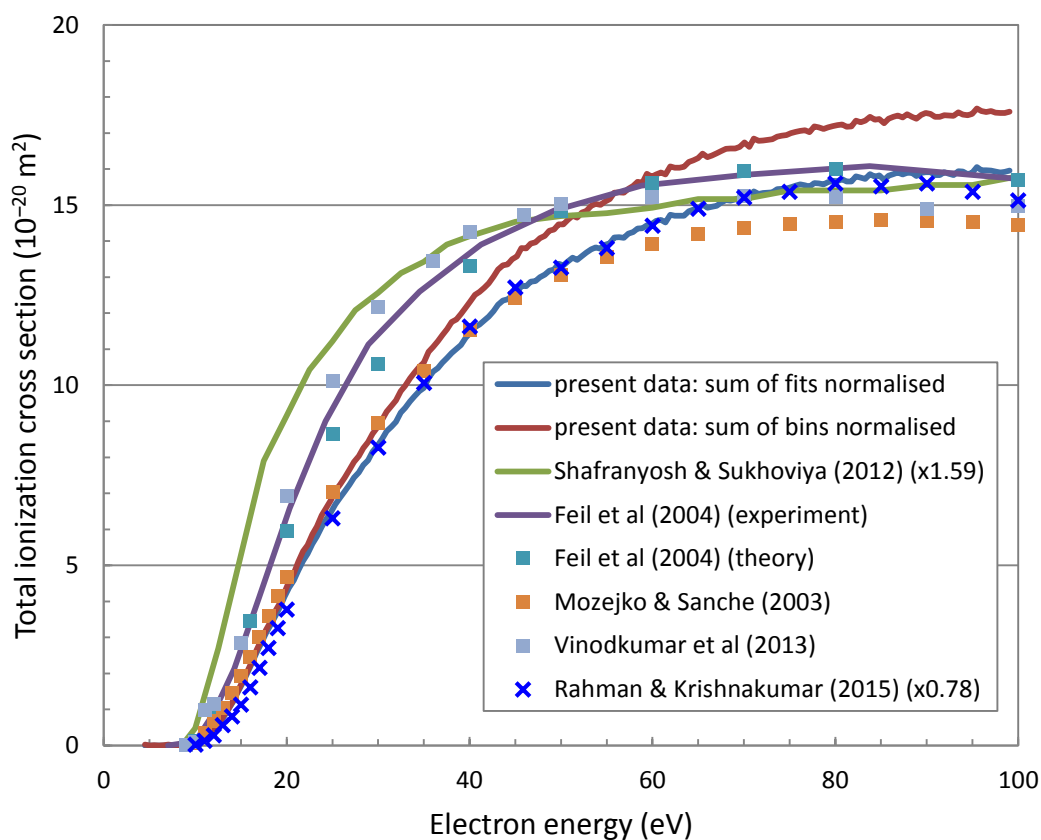
Figure 6.2. Total ionisation cross section of the sum of our fitted data and the sum of all the counts in our spectra compared to the theoretical models of Feil et al [25], Mozejko and Sanche [29] and Vinodkuma et al [30]. The experimental ionization cross sections from Feil et al [25], Shafranyosh et al [26] and M.A. Rahman and E. Krishnakumar [27] are also compared.

We have obtained two curves for the total ionization cross section as a function of electron impact energy. The sum of all our ion yields ("sum of fits") using the described Guassian fitting procedure and the sum of all the counts in our mass spectra ("sum of bins"). All ion yield curves are on the same relative scale assuming the ion collection and detection efficiency of the mass spectrometer is mass independent. This allows us to normalize the ("sum of fits") curve to the theoretical total ionisation cross section. The ("sum of fits") curve slightly underestimates the

total ionization cross section as weak fragments with less than 5% of the relative yield of the 42 u ion were not fitted. The ("sum of bins") curve slightly overestimates the total ionization cross section because it contains the background signals between the uracil peaks. Both curves exclude the contributions from 16, 17 and 18 u.

Shown in figure 6.2 is the total ionization cross section curves obtained from our data set compared to both experimental and theoretical data of Shafranyosh et al [27], Vinodkumar et al [30], Feil et al [25], Mozejko & Sanche [29] and M.A. Rahman and E. Krishnakumar [27]. Our "Sum of fits" curve was normalised to the average theoretical cross sections of Vinodkumar et al, Feil et al and Mozejko & Sanche at 70 eV using a factor of 7.70 x 10^{-5}. This factor was then applied to our sum of bins curve.

The normalization provides good agreement to the theoretical model of Mozejko & Sanche. Our curves rise less rapidly at low energies compared to Vindokumar et al and the theoretical model of Feil et al. The curves of Vindokumar et al and the theoretical model of Feil et al reach a maximum at around 70 eV where our curves have a maximum at around 100 eV. The other experimental results had a lower threshold than both our curves. There is good agreement between our sum of fits curve and the curve of M.A. Rahman and E. Krishnakumar. After 70 eV our "Sum of fits" curve provides better agreement with the experimental results of Feil et al. It is shown that there is a significant difference in shapes between our curves and the curve by Shafranyosh et al. They were able to put their cross sections on an absolute scale by measuring the density of the molecules in the beam by condensing their uracil beam onto a plate held at liquid nitrogen temperature. Based on the good agreement, all our ion yield curves can be normalised using the same factor to obtain partial ionisation cross sections
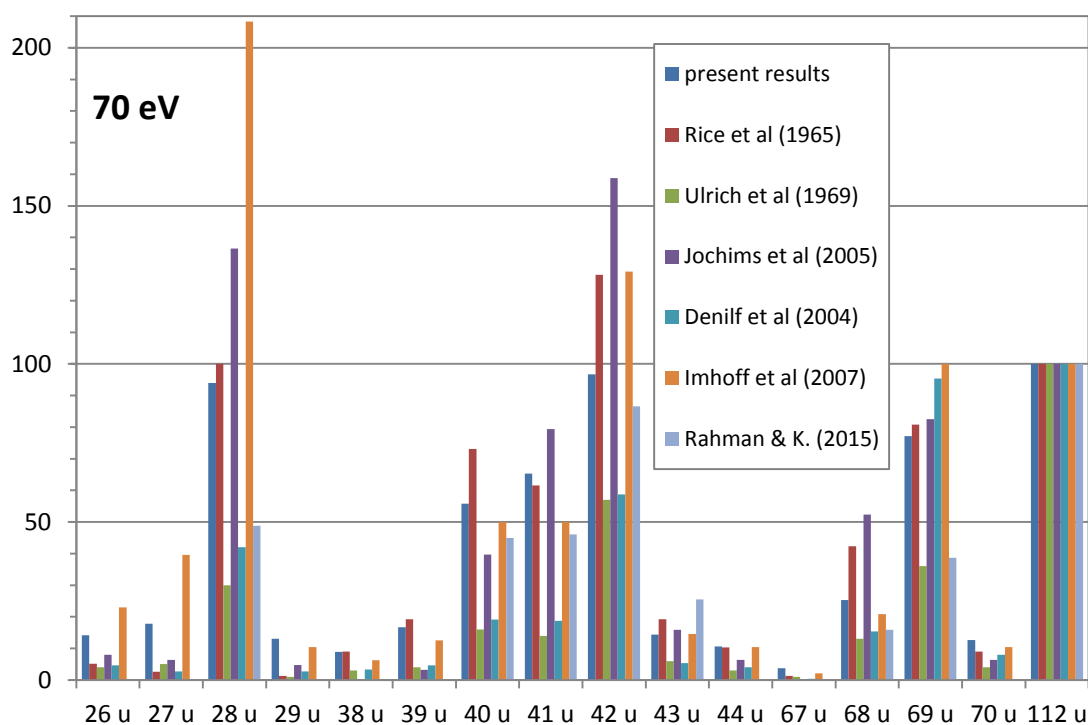
6.3 Relative yields of the fragment ions

Figure 6.3. Comparison of relative fragment yields of uracil fragments ions. All measurements are with 70 eV electron impact, except the yields of Jochims et al which were obtained with 20 eV photon impact.

The relative intensities of the peaks in our uracil mass spectrum at 70 eV are compared with Denifl et al [5], Rice et al [21], Ulrich et al [22], Imhoff et al [24], M.A. Rahman and E. Krishnakumar [27] and Jochims et al [50]. The intensity of the peaks in each spectrum are set relative to the 112 u peak. Rice et al, Jochims et al and Denifl et al all measured the 42 u peak to have the highest intensity in their spectra. Imhoff et al have have measured the 28 u peak to have the highest intensity in their spectrum. There is substantial differences in the ion yields, in particular the 28 u and 40 – 42 u ions. Our ion yields are in good agreement with the ion yields of Rice et al, but substantially higher than the ion yields of M.A. Rahman and E. Krishnakumar, and substantially lower than the yields of Imhoff et al. The intensity of our parent ion peak at 112 u and the 42 u fragment shows a

similar intensity. The yields for the 42 u, 69 u and the 112 u will be compared and discussed with Feil et al [25] and Shafranosh et al [26] in section 6.4

6.4. Gaussian peak fitting

6.4.1 The 12-15 u group.

Figure 6.4 shows the 12-15 u group of peaks from our mass spectrum. The figure compares the model fit (solid blue line) with the ion yield data. The partial ionization cross sections for this group are shown in figure 6.5. The 14 u peak is the largest peak in the group. This group has the lowest yields of all the groups analysed. All fragments exhibit a different response to electron impact and this is shown by the shapes of the partial ionization cross sections. Rice et al [21] have assigned C^+, CH^+, CH_2^+ and CH_3^+ as the fragments in this group.
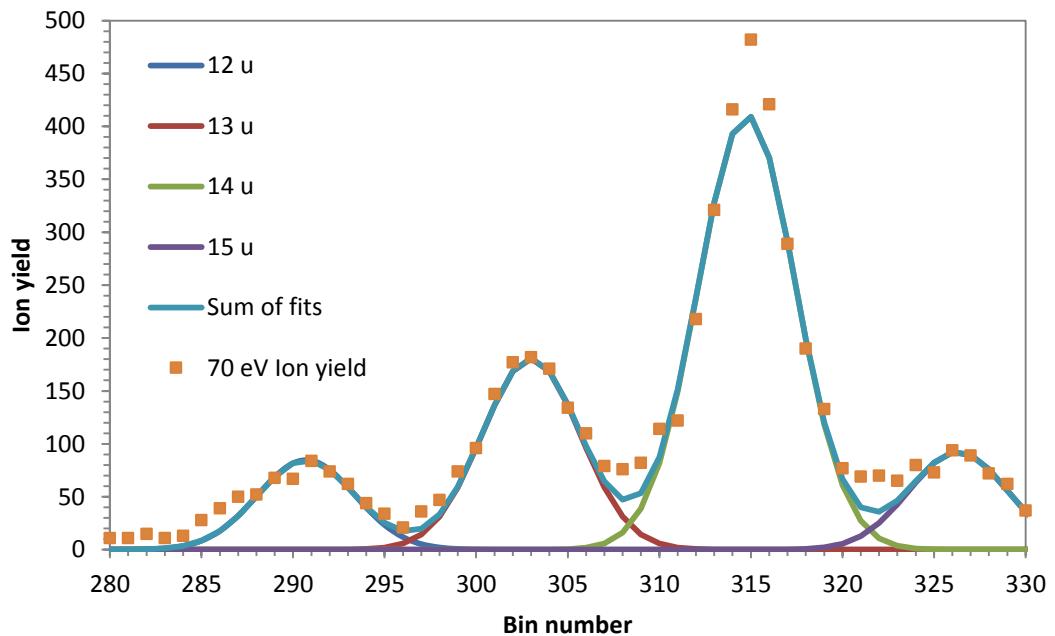
Figure 6.4. Comparison between the Gaussian peak fitting results and the individual peak yields at 70 eV for the 12-15 u group.
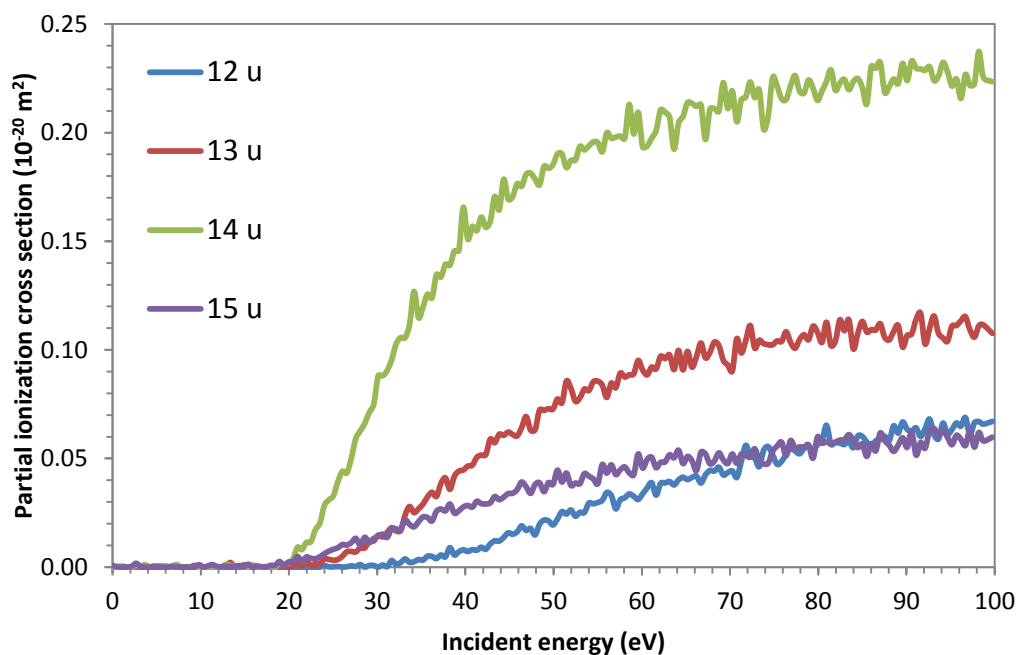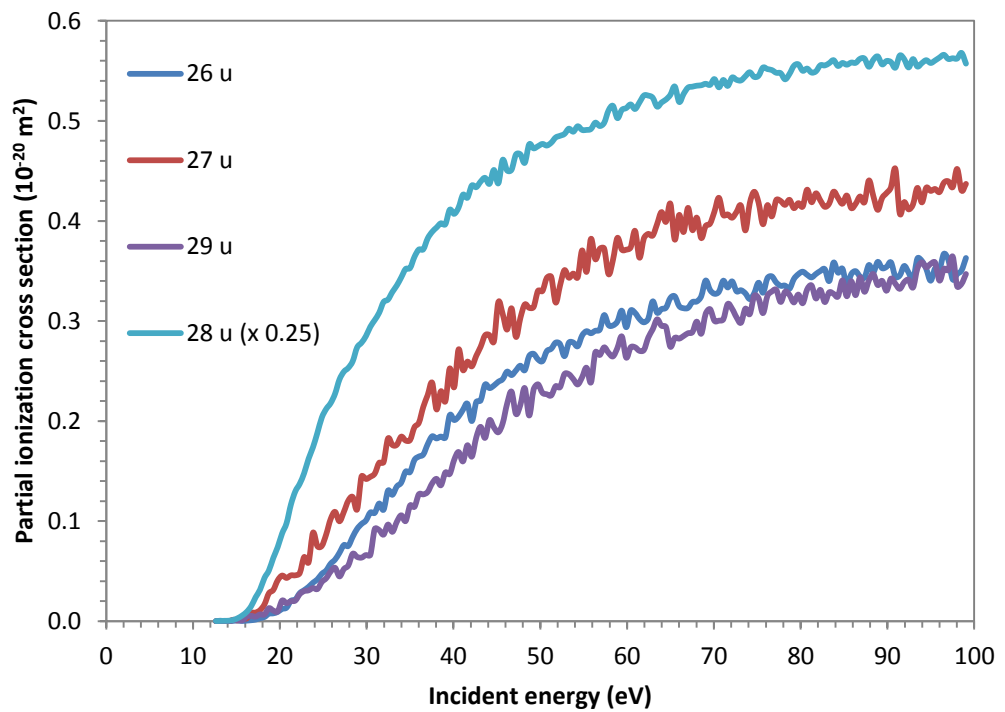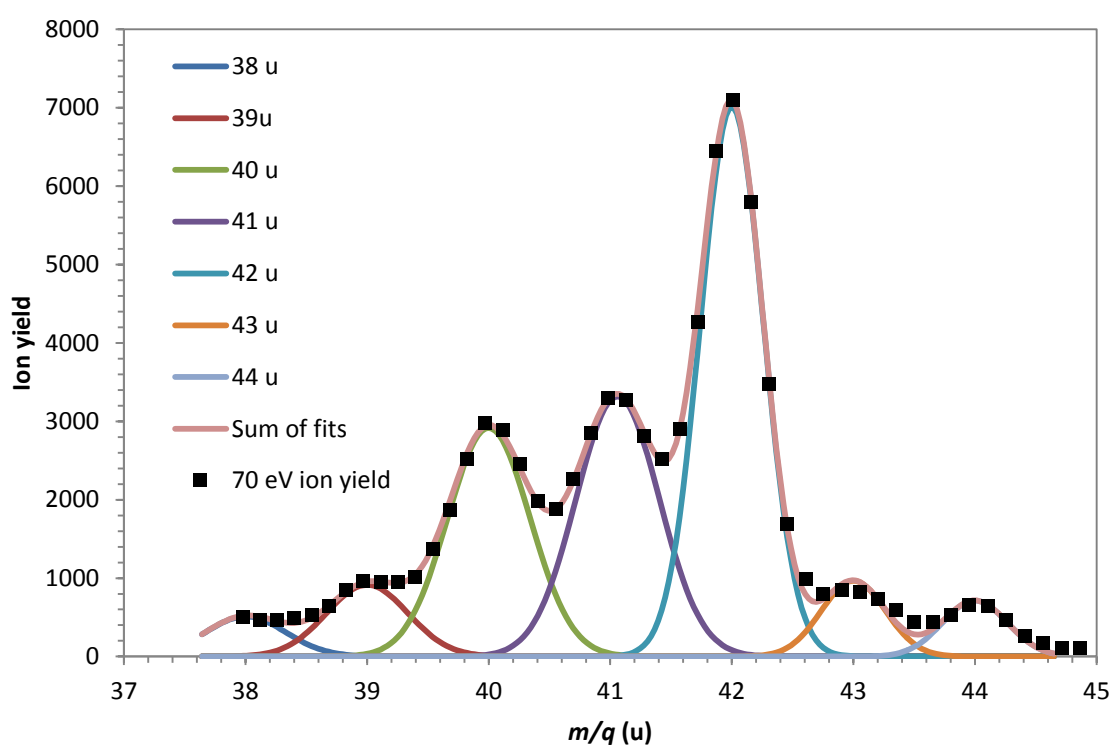
Figure 6.5. Partial ionization cross sections of the 12 – 15 u group.

6.4.2 The 26-29 u group.

Figure 6.6 shows the 26-29 u group of peaks from the mass spectrum. The partial ionization cross sections for this group are shown in figure 6.7. The 26, 27 and 29 u peaks exhibit a low yield in comparison to the 28 u peak (A multiplication factor was used for the 28 u to allow it to be displayed with the other curves). The partial ionization cross section curves exhibit similar shapes in this group. Rice et al [21] have assigned the molecule CH_2N^+ as the largest fragment in this group.
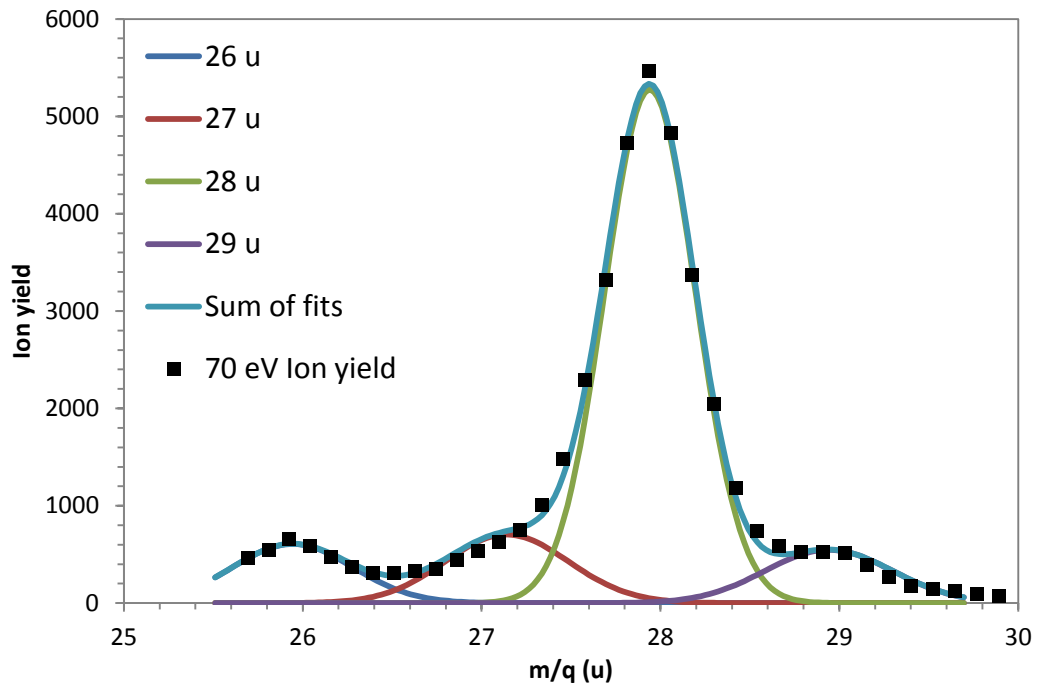
Figure 6.6. Comparison between the Gaussian peak fitting results and the individual peak yields at 70 eV for the 26-29 u group.
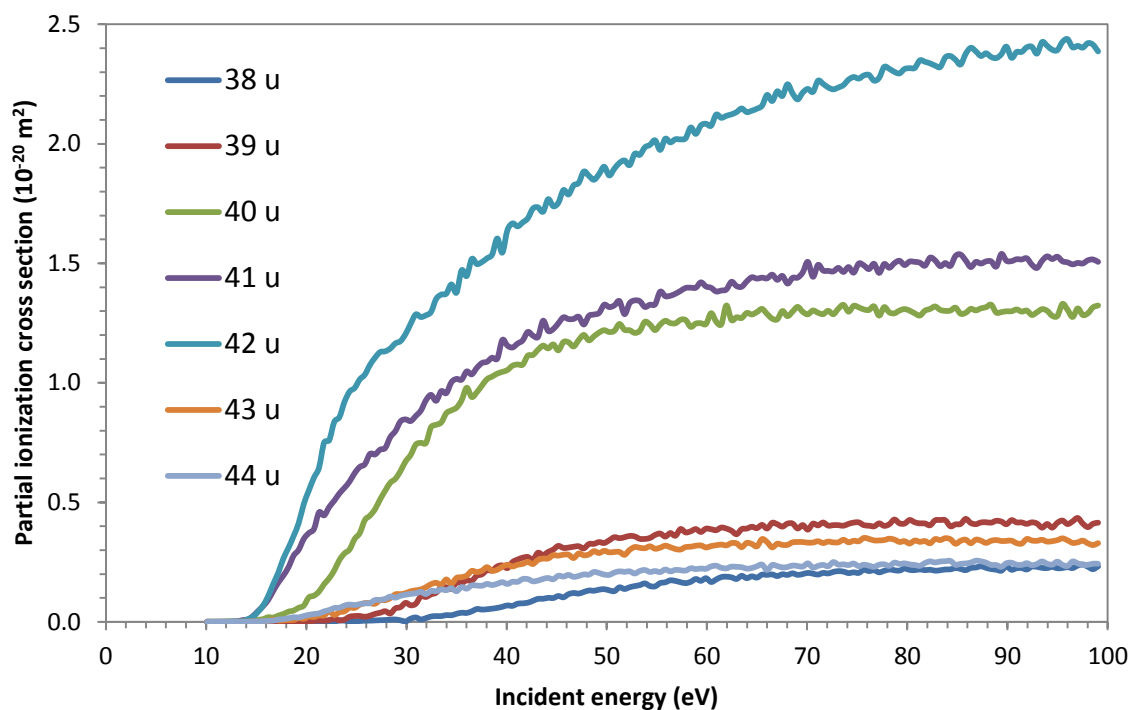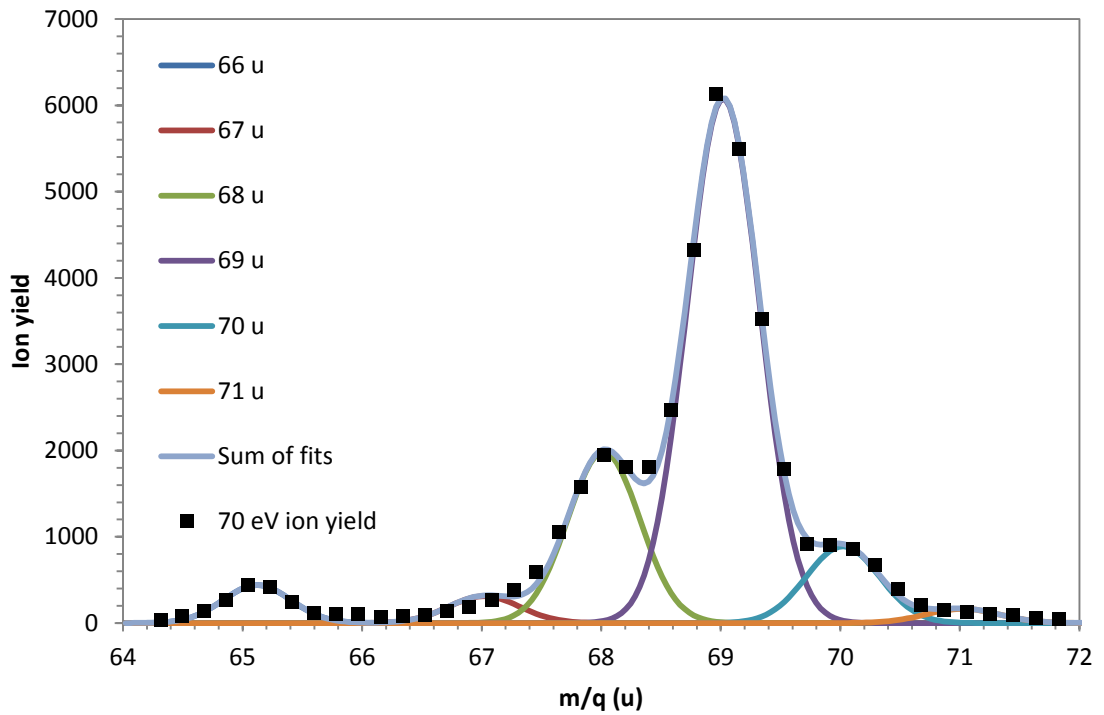

Figure 6.7. Partial ionization cross sections of the 26 – 29 u group.

6.4.3 The 38-44 u group

Figure 6.8 shows the 38-44 u group from the mass spectrum. The ion yield curves (figure 6.9) in this group have the largest fragment yields. The shapes of the partial ionization cross section curves in this group all appear to be different indicating that fragments in the same group are undergoing different fragmentation processes. The 38 u curve has the highest appearance energy (see section 6.5). Rice et al [21] have assigned the molecule $C_2H_2O^+$ as the largest fragment in this group.

Figure 6.8. Comparison between the Gaussian peak fitting results and the individual peak yields at 70 eV for the 38 - 44 u group.

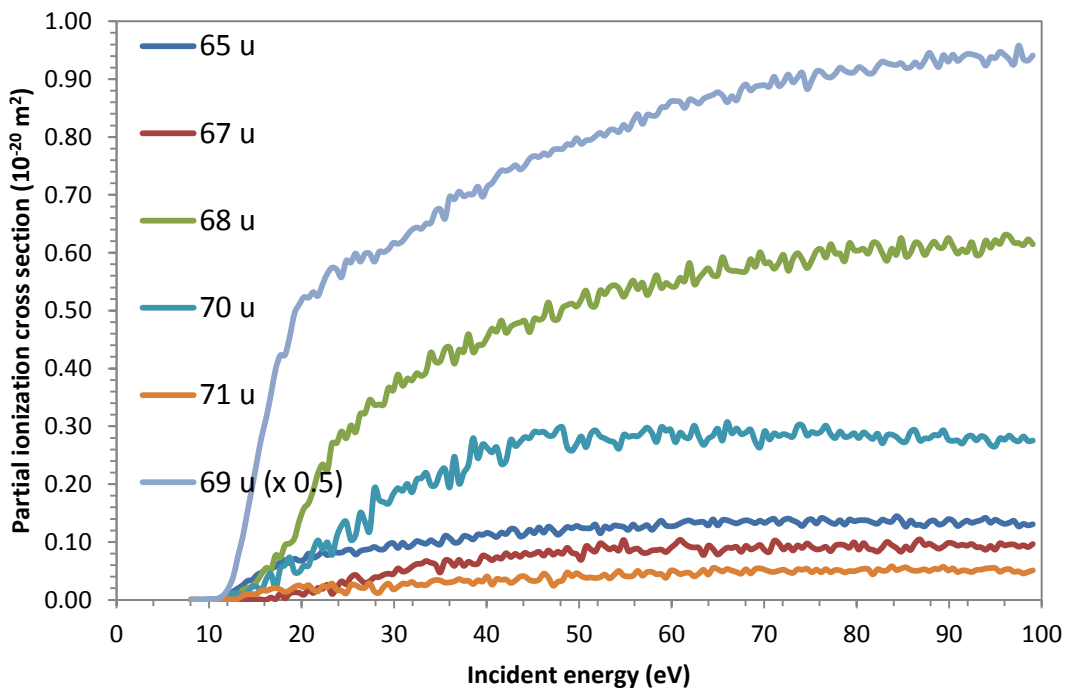**Figure 6.9.** Partial ionization cross sections of the 38 – 44 u group.

6.4.4. The 65 - 71 u group.

Figure 6.11 shows the 65 - 71 u group of peaks from the mass spectrum. The Partial ionization cross section curves for this group are shown in figure 6.12. The 65, 67 70 and 71 u peaks exhibit a low yield in comparison to the 68 and 69 u peaks (a multiplication factor was used for the 69 u peak). The 68 and 69 u ion yield curves are shown to exhibit similar shapes above 40 eV. $C_3H_3NO^+$
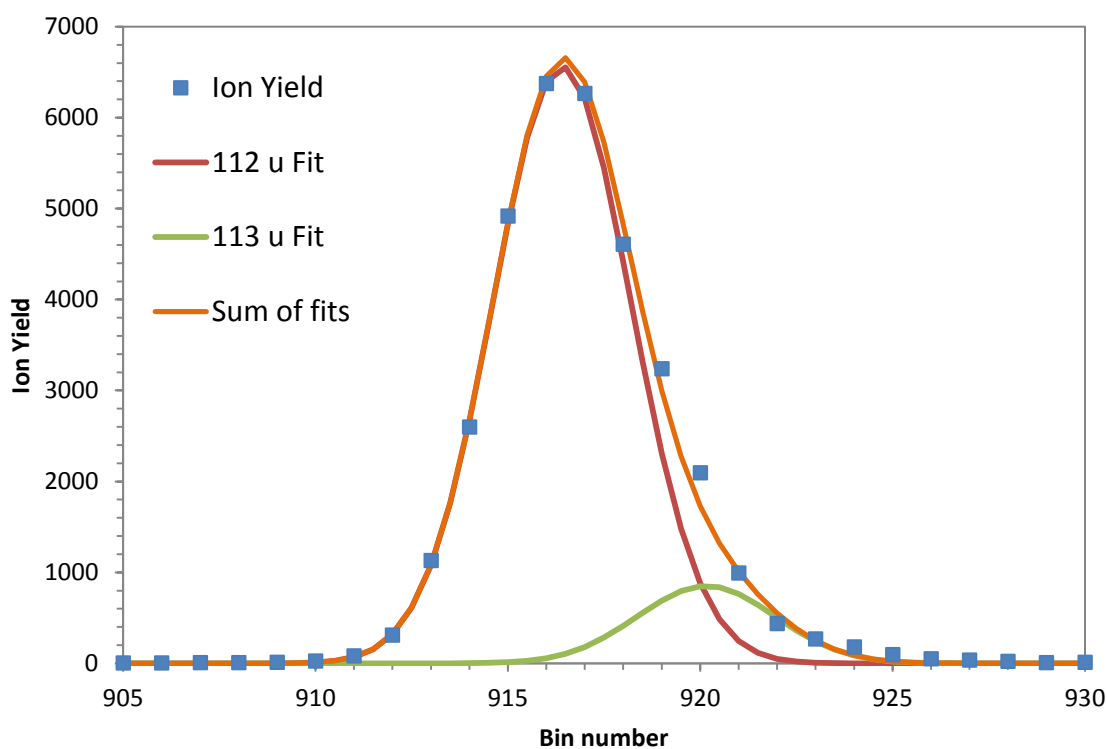
Figure 6.10. Comparison between the Gaussian peak fitting results and the individual peak yields at 70 eV for the 66-71 u group.

Figure 6.11. Partial ionization cross sections of the 66 – 71 u group

6.4.5 The 112-113 u group.

Figure 6.12 shows the 112 - 113 u group of peaks from the mass spectrum. The partial ionization cross section curves for this group are shown in figure 6.13. The main uracil parent ion at 112 u is the parent ion, and there is a presence of a very weak peak at 113 u due to uracil containing a ^{13}C natural isotope. The fits of the 112 - 113 u group of peaks converged well, but the low yield of the 113 u peak directly adjacent to the high yield 112 u peak may add some uncertainty to the precise shape of the 112 u ionization yield curve. For this reason we have included the ion yield curve for the sum of the 112 and 113 u ions. The sum of fits is identical to the sum of bins in this mass range. The parent peak at 112 u is the most intense in our spectra out of all the peaks fitted. The intensities of the other principal peaks are in the order 42 u > 69 u > 28 u (see figure 6.3).

Figure 6.12. Comparison between the Gaussian peak fitting results and the individual peak yields at 70 eV for the 112-113 u group.
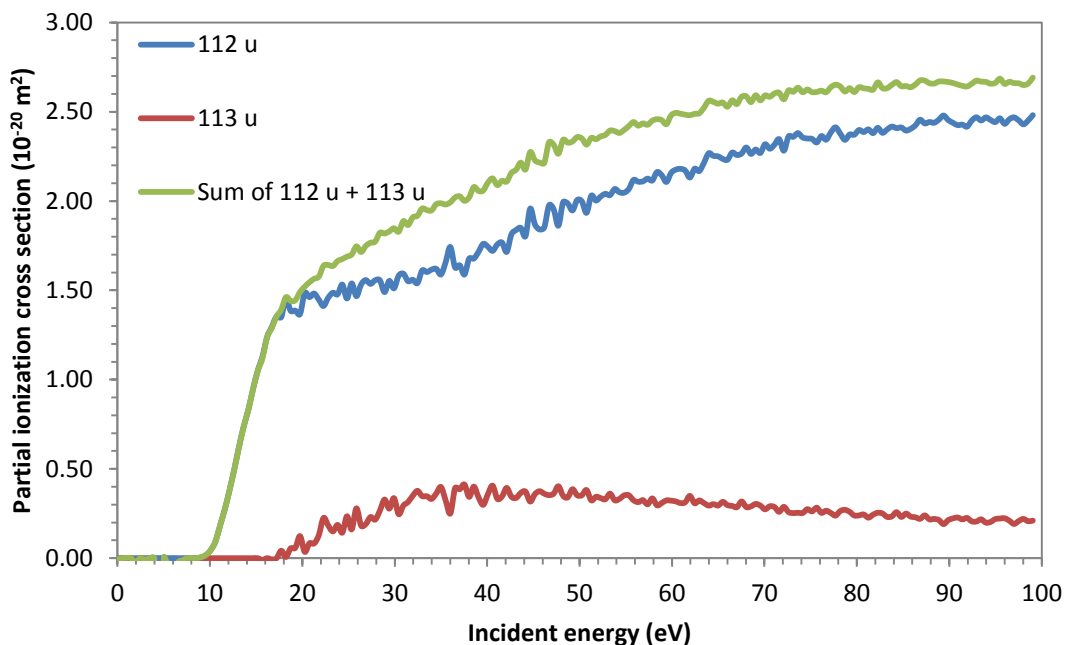
Figure 6.13. Partial ionization cross sections of the 112-113 u group

6.4.6 Partial ionization cross section comparisons

Partial ionization cross sections for positive fragments of uracil have been reported by Feil et al [25], Shafranyosh et al [26] and M.A. Rahman and E. Krishnakumar [27]. The curves from Shafranyosh et al have been read from the graphs in their papers, the data of Feil et al was provided to us by Prof. Paul Scheva, and the data of M.A. Rahman and E. Krishnakumar is from their table 3. We have not included any multiplication factors in the data. These graphs clearly show differences in the relative yields of the 112 u, 69 u and 42 u fragment. For instance the partial ionization cross section of the 42 u fragment are in reasonable agreement, where as the 112 u + 113 u cross sections is about 60 % of the cross section measurement of Feil et al. We note however that our relative yields for these fragments are in much better agreement with Rice et al [21] see figure 6.3. The shapes of the 112 u + 113 u and the 69 u curves show a faint undulation in the range of 20 – 40 eV, which could be due to variation in the overlap of the electron beam with the molecular beam.
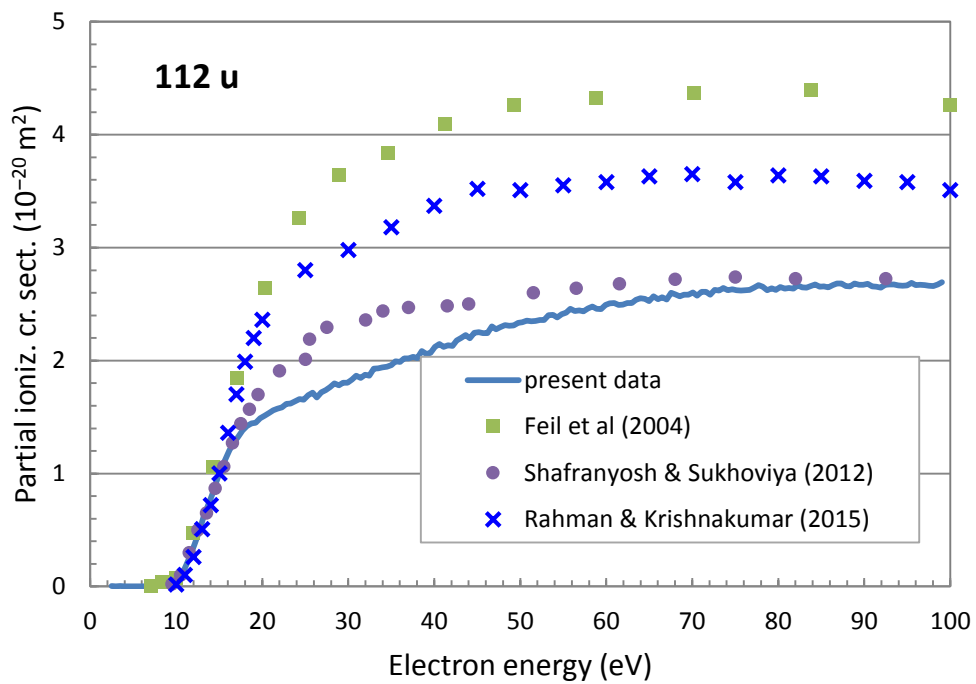
Figure 6.14. Partial ionization cross section comparisons of the parent molecule
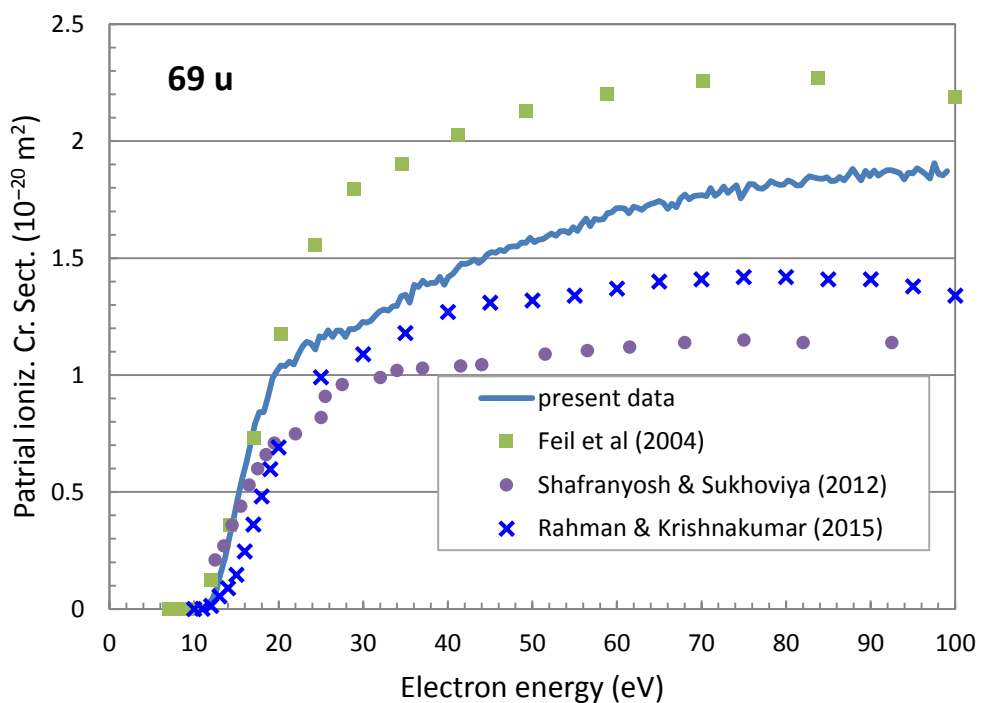

Figure 6.15. Partial ionization cross section comparison of the 69 u ion.
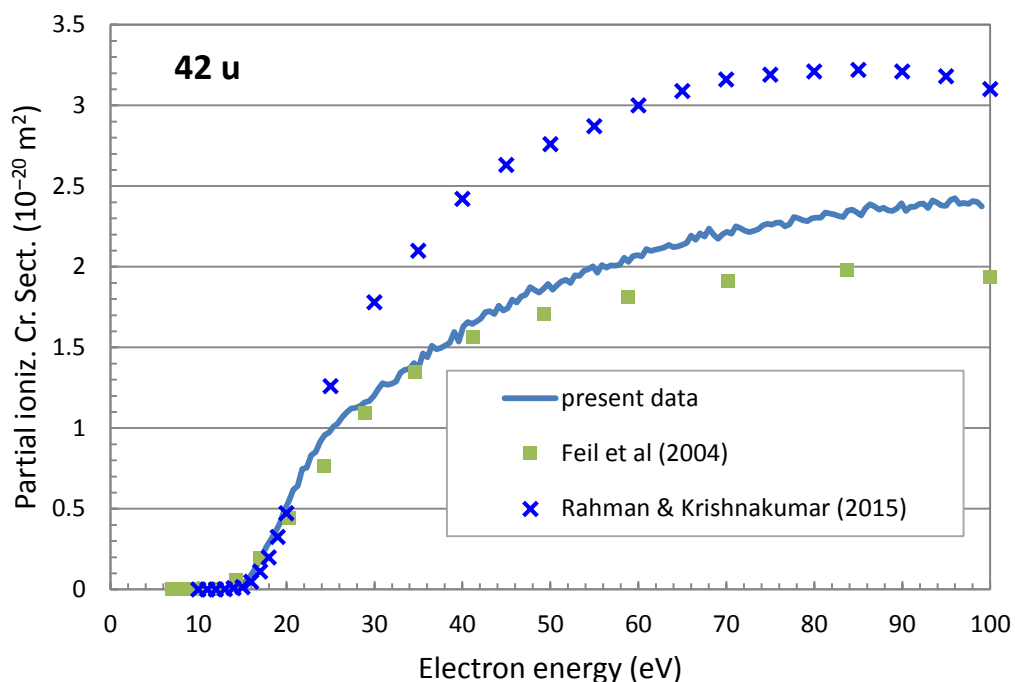
Figure 6.16. Partial ionization cross section comparison of the 42 u ion.

6.5 Appearance energies

The appearance energy is the minimum electron impact energy supplied to an atom or molecule to produce an ion of a particular mass. The appearance energy indicates the lowest energy at which a fragment appears in a mass spectrum. The appearance energies are important because they give an indication of the fragmentation sequence as the incident energy increases. Our measurements of the appearance energies of fragment ions enable us to further investigate the validity of the fragmentation pathways identified in previous work and to consider new aspects and extensions of the fragmentation processes.

Using our ionization yield curves we could determine the appearance energies using the fit procedure described in chapter 4. The appearance energy for each fragment in our mass spectra is shown with the uncertainty in table 6.1. The best fit values

and their uncertainties are based on the range of data points used in the model. The uncertainties are based on the fits only and do not include the error in the energy calibration. The table compares the appearance energies from the present data to Denifl et al [5], M.A. Rahman and E. Krishnakumar [27] and Jochims et al [50]. Except for 40 u, we did not find indications for a second onset. The fitting of a single onset produced the best results and agreed well with the results from the other groups as seen in table 6.1 and 6.2. Table 6.2 lists all the measured and calculated appearance energy values for the parent ion from a number of different groups.

Mass (amu)	Present data Electron impact	Denifl et al [5] Electron impact	M.A. Rahman et al [27] Electron impact	Jochims et al [50] Photon impact
13	19.8 ± 2.3		11 ± 0.9	
14	18.69 ± 0.26		12.5 ± 0.7	
15	16.9 ± 1.4		13.5 ± 0.7	
26	16.3 ± 0.39		15.5 ± 0.7	
27	14.56 ± 0.18	14.77 ± 0.92	13.5 ± 0.7	
28	13.40 ± 0.29	13.83 ± 0.39	13.7 ± 0.7	13.75 ± 0.05
29	13.71 ± 1.2			
38	21.77 ± 0.45		12 ± 0.7	
39	16.52 ± 0.72		14 ± 0.9	
40	13.01 ± 0.66		14.5 ± 0.9	14.06 ± 0.10
41	13.21 ± 0.25	13.32 ± 0.18	11.5 ± 0.7	12.95 ± 0.05
42	13.07 ± 0.24	13.41 ± 0.10	13 ± 0.7	13.25 ± 0.05
43	13.58 ± 0.78	13.36 ± 0.30	13.5 ± 0.6	13.6 ± 0.2
44	13.98 ± 0.26			
65	10.92 ± 0.15			
66	12.81 ± 0.54			
68	12.36 ± 0.29	12.75 ± 0.66	11.5 ± 0.9	13.40 ± 0.05
69	10.84 ± 0.17	10.89 ± 0.07	11.5 ± 0.7	10.95 ± 0.05
70	11.04 ± 0.84			

Table 6.1. Comparison of the present appearance energy values for positive uracil fragment ions with previous determinations by Denifl et al [5], M.A. Rahman and E. Krishnakumar [27] and Jochims et al [50].

Author	Method	Appearance energy (eV)
Present	Electron impact	9.15 ± 0.21
Denifl et al [5]	Electron impact	9.59 ± 0.08
Lifshitz et al. [51]	Electron impact	9.82 ± 0.1
Jochims et al [50]	photoelectron spectroscopy	9.15 ± 0.03
Verkin et al. [52]	photoelectron spectroscopy	9.35 ± 0.1
Zaretskii et al. [53]	photoelectron spectroscopy	9.53 ± 0.02
Padva et al. [54]	photoelectron spectroscopy	9.59 ± 0.02
Hush et al. [55]	photoelectron spectroscopy	9.50 ± 0.03
Dougherty et al. [56]	photoelectron spectroscopy	9.60/9.34
Lauer et al. [57]	photoelectron spectroscopy	9.45
Palmer et al. [58]	photoelectron spectroscopy	9.68
Yu et al. [59]	photoelectron spectroscopy	9.59 ± 0.03
Urano et al. [60]	photoelectron spectroscopy	9.59
Kubota and Kobayazhi [61]	photoelectron spectroscopy	9.53 ± 0.01
Wetmore et al. [62]	Theory	9.47/9.21
Russo et al. [63]	Theory	9.25

Table 6.2. Comparison of the present appearance energy value for the parent cation of uracil with previous determinations of the vertical ionization energy of uracil.
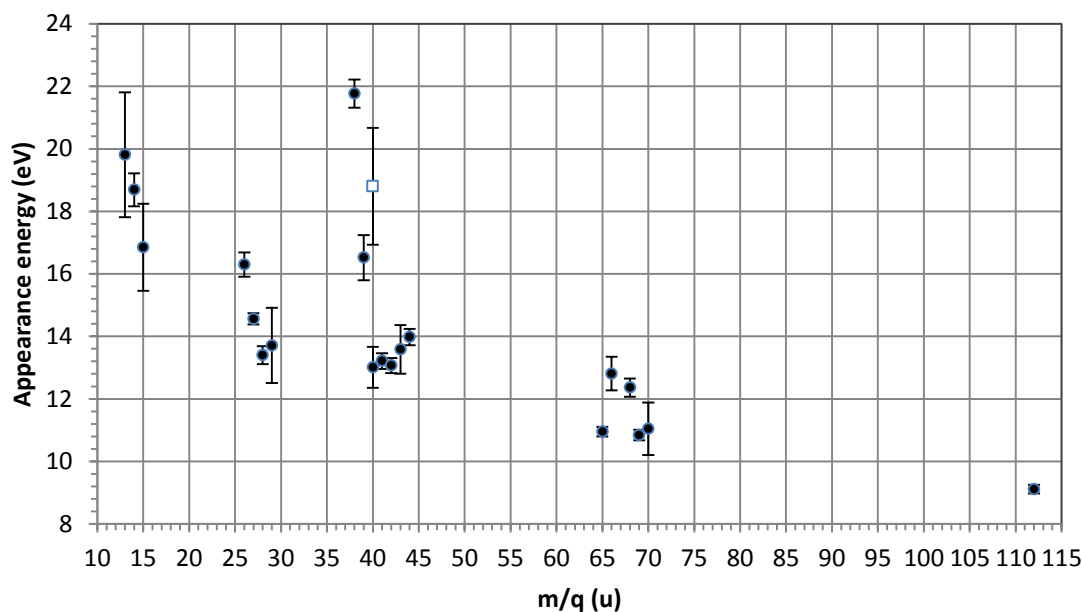
Figure 6.17. Appearance energies for positive fragment ions of uracil. The appeance energies are shown as solid circles (higher onset shown as open square).

Figure 6.17 shows the appearance energies obtained for each of the uracil fragments. This figure gives an indication of the fragmentation sequence as the incident energy increases. Our appearance energy for the parent ion is 9.15 ± 0.21 eV. Our appearance energy for the parent ion is in good agreement with Jochims et al [50] shown in table 6.2. Our measured appearance energy value for the parent ion represents the lowest appearance energy of all the measured fragments. Rahmen et al determined AE's by using "linear fits" but it is not clear whether this was done by hand, or by using a numerical method.

The second lowest appearance energy is 10.84 ± 0.17 eV for the 69 u ion. Denifl et al [5] measured an appearance energy of 10.89 ± 0.07 eV for the 69 u ion, which is close to our value of 10.84 ± 0.17 eV. All other appearance energies from the group of peaks from 65 u to 70 u are all between 10.84 and 12.81 eV. The 68 u ion appearance energy of 12.36 ± 0.29 eV was measured to be lower than the values obtained by Denifl et al [5] and Jochims et al [50].

All smaller fragments (44 u and lower) have appearance energies above 13.01 eV, indicating that all these fragments are the result of successive fragmentations *via* 112 u and 65–70 u. Denifl et al also determined the appearance of the 56 u fragment. The group of peaks in our data which contained the 56 u ion had very low yields so they were not analysed. We find that the 42 u ion has an appearance energy of 13.07 ± 0.24 eV compared to 13.25 ± 0.05 eV of Jochims et al and 13.41 ± 0.1 eV of Denifl et al. For the 40 u fragment we measured a second onset. The difference in energy between the first and second onset is 4.2 eV. It is unlikely that this second onset is linked to tautomerization, because the relative energies of the uracil tautomers are less than 0.3 eV [64]. We find that the 28 u ion has an appearance energy of 13.40 ± 0.29 eV and is in good agreement when compared to 13.83 ± 0.39 eV of Jochims et al and 13.75 ± 0.05 eV of Denifl et al. The ion yield curves of 12 u, 13 u and 14 u show indications of higher onsets but were difficult to determine accurately due to the low yields. Figures 6.18 – 27 show the partial ionization cross sections with the model onset function fit for all the measured fragments.
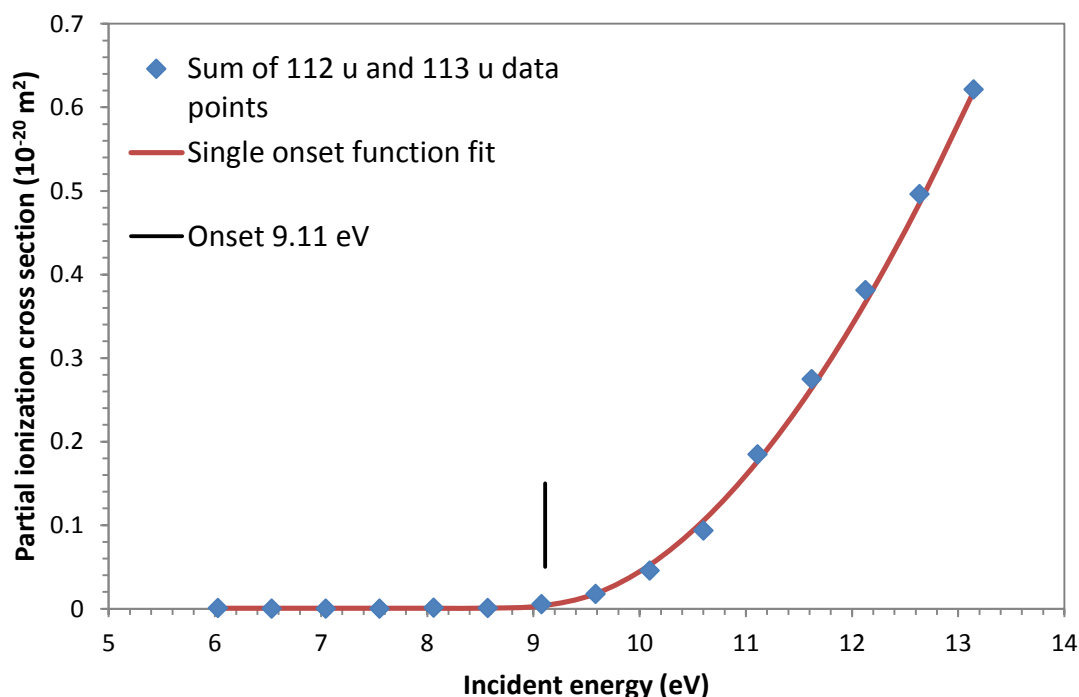
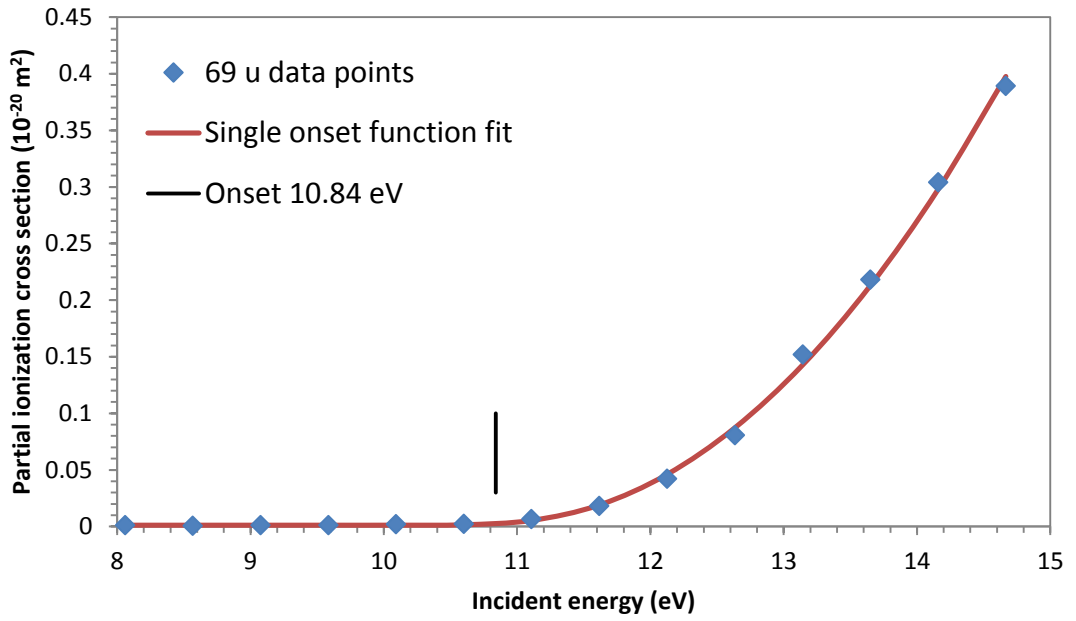**Figure 6.18.** Partial ionization cross section of the 112 u fragment.

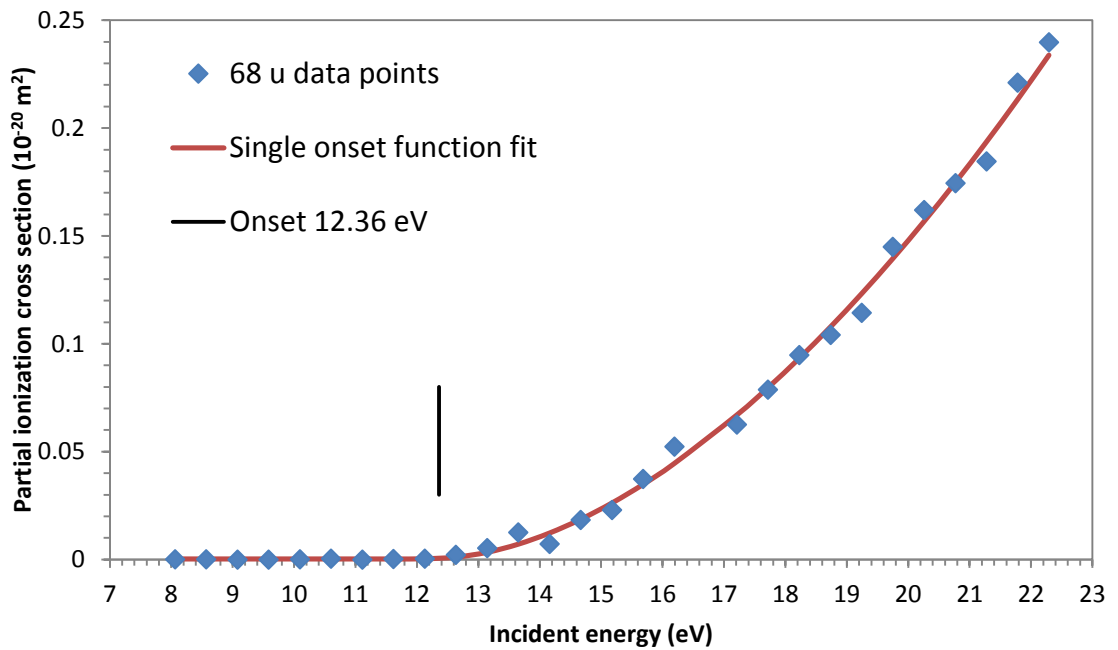**Figure 6.19.** Partial ionization cross section of the 69 u fragment.

Figure 6.20. Partial ionization cross section of the 68 u fragment.
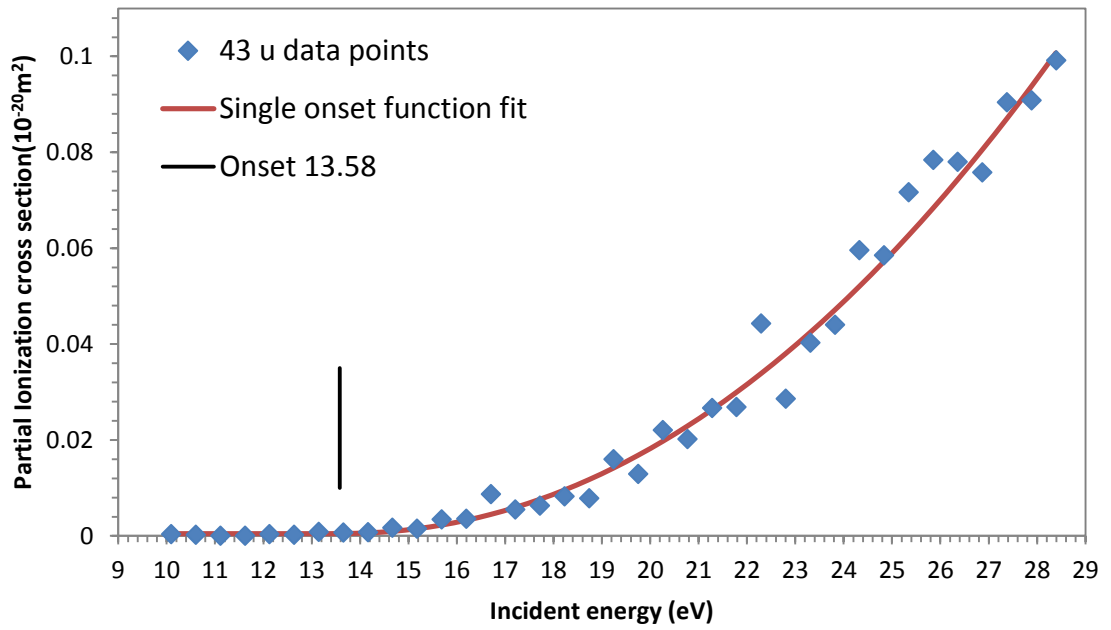
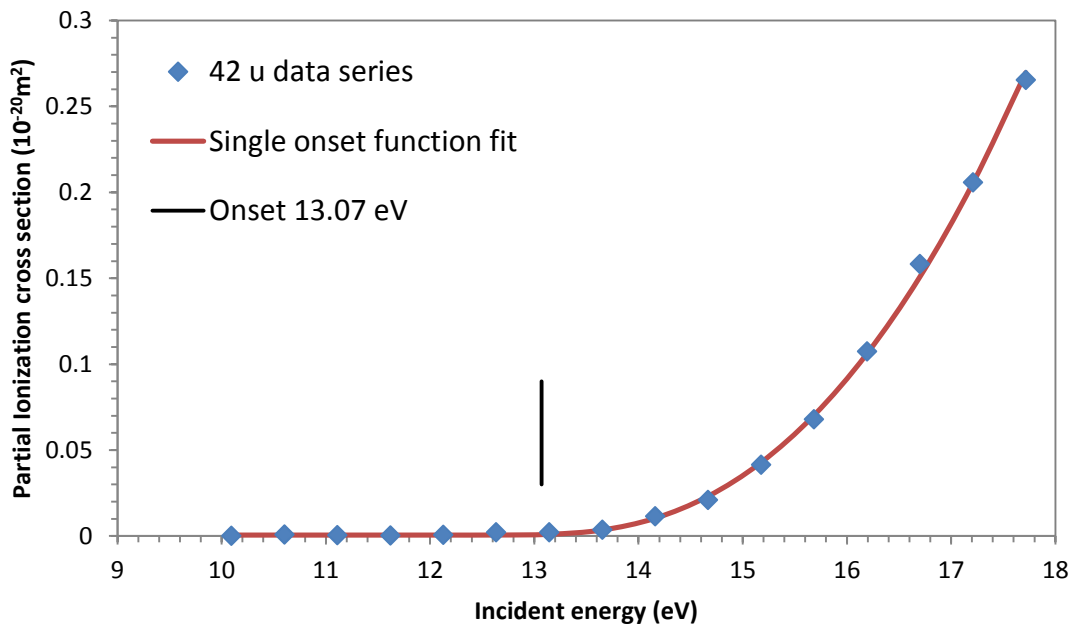**Figure 6.21.**Partial ionization cross section of the 43 u fragment.

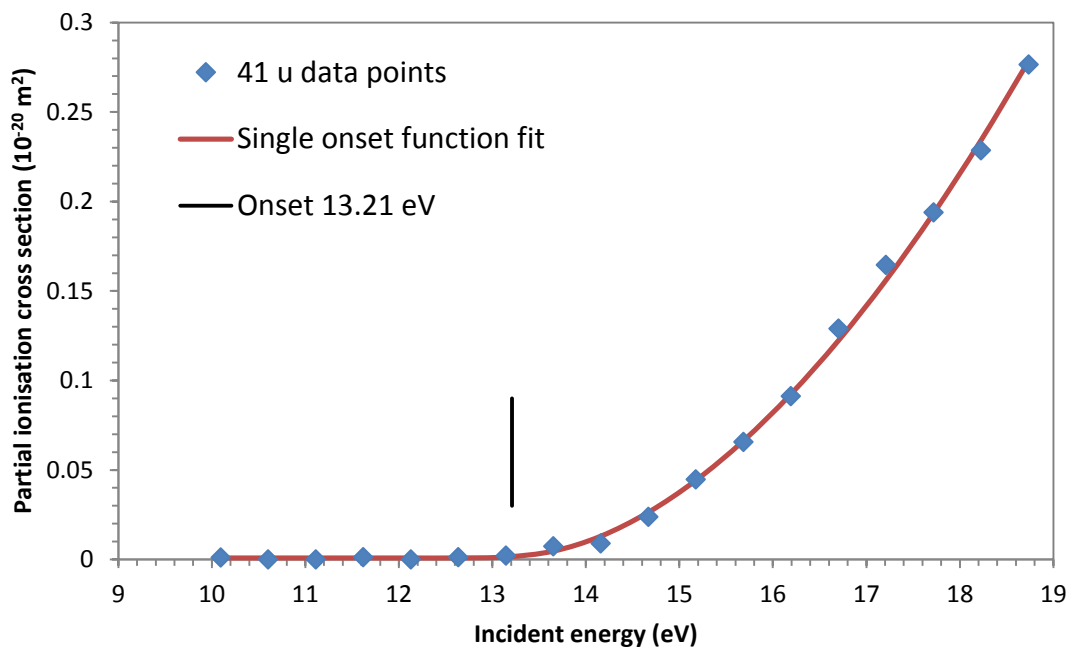**Figure 6.22.**Partial ionization cross section of 42 u fragment.

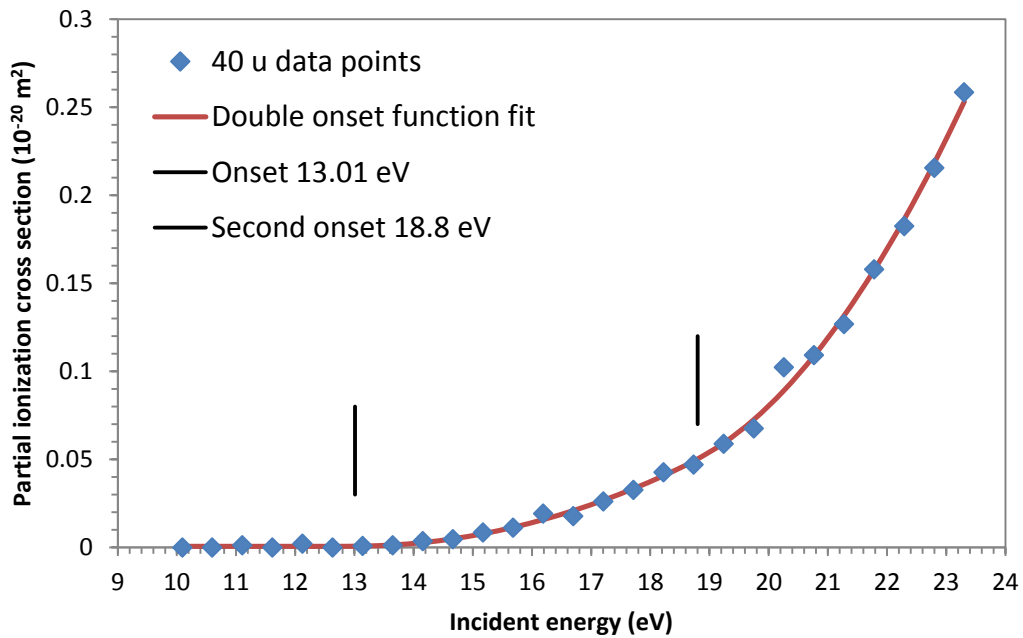**Figure 6.23.** Partial ionization cross section of the 41 u fragment.

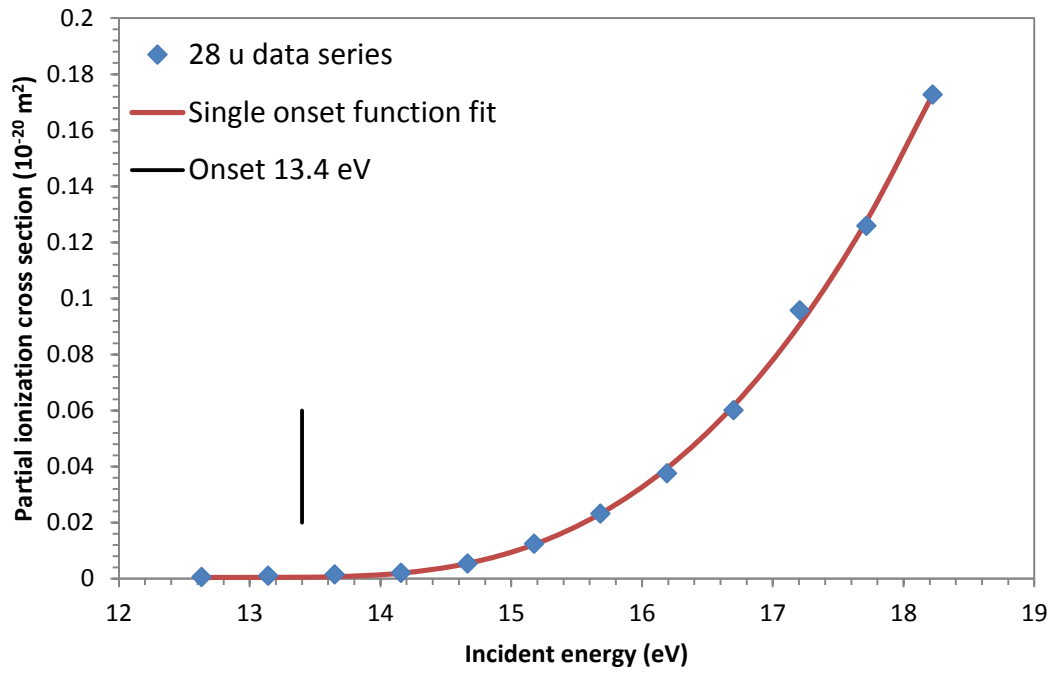**Figure 6.24.** Partial ionization cross section of the 40 u fragment.

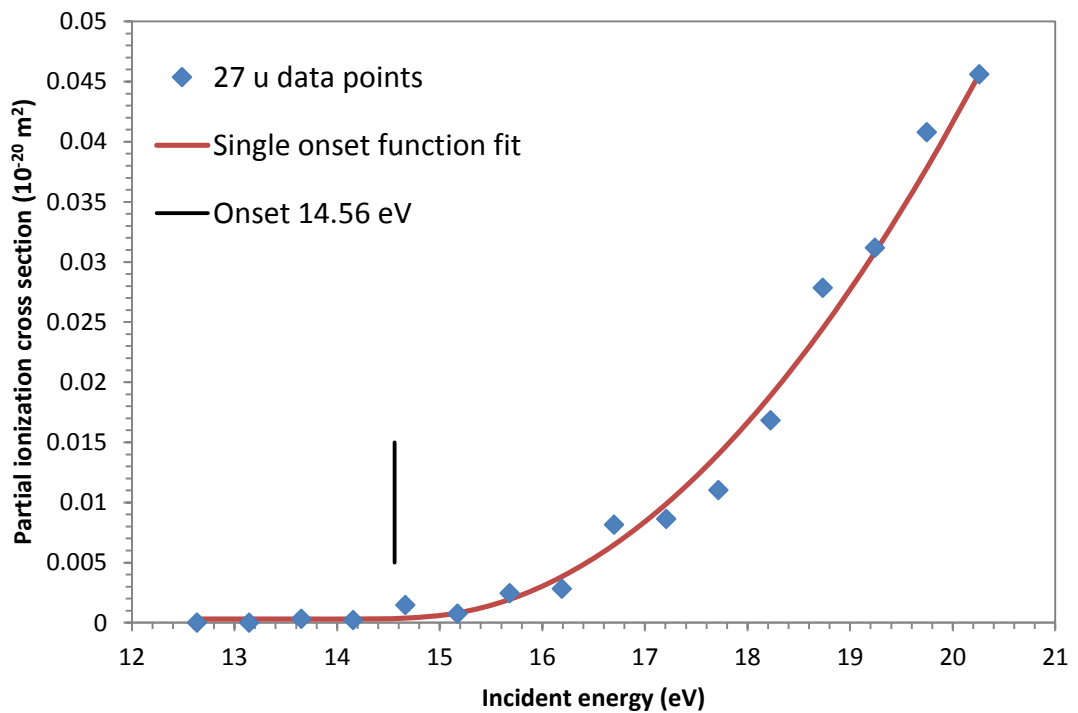**Figure 6.25.** Partial ionization cross section of the 28 u fragment.

Figure 6.26. Partial ionization cross section of the 27 u fragment.
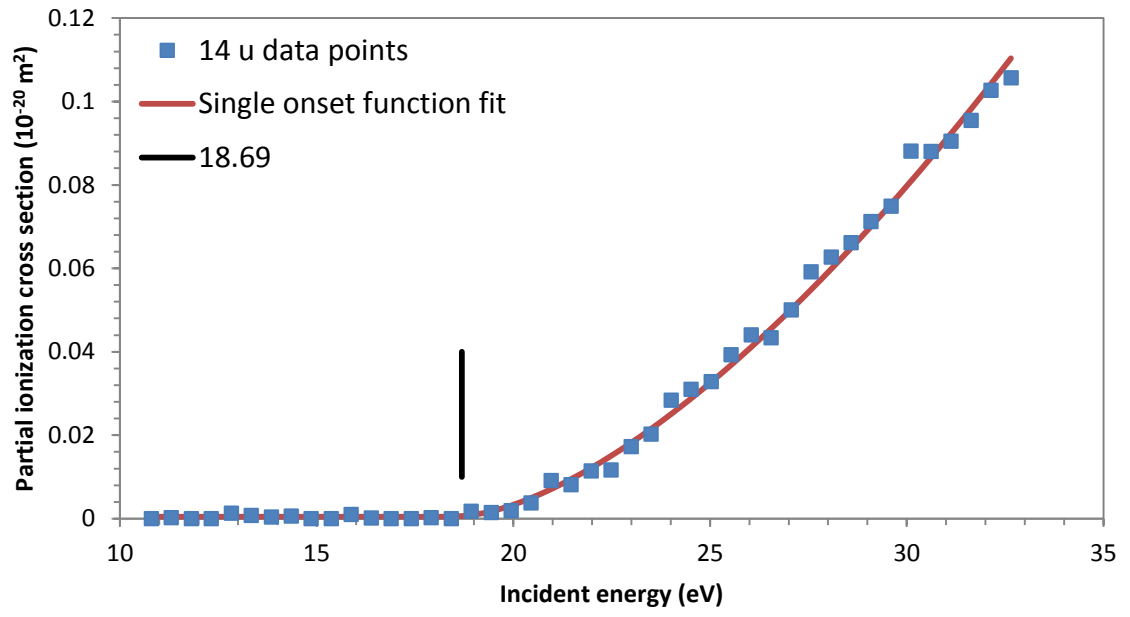
Figure 6.27. Partial ionization cross section of the 14 u fragment.

6.6 Fragmention processes

This chapter will present new results for the formation of positively charged fragments following low energy electron impact to uracil. It is important to note that the uracil molecule can occur in different tautomeric forms. Different uracil tautomers based on calculations by Tsuchiya et al [65] are shown in figure 6.28. Tautomerization preceding the dissociation of the parent ion may be significant in the sequential fragmentation of the radical cations. Atomic rearrangements prior to fragmentation have also been observed in other nucleobases [50]. Comparison of the ion yield curves of the various groups of fragments clearly shows that several of the curves have very similar shapes possibly pointing towards the relevance of tautomerization. In this section we consider possible fragmentation processes based on the measured data. Figure 6.29 presents selected fragmentation sequences of uracil identified by Rice et al [21].
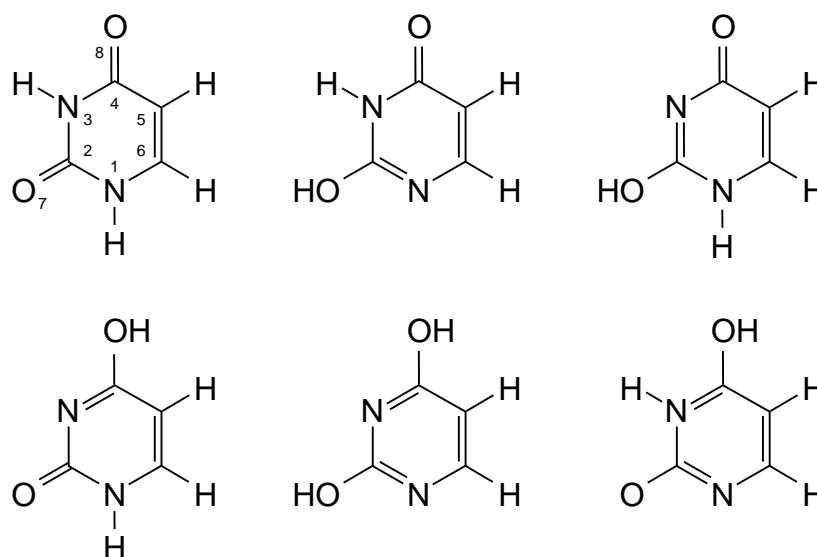

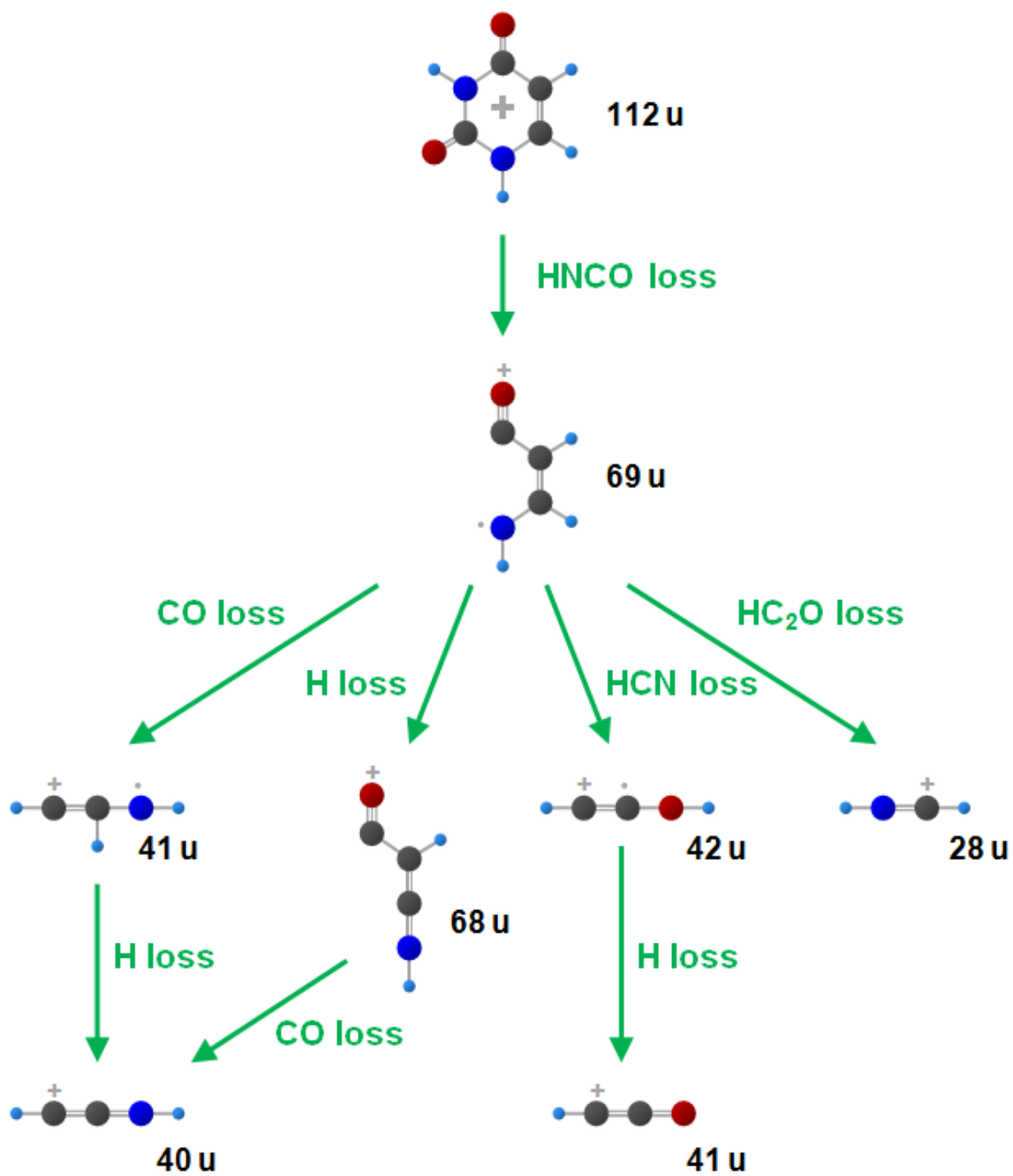**Figure 6.28**. Tautomeric structures of uracil. Adapted from [65]

Figure 6.29. Selected fragmentation patterns for uracil (adapted from Rice et al [21]).

6.6.1. The 112-113 u group

There is a presence of a very weak peak at 113 u possibly u due to uracil containing a ^{13}C natural isotope. The 113 u appearance energy was not measured because the 113 u peak is a very weak peak directly adjacent to the very strong 112 u peak, and is poorly resolved. Subsequent productions of HNCO, HCN, CO, and H (as well as combinations of these neutrals) account for the lower m/q fragment ions. We note that there is no initial loss of CO from the parent ion, since there is no 84 u fragment ion present in the mass spectrum of uracil.

6.6.2. The 65-71 u group

Neutral HNCO loss has been widely recognized as the initial step in the dominant fragmentation pathway of the 112 u fragment. Jochims et al note the principal fragmentation pathway involves loss of neutral HCNO by the Retro-Diels-Alder reaction resulting from the N1-C2 and N3-C4 bond breaks. This involves the expulsion of HNCO leading to 69 u. The 69 u ion can also lose a hydrogen atom to give a 68 u fragment that produces a strong peak in our mass spectrum.
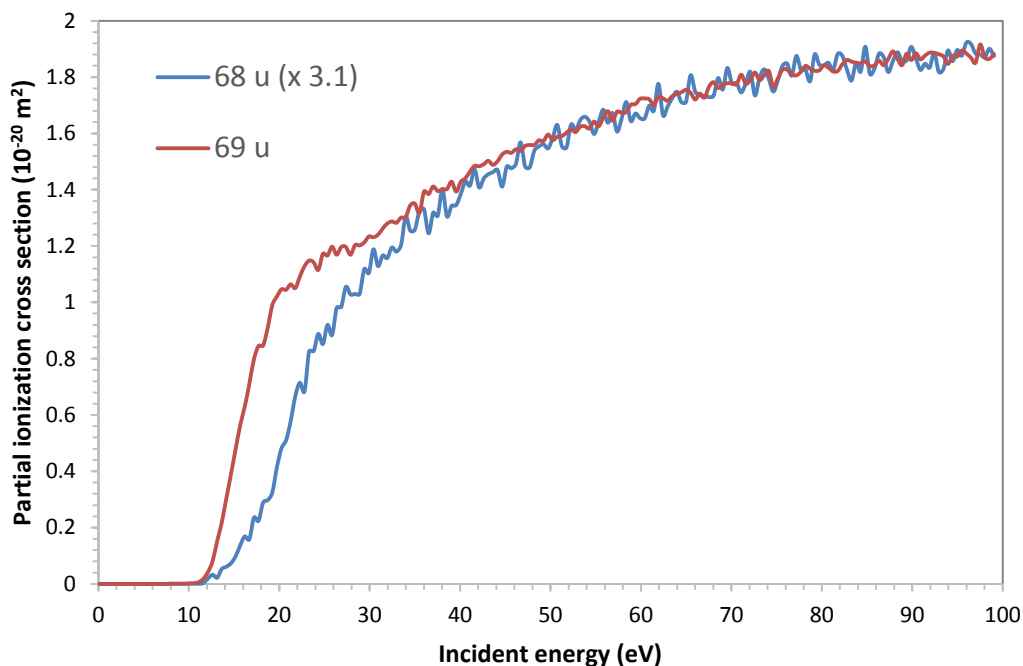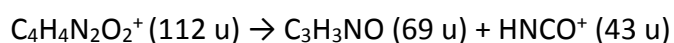
$$C_4H_4N_2O_2^+ \ (112 \ u) \rightarrow C_3H_3NO^+ \ (69 \ u) + HNCO \ (43 \ u)$$
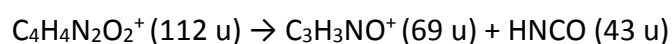
Figure 6.30. Similar partial ionization cross sections of the 68 u and 69 u fragments.

The 69 u and 68 u ion yield curves have a constant yield ratio above 50 eV as shown in figure 6.30. From threshold to 50 eV the ion yield curve of 68 u rises differently from 69 u.

$$C_4H_4N_2O_2^+ (112 \text{ u}) \rightarrow C_3H_3NO (69 \text{ u}) + HNCO^+ (43 \text{ u})$$

The formation of the 70 u ion could result from HNCO loss from the 113 u parent ion. The fragmentation of the 70 u ion can also give rise to the HNCO (43 u) molecule by loss of a HCN molecule.

We have observed the 65 u peak in our mass spectrum and this has not been identified in mass spectra by other groups. This fragment is possibly due to a bond breakage directly from the parent ion itself resulting in the 65 u ionised fragment and the neutral CH_3O_2 (47 u):

$$C_4H_4N_2O_2^+ \text{ (112 u)} \rightarrow C_3N_2H^+ \text{ (65 u)} + CH_3O_2 \text{ (47 u)}$$
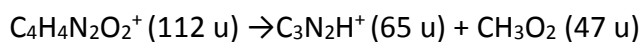
Several bond re-arrangments would be needed to create this ion leaving it very unlikely. It is difficult to attribute this peak to contamination as it is not present in the mass spectrum of thymine, and is only a very weak peak in the mass spectra of cytosine and adenine, which were studied earlier with the apparatus.

6.6.3. The 38 – 44 u group

All smaller fragments (44 u and lower) have appearance energies above 13 eV, indicating that all these fragments are the result of successive fragmentations via 112 u and 65–70 u. Denifl et al [5] assigned OCN^+ to the 42 u fragment. Formation of the OCN^+ fragment ion directly from the parent ion would involve rupture of three bonds, and it would involve a very complex reorganization process if the precursor ion was the 69 u ion. We have assigned the 42 u fragment to the $C_2H_2O^+$ ion *via* a HCN loss from the 69 u fragment.

$$C_3H_3NO^+ \text{ (69 u)} \rightarrow C_2H_2O^+ \text{ (42 u)} + HCN \text{ (27 u)}$$
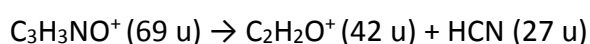
The process for the production of the 42 u ion is shown in figure 6.31 (b). The 42 u ion can be formed by a bond breakage between C6-C5 with a 6,8 H-shift from the 69 u fragment. Jochims et al [50] notes that the other possible isomer of $C_2H_3N^+$ could be $H_2C=C=O^+$. The assignment of the 42 u ion to $HC=COH^+$ is consistent with the fragmentation patterns from electron impact mass spectra of at least four 2,4-dioxypyrimidenes [31], whose structures are related to uracil.

The 69 u fragment ion can also lead to a 41 u ion by CO loss. This process is shown in figure 6.31 (c). ie, the 41 u ion is formed by a bond breakage between C4-C5.
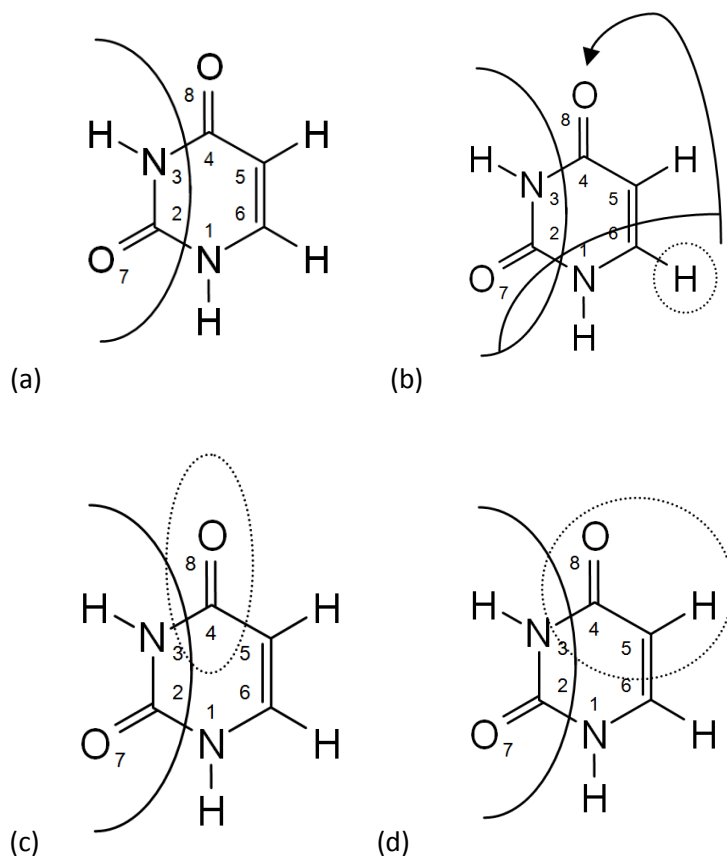
$$C_3H_3NO^+ (69\ u) \rightarrow C_2H_3N^+ (41\ u) + CO\ (28\ u)$$
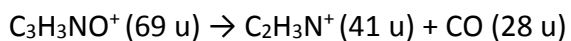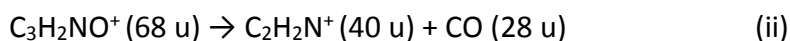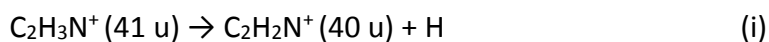

Figure 6.31. Possible fragmentation processes of the core ionized uracil molecule.
(a) 69 u (b) 42 u (c) 41 u (d) 28 u

It has been proposed by Jochims et al [50] that the 40 u fragment ion can be formed via two pathways: (i) loss of a CO molecule from the 69 u ion, followed by loss of a hydrogen atom or (ii) loss of H from 69 u followed by loss of CO molecule.

$$C_2H_3N^+ (41\ u) \rightarrow C_2H_2N^+ (40\ u) + H \qquad\qquad\qquad (i)$$

$$C_3H_2NO^+ (68\ u) \rightarrow C_2H_2N^+ (40\ u) + CO\ (28\ u) \qquad\qquad (ii)$$

Our ion yield measurements would suggest the second pathway as the measured appearance energy (13.01 eV) for the 40 u ion is higher than that of the 68 u ion (12.36 eV) and lower than that of the 42 u (13.07 eV) ion. Rice et al [21] confirmed that the only ion fragment observed with m/q of 40 u is $C_2H_2N^+$. However we have not ruled out the first pathway as the appearance energy of the 40 u fragment (13.01 ± 0.66 eV) is within range of the appearance energy of the 41 u fragment (13.21 ± 0.25 eV). The second onset of this ion is a result from multiple fragmentations to the formation of this fragment. It is difficult to conclude the exact fragmentation process involved when dealing with the higher onsets.

Despite differences in appearance energies and in the rise at low electron energies, above 40 eV the ion yield curves of 41 u, 43 u and 44 u have similiar ion yield curves as shown in figure 6.32. This may be due to tautomerization or H atom rearrangement during the fragmentation.
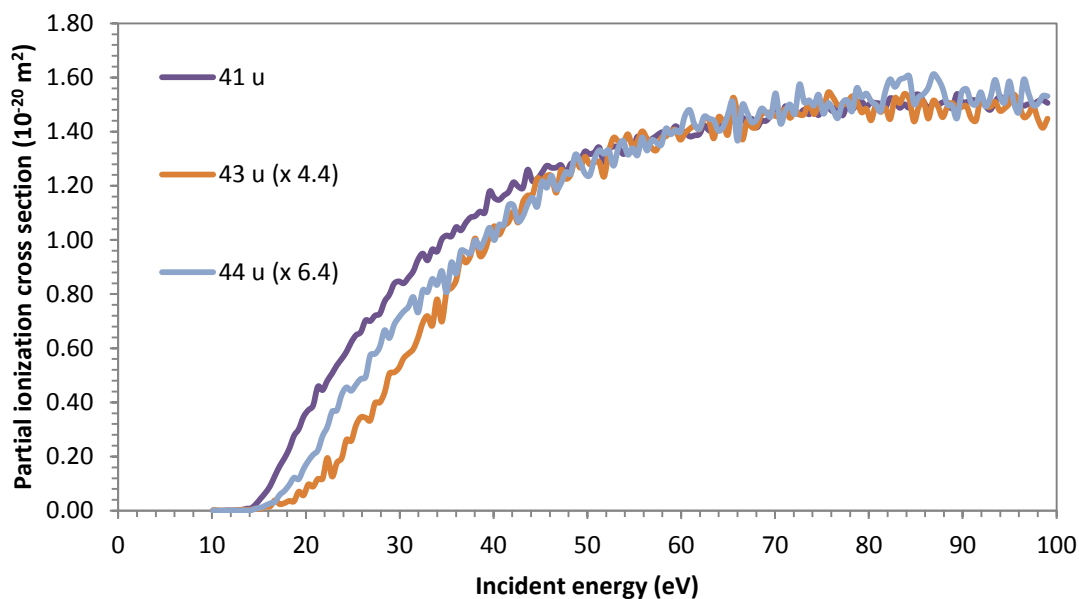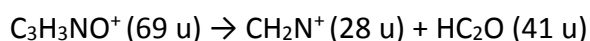
Figure 6.32. Partial ionization cross sections of the 41, 43 and 44 u fragments with multiplication factors.

6.6.4. The 26-29 u group

The fragmentation pathway by the rupture of the central carbon–carbon bond of the 69 u ion could lead to the formation of $HCNH^+$ (28 u) by loss of the ketene radical (HC=C=O).

$$C_3H_3NO^+ \, (69 \text{ u}) \rightarrow CH_2N^+ \, (28 \text{ u}) + HC_2O \, (41 \text{ u})$$

This process is shown in figure 6.31 (d). The pathway to the formation of the 28 u isomer CH_2N^+ could also result from the 68 u precursor ion. Jochims et al [50] found that the intensity of the 69 u ion decreases rapidly above 15.39 eV which is close to their onset of the 28 u ion. They suggest from this evidence that both pathways to the formation of the $HCNH^+$ fragment are operative, weakly from the parent ion pre-cursor, and strongly from the 69 u precursor. The fragmentation of the 43 u

105

fragment may also lead to the production of the 27 u fragment as shown in figure 6.33 and in the following reaction :

$$C_3H_3NO^+ (69\ u) \rightarrow HCN^+ (27\ u) + C_2H_2O\ (42\ u)$$

43 u	27 u	26 u
HNCO$^+$	CHN$^+$	CN$^+$
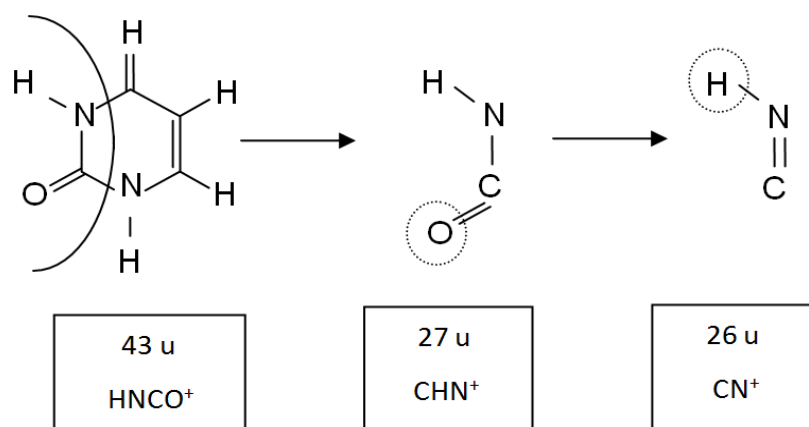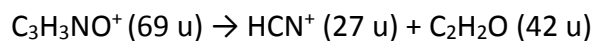
Figure 6.33. Possible fragmentation process of the 43 u ion.

The progressively increasing appearance energies for the 28, 27 and 26 u fragments also suggest the progressive loss of a hydrogen atom.

$$C_3H_3NO^+ (69\ u) \rightarrow CH_2N^+ (28\ u) + HC_2O\ (41\ u)$$

$$CH_2N^+ (28\ u) \rightarrow CHN^+ (27\ u) + H$$

$$CHN^+ (27\ u) \rightarrow CN^+ (26\ u) + H$$
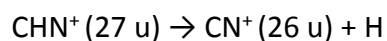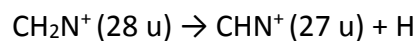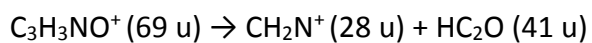
The ion yield curves for the 27 and 26 u fragments have similar ion yield shapes shown in figure 3.34.

Figure 6.34. Similar partial ionization cross sections of the 26 u and 27 u fragments.

Chapter 7: Test measurements with the supersonic source

This chapter will look at the experimental work carried out using the supersonic source. The supersonic source features a 50 micron straight nozzle with argon used as the buffer gas (see section 3.3.3). The supersonic source improves beam collimation and will enable formation of small nucleobase-water clusters when water vapour is introduced into the source. The supersonic source design will also allow for energy calibration using argon peaks.

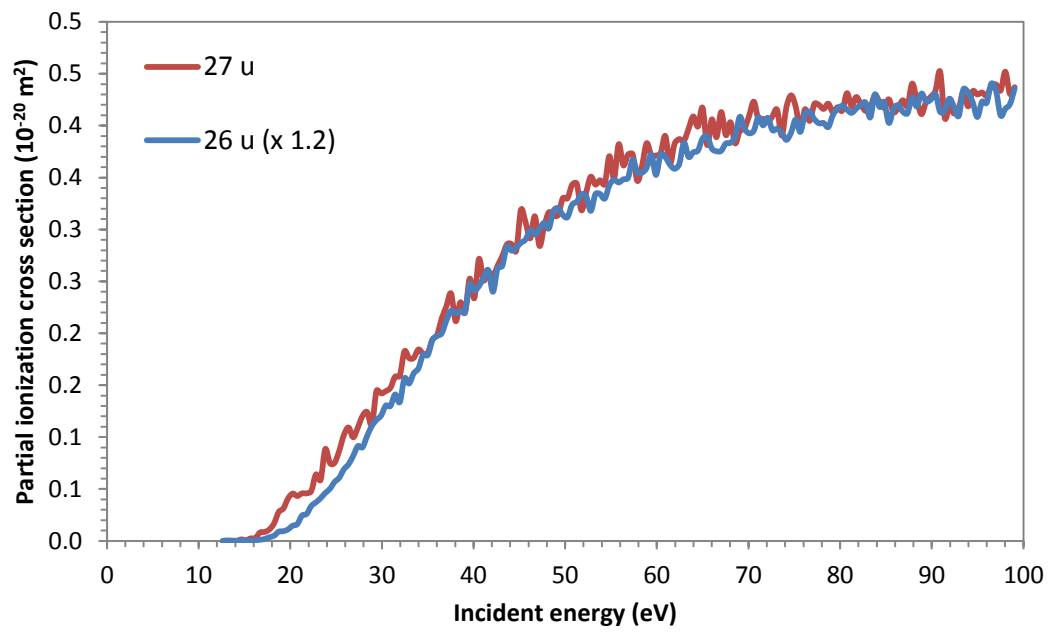One of the main objectives of this research was to implement and test the supersonic source design. This chapter is to demonstrate the capabilities of the supersonic source design. The current settings will have to be investigated further by future research students.

A uracil mass spectra and ion yield curves presented in this chapter have been obtained using the supersonic source experimental set up described in chapter 3. The incident electron energy was varied from 0 to 100 eV in 0.5 eV steps using the programmable power supply described in section 5.4. All ionization yield curves have been generated from a single data set. 28 cycles were measured in total to make up the data set using the data acquisition methods described in chapter 4. This chapter will compare the uracil mass spectrum and ion yield curves from chapter 6 using the effusive source with the uracil mass spectrum and ion yield curves using the supersonic source.

7.1 Uracil mass spectrum comparison

The uracil mass spectrum shown in figure 7.1 was measured at an electron impact energy at 70 eV using the supersonic source and is compared with the uracil mass spectrum from section 6.1. A vertical scaling factor was used to superimpose the 69 u and 112 u peaks.

The two dominant peaks at 20 u and 40 u in the supersonic source mass spectrum are due to Ar^+ and Ar_2^+ as a result of the buffer gas. There are several additional peaks in the supersonic source spectrum that are not seen in the effusive source spectrum. The additional peaks suggest that there is contamination in the system. The foreline was not thoroughly cleaned before the addition of the supersonic source. Remnants of cleaning solution may have been added during the implementation of the new buffer gas system that could count for some of the peaks. Acetone (58 u) is absent however a methanol (32 u) peak is present which was used for rinsing out the tube. 28 u and 32 u indicate the presence of air, which may be outgassing from the walls of the tube. The spurious peaks at 36 u and 38 u cannot be identified.
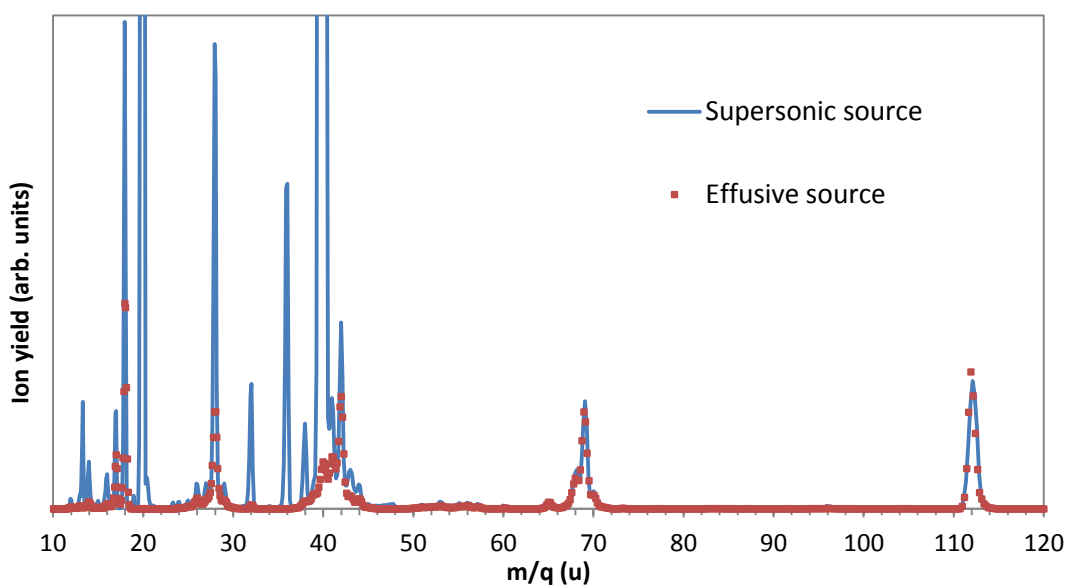

Figure 7.1. Uracil mass spectra comparison.

7.2 Ion yield curve comparisons

In this section the ion yield curves measured with the supersonic source are compared to the ion yield curves measured with the effusive source. Figure 7.2 compares the ion yield curves of the parent ion. The supersonic source ion yield curve exhibits a lower yield in comparison to the effusive source ion yield curve, a multiplication factor was used for the supersonic source ion yield curve.

The supersonic source ion yield curve reaches a maximum at around 22 eV where the effusive ion yield curve has a maximum at around 100 eV. After 22 eV the supersonic source ion yield curve steadily decreases. This could be due to variation in the overlap of the electron beam with the molecular beam. It is assumed that the electron beam width variation has a greater effect on the supersonic molecular beam as there is a smaller overlap. This is also shown in figure 7.3 for each of the ion yield curves in the 67 u – 71 u group. Figure 7.4 compares the 69 u supersonic source ion yield curve with the 69 u effusive source ion yield curve. The supersonic source ion yield curve is shown to peak at 22 eV which is the same to the peak of the parent ion however the rate of drop off differs slightly.
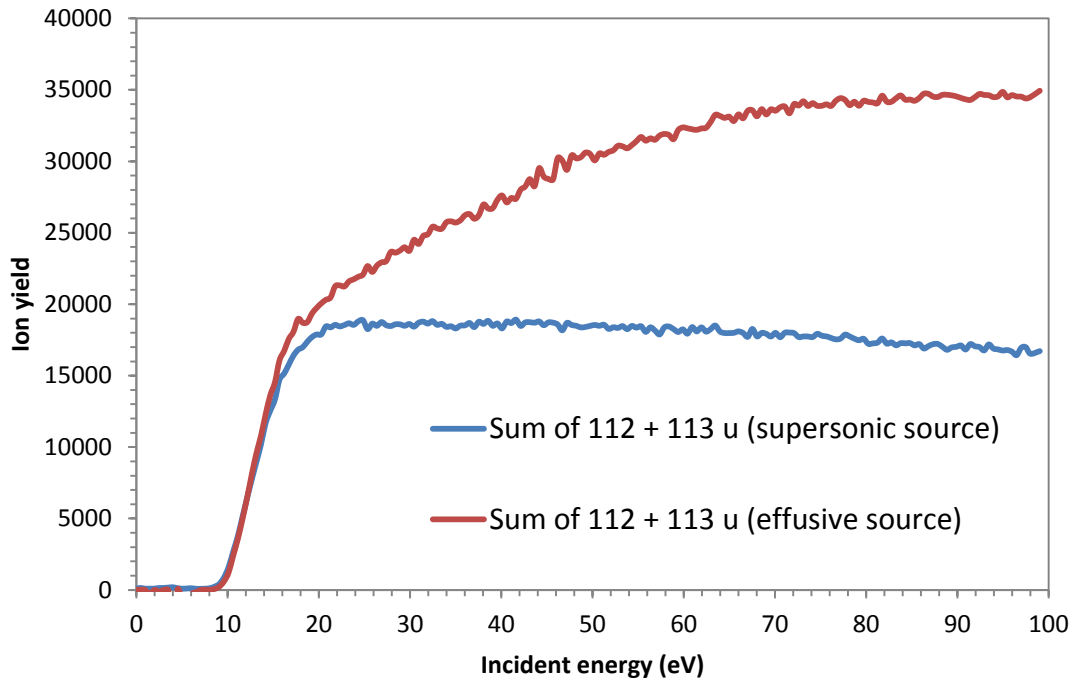
Figure 7.2. 112 u ion yield comparison.
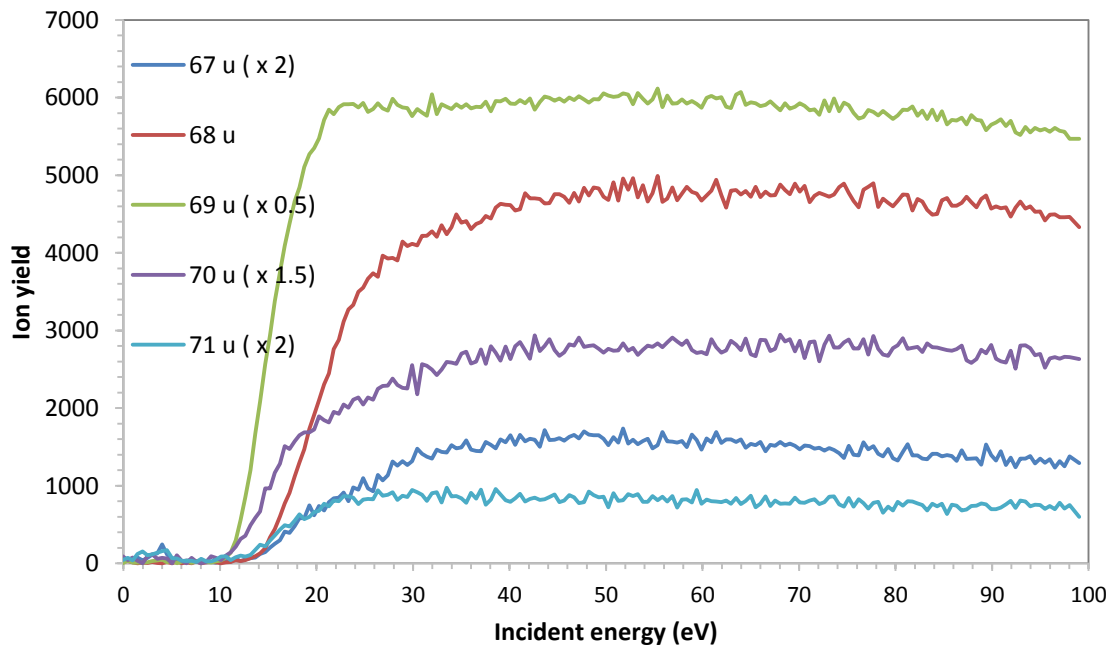
Figure 7.3. 67 u – 71 u group ion yield curves.
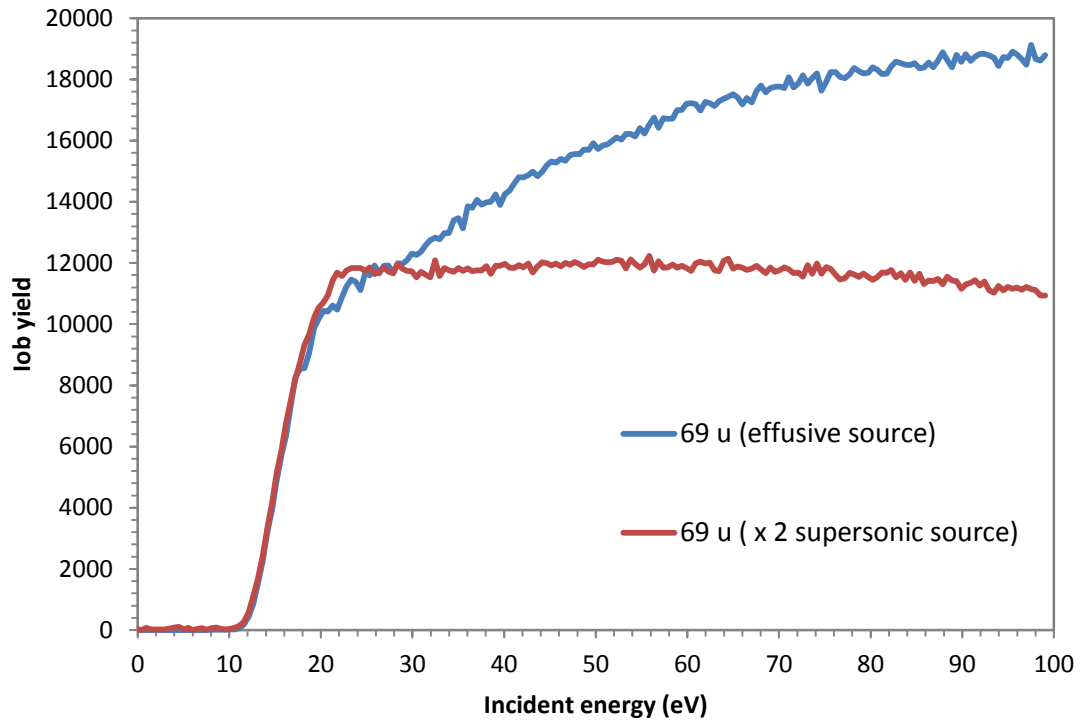
Figure 7.4. 69 u ion yield curve comparison.

The argon peaks in our mass spectrum have been compared to the ionization cross sections from Rejoub et al [66]. This paper contains ionization cross section data for electron collisions with argon. The ion yield curves for the Ar^+ and Ar^{2+} were determined using the peak fitting procedure described in section 4.4.4. The graph compares our ionization yield curves for 20 u (Ar^{2+}) and 40 u (Ar^+) to the data from Rejoub et al. There is good agreement for the Ar^{2+} curves however there is poor agreement for Ar^+ curve, but the disagreement is far less than for the 112 u and 69 u ion yield curves.
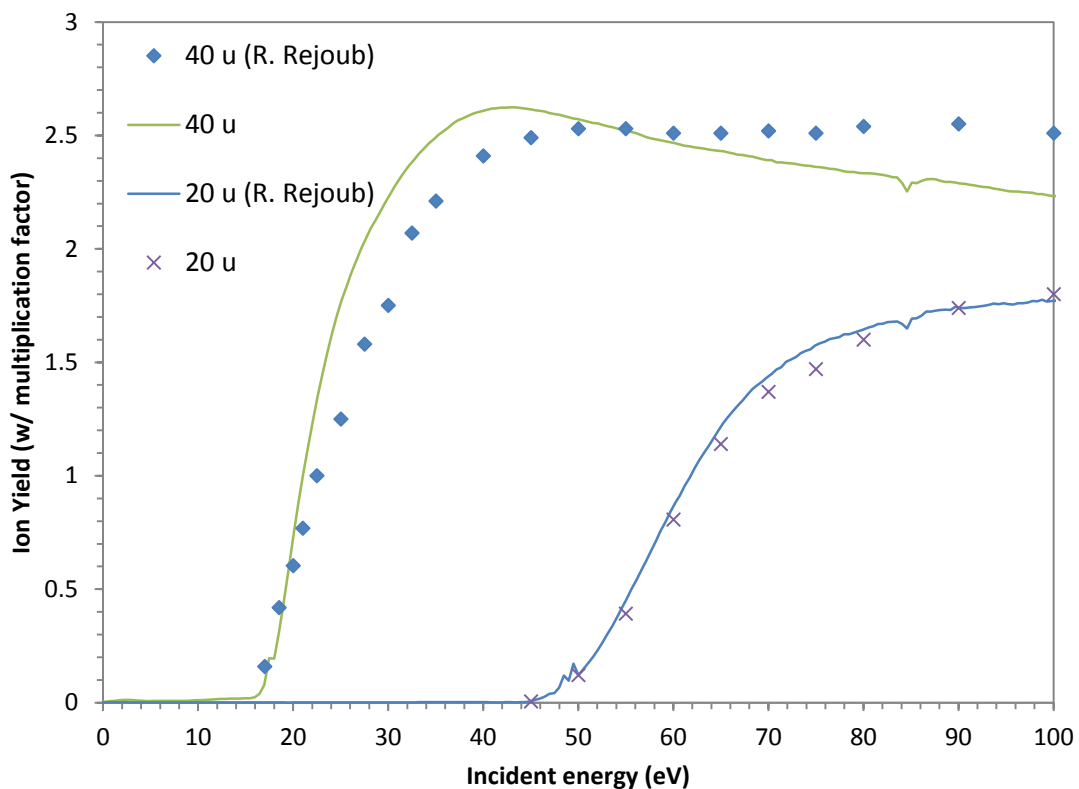
Figure 7.5. Ionization yield curves of 40 u and 20 u compared to R Rejoub [64].

7.3 Problems identified and future plans

The results of the test measurements with the new supersonic source have been very disappointing. A number of problems have been identified, that will be rectified in the future.

During the test, the front part of the source with the uracil container was heated to 200 °C, but the other parts of the container were not heated. Future plans include baking the entire system, heating the foreline and the addition of an accurate temperature controller of the source to better control pressure regulation and reduce contamination.

Also, a better molecular beam may be produced by using a higher temperature for the uracil container. During the measurements the pressure in the foreline was set to 0.1 bar but the pressure fluctuated from 0.012 to 0.168 bar, which would indicate that the argon was not introduced into the source at a constant rate.

Possibly a better pressure handling system can be implemented by using a single regulator to reduce the pressure directly from the pressure in the gas bottle down to the pressure in the source. To keep the pressure in the source chamber to below 1×10^{-4} bar, the pressure in the supersonic source had to be kept to less than 0.2 bar. By using a bigger forepump we may be able to go down to 0.5 bar. We are also planning to use neon as a buffer gas to avoid buffer gas peaks appearing near uracil fragment peaks in the mass spectra.

The overlap of the electron beam with the molecular beam is assumed to be constant throughout the entire measurement based on our electron gun settings. However based on the difference in shape of the ion yield this would suggest that the overlap is not constant. It is assumed that the electron beam width variation has a greater effect on the supersonic molecular beam as there is a smaller overlap.

The 112 u and 69 u ion yield curves suggest that there is substantial variation of the electron beam with the molecular beam, possibly because the supersonic beam is much narrower than the beam produced by the effusive source for the measurements in chapter 6. However, the disagreement is far less major for the argon ion peaks.

A possible solution is the use of a magnetic field. Magnetic field coils have already been fitted by Jason Howard [67]. However, tests conducted with the magnetic field have shown that the magnetic field direction needs to be carefully aligned with the

direction of the electron beam in order to avoid beam overlap effects due to spiralling of the electrons in the magnetic field.

We cannot compare total ionization cross sections with the old source as we could not analyse each group of peaks, and as a result we could not obtain partial ionization cross sections. However we could compare ion yield curves of the parent ion and the 69 u ion as these peaks were not contaminated.

Chapter 8: Conclusion

The main objective of this project was to study low energy electron impact induced ionization and fragmentation of uracil. The apparatus used consisted of a pumped vacuum system with an expansion chamber, a collision chamber and a flight tube. A beam of the uracil was generated in the expansion chamber and crossed with a pulsed beam of low energy electrons. The electron gun has a pulse time capable of providing the necessary time of flight resolution and incorporates a deflection system for the focusing of the low energy electron beam. The electron gun was calibrated to produce a stable beam of electrons with a constant beam current down to 17 eV, and with approximately 60% of the current to 9 eV, allowing us to determine the lower onsets such as the uracil parent ion (112 u) at 9.11 eV. A study of the water peaks in our mass spectrum was conducted to calibrate the incident energy scale for our ion yield curves.

The process was measured using a reflectron time of flight mass spectrometer with a microchannel plate detector to detect and resolve positive ionised fragments in the flight tube. A multichannel scaler card was used for data acquisition. Code written in LabVIEW was used to fit peaks in our spectrum with normalised Gaussian functions. This allowed us to obtain accurate peak areas for all the adjacent peaks over a range of 0 -100 eV from a single data set and produce ion yield curves for all the identified fragments in our spectrum. This program will be used to obtain accurate peak areas for future experiments with flurouracil and other molecules. The relative intensity of the peaks in our mass spectrum at 70 eV was compared to other groups. The appearance energies were determined from the ion yield curves and are in good agreement with Denifl et al [5], M.A. Rahman and E. Krishnakumar [27] and Jochims et al [50]. The appearance energies give us an insight into the fragmentation processes of uracil induced by low energy electron impact. The total ionization cross section of our mass spectrum was compared to other groups. The information collected is relevant in the field of radiation damage on our understanding of the processes that are happening on the microscopic scale, when ionising radiation passes through living cells. These results provide new information

about the fragmentation pathways initiated by electron impact and the cross sections for production of these ions.

The experiment implemented and developed a supersonic source design using a 50 micron straight nozzle with argon gas acting as the buffer gas. The results of the test measurements with the new supersonic source have been very disappointing. A number of problems have been identified, that will be rectified in the future. The main factor is believed to be problems with the the overlap of the electron beam with the molecular beam. The overlap is assumed to be constant throughout the entire measurement based on our electron gun settings. However based on the difference in shape of the ion yield this would suggest that the overlap is not constant. It is assumed that the electron beam width variation has a greater effect on the supersonic molecular beam as there is a smaller overlap.

Future work will look into the formation of small nucleobase-water clusters when water vapour is introduced into the source. Other plans for the future are the detection of neutral metastable fragments using the metastable detector in the collision chamber and a redesign of the electron gun using molybdenum lens elements (the gun used in this work only has molybdenum apertures).

Bibliography

1. M. Bardies and P. Pihet, *Cur. Pharm. D*. **14** (2000)

2. J. E. Turner, "Atoms, *Radiation, and Radiation Protection*", Wiley-VCH (2010)

3. B. Boudaiffa, P. Cloutier, D. Hunting, M.A. Huels and L. Sanche, *Science* **287** (2000)

4. L. Sanche*, Eur. Phys. J.* **35** (2005)

5. S. Denifl, G. Hanel, P. Scheier and T.D. Mark, *Int. J. of Mass Spect.* **238** (2004)

6. A.D. Bass and L. Sanche "*Charged particle and photon interactions with matter: Chemical, physicochemical and biological consequences with applications*" Marcel Dekker (2004)

7. B. Alberts *"Essential Cell Biology"* Garland Science (2010)

8. J.C. Kotz "*Chemistry and Chemical Reactivity"* Thomson (2009)

9. https://upload.wikimedia.org/wikipedia/commons/4/4c/Uracil-3D-balls.png.

10. Wei Han and K. N. Yu, *Advances Gen. Research* **4** (2010)

11. P. O'Neill, *Rad. Chem.* **87** (2001)

12. M.S. Yadav "*A Textbook of Spectroscopy*" Anmol publications (2003)

13. X. Pan, P. Cloutier, D. Hunting, and L. Sanche, *Phys. Rev. Lett*. **90** (2003)

14. J.H. Gross "*Mass spectrometry"* Springer (2011)

15. S. Ptasińska, B. Mróz, M. Probst, V. Grill, E. Illenberger, P. Scheier, and T. D. Märk, *J. Chem. Phys*. **123** (2005)

16. L. Sanche, *Eur. Phys. J. D*, **35** (2005)

17. S. Denifl S, P. Scheier, M. Probst, B. Farizon, M. Farizon, E. Illenberger and T.D. Mark, *Phys. Rev. Lett.* **90** (2003)

18. S. Gohlke and E. Illenberger, *Europhys. News* **33** (2002)

19. P. Burrow, G. A. Gallup, A.M. Scheer, G. Denifl, S. Ptasinska, T. Märk, and P. Scheier, *J. Chem. Phys*. **124** (2006)

20. N.J. Mason, B. Nair, S. Jheeta and E. Szymańska, *Faraday discuss.* **168** (2014)

21. J.M. Rice, G.O. Dudek and M. Barber, *J. Am. Chem. Soc.* **87** (1965)

22. J. Ulrich, R. Teoule, R. Massot and A. Cornu, *Org. Mass Spectrom*. **2** (1969)

23. T. Schlathölter, R. Hoekstra and R. Morgenstern, *Mass Spectrom*. **233** (2003)

24. M. Imhoff, J. Deng and M.A. Huels, *Int. J. Mass Spect*. **262** (2007)

25. S. Feil, K. Gluch, S. Matt-Leubner , P. Scheier , J. Limtrakul, M. Probst, H. Deutsch, K. Becker, A. Stamatovic and T. D. Märk, *J. Phys. B: At. Mol. Opt. Phys*. **37** (2004)

26. I. I. Shafranyosh, M. I. Sukhoviya, M. I. Shafranyosh, and L. L. Shimon, *Tech. Phys.* **53** (2008)

27. M.A. Rahman and E. Krishnakumar, *Int. J. Mass Spect*. **392** (2015)

28. A. Dora, L. Bryjko, T. van Mourik and J. Tennyson, *J. Phys.* **45** (2012)

29. P. Mozejko and L. Sanche, *Rad. Phys. Chem.* **73** (2005)

30. M. Vinodkumar, C. Limbachiya, M. Barot, M. Swadia and A. Barot, *Int. J. Mass. Spect.* **339** (2013)

31. H.W. Jochims, H. Baumga and S. Leach, *Chem. Phys.* **314** (2005)

32. J. Tabet, S. Eden, S. feil, H. Abdoul-Carmine, B. Farizon, M. Farizon, S. Ouaskit and T.D. Mark, *Int. J. Mass Spect*. **292** (2010)

33. Edmond de Hoffmann and Vincent Stroobant *"Mass Spectrometry principles and applications"* Wiley, third edition*,* (2007)

34. J. Mattauch*, Phys. Rev*. **50** (1936)

35. http://www.chemicool.com/definition/quadrupole_mass_spectrometry.html

36. http://www.nature.com/nrd/journal/v2/n2/fig_tab/nrd1011_F4.html

37. W.C. Wiley and I.H. McLaren, *Rev. Sci. Instrum*. **26** (1955)

38. W. Stephens. *Phys. Rev.* **69** (1946)

39. W.C. Wiley and J.B. McLaren, *Rev. Sci. Instrum*. **16** (1955)

40. B.A. Mamyrin, V. I. Karataev, D. V. Shmikk, and V. A. Zagulin, *Zh. Eksp. Teor. Fiz.* **64** (1972)

41. B.A. Mamyrin, *Int. J. Mass Spect*. **206** (2001)

42. *"Construction of a Supersonic Beam Experiment for Cluster Studies"*, Joseph E. Lynch*, MSc Thesis,* National University of Ireland, Maynooth *(2001)*

43*. "Development of an Apparatus for the Study of Electron Impact Fragmentation of Molecular Clusters",* Gerard Thomas Barrett*,* MSc thesis, National University of Ireland, Maynooth (2008)

44. *http://www.thinksrs.com/products/DG535.htm.*

45. *Model 7886 2 GHz Multiscaler User Manual, FAST ComTEC, 2.1, September 1998*

46. *"Study of low energy electron-impact induced fragmentation of adenine",* Sinead Finnegan, MSc thesis, National University of Ireland, Maynooth (2014)

47. Y. Itikawa*, J. Phys. Chem.* **34** (2005)

48. H. C. Straub, B. G. Lindsay, K. A. Smith, and R. F. Stebbings, *J. Chem. Phys.* **108** (1998)

49. B. G. Lindsay and M. A. Mangan, "*Photon and Electron Interactions with Atoms, Molecules and Ions"*, Landolt-Bornstein **Vol. I/17**, Subvolume C, edited by Y. Itikawa, Springer, New York (2003)

50. M. Jochims, H. Schwell, Baumgartel and S. Leach*, Chem. Phys.* **263** (2005)

51. C. Lifshitz, E.D. Bergmann and B. Pullmann, *Tetrahedron Lett. 46 (1967)*

52. B.I. Verkin, L.F. Sukodub, I.K. Yanson, Dokl. *Akad. Nauk. SSSR* **228** (1976)

53. V.I. Zaretskii, V.L. Sadovskaya, N.S. Wulfson, V.F. Sizoy and V.G. Merimson, *Org. Mass Spectrom.* **5** (1971)

54. A. Padva, P.R. LeBreton, R.J. Dinerstein and J.N.A. Ridyard, *Biochem. Biophys. Res. Commun.* **60** (1974)

55. N.S. Hush and A.S. Cheung, *Chem. Phys. Lett.* **34** (1975)

56. D. Dougherty, K. Wittel, J. Meeks and S.P. McGlynn, *J. Am. Chem. Soc.* **98** (1976)

57. G. Lauer, W. Schafer and A. Schweig, *Tetrahedron Lett.* **45** (1978)

58. M.H. Palmer, I. Simpson and R.J. Platenkamp, *J. Mol. Struct.* **66** (2006)

59. C. Yu, T.J. O'Donnell and P.R. LeBreton, *J. Phys. Chem.* **85** (1981)

60. S. Urano, X. Yang and P.R. Le Breton, *J. Mol. Struct.* **214** (1989)

61. M. Kubota and T. Kobayashi, J. El. Spectros. *Rel. Phen.* **82** (1996)

62. S.D. Wetmore, R.J. Boyd and L.A. Eriksson, *Chem. Phys. Lett.* **322** (2000)

63. N. Russo, M. Toscano and A. Grand, J. *Comput. Chem.* **21** (2000)

64. G. Fogarasi, *J. Mol. Struct.* **271** (1997).

65. Y. Tsuchiya, T. Tamura, M. Fujii and M. Ito, J. *Phys. Chem.* **92** (1988)

66. R. Rejoub, B. G. Lindsay, and R. F. Stebbings, *Phys. Rev.* **65** (2002)

67. *"Electron and Ion Collisions on Adenine and Thymine"*, Jason James Howard, MSc thesis, National University of Ireland, Maynooth (2009)